NPS-SP-19-003

NAVAL POSTGRADUATE SCHOOL

MONTEREY, CALIFORNIA

FAILURE ANALYSIS OF COMPOSITE CYLINDERS UNDER COMPRESSIVE AXIAL LOADING

by

Benedikt Mertens

July 2019

Approved for public release; distribution is unlimited

Prepared for: Naval Postgraduate School

THIS PAGE INTENTIONALLY LEFT BLANK

REPORT DOCUMENTATION PAGE			*Form Approved* OMB No. 0704-0188
Public reporting burden for this collection of information is estimated to average 1 hour per response, including the time for reviewing instructions, searching existing data sources, gathering and maintaining the data needed, and completing and reviewing this collection of information. Send comments regarding this burden estimate or any other aspect of this collection of information, including suggestions for reducing this burden to Department of Defense, Washington Headquarters Services, Directorate for Information Operations and Reports (0704-0188), 1215 Jefferson Davis Highway, Suite 1204, Arlington, VA 22202-4302. Respondents should be aware that notwithstanding any other provision of law, no person shall be subject to any penalty for failing to comply with a collection of information if it does not display a currently valid OMB control number. **PLEASE DO NOT RETURN YOUR FORM TO THE ABOVE ADDRESS.**			
1. REPORT DATE ***(DD-MM-YYYY)*** 22-07.2019	**2. REPORT TYPE** Technical Report		**3. DATES COVERED** ***(From-To)*** May-July 2019
4. TITLE AND SUBTITLE Failure Analysis of Composite Cylinders under Compressive Axial Loading			**5a. CONTRACT NUMBER**
			5b. GRANT NUMBER
			5c. PROGRAM ELEMENT NUMBER
6. AUTHOR(S) Mertens, Benedikt			**5d. PROJECT NUMBER** NPS-SP-19-003
			5e. TASK NUMBER
			5f. WORK UNIT NUMBER
7. PERFORMING ORGANIZATION NAME(S) AND ADDRESS(ES) AND ADDRESS(ES) Naval Postgraduate School 1 University Circle, Monterey, CA 93943			**8. PERFORMING ORGANIZATION REPORT NUMBER**
9. SPONSORING / MONITORING AGENCY NAME(S) AND ADDRESS(ES) Helmut-Schmidt University Holstenhofweg 85 22043 Hamburg Germany			**10. SPONSOR/MONITOR'S ACRONYM(S)**
			11. SPONSOR/MONITOR'S REPORT NUMBER(S)
12. DISTRIBUTION / AVAILABILITY STATEMENT Approved for public release; distribution is unlimited			
13. SUPPLEMENTARY NOTES			

14. ABSTRACT

The compressive behavior of filament-wound carbon-fiber/epoxy composite cylinders subjected to axial compression, especially with varying loading angles, is not widely understood, so far. The primary objective of this thesis was to determine how the compression strength of filament-wound composite cylinders vary with increasing loading offset angle. Therefore, the compression strengths of composite cylinders and aluminum cylinders subjected to compressive axial loading under different loading angles were analyzed. Two different test fixture designs were developed and constructed to vary the loading angle by 5°, 10° and 15°. Two-layered and three-layered composite cylinders were manufactured using the filament-winding technique and a winding angle of 45° was used. The experimental tests were conducted to verify the results obtained by a numerical analysis.

15. SUBJECT TERMS
Filament-Winding, Compression testing, Composite Cylinders

16. SECURITY CLASSIFICATION OF:			**17. LIMITATION OF ABSTRACT**	**18. NUMBER OF PAGES**	**19a. NAME OF RESPONSIBLE PERSON**
a. REPORT	**b. ABSTRACT**	**c. THIS PAGE**			
Unclassified	Unclassified	Unclassified	UU	162	**19b. TELEPHONE NUMBER** ***(include area code)***

Standard Form 298 (Rev. 8-98)
Prescribed by ANSI Std. Z39.18

THIS PAGE INTENTIONALLY LEFT BLANK

NAVAL POSTGRADUATE SCHOOL
Monterey, California 93943-5000

Ann E. Rondeau
President

Steven R. Lerman
Provost

The report entitled “Failure Analysis of Composite Cylinders under Compressive Axial Loading” was prepared for “Naval Postgraduate School” and funded by “Naval Postgraduate School” and “Helmut Schmidt University”.

Further distribution of all or part of this report is authorized.

This report was prepared by:

____
Benedikt Mertens
B.Sc.

Reviewed by:

____
James Newman, Chairman
Space Systems Academic Group

Released by:

____
Jeffrey D. Paduan
Dean of Research

Acknowledgements

Throughout the writing of this thesis, I experienced great support and assistance. At first, I would like to thank my advisor Prof. Kwon, who always had an open door for me. His expertise was invaluable for the success of this thesis. I immensely enjoyed the collaboration.

I would also like to thank Professor Panholzer and the Space Systems Academic Group, for the great support and assistance I experienced during my time at the Naval Postgraduate School. I also want to thank Professor Panholzer for his valued contribution on the student exchange program between the Naval Postgraduate School and the Helmut Schmidt University whereby this opportunity was made possible.

I would like to thank John Mobley for his contribution in the experimental part of this thesis by manufacturing the test fixture and by processing the specimens.

THIS PAGE INTENTIONALLY LEFT BLANK

Contents

List of Figures

List of Tables

List of Abbreviations

Approx.	Approximately
Avg.	Average
Cyl.	Cylinder
Exp.	Experimental
Max.	Maximum
Num.	Numerical
SG.	Strain gauge

1. Introduction

In this thesis, the compression strength of composite cylinders subjected to compressive axial loading under different loading angles was analyzed. Two different test fixture designs were developed and constructed to vary the loading angle by 5Â°, 10Â° and 15Â°. Two-layered and three-layered composite cylinders were manufactured using the filament-winding technique and a winding angle of 45Â° was used. Aluminum cylinders were also loaded under compressive axial loading. The experimental tests were conducted to verify the results obtained by a numerical analysis.
The use of composite materials for the design of structures in high-performance applications (e.g., aerospace, automotive, and motorsport), which require a high level of compressive performance, has increased significantly during the past few years. Composite materials have special characteristics that are different from the properties of conventional isotropic materials. Thus, composite materials have a high strength-to-weight and stiffness-to-weight ratio. Moreover, they are corrosion resistant, thermally stable and can be perfectly used for weight-sensitive structures. Aircraft manufacturers (e.g., Airbus and Boeing) make use of the advantages of these materials and started using composites in aircraft manufacturing. For instance, the airframe of the A350[1] is made out of 53% composites. Moreover, an increasing number of general aviation airplanes are also manufactured using composite materials to save weight. The Aquila A 210 (Fig. 1.1)[2] is manufactured entirely out of carbon and glass fibre reinforced plastics. Because of the use of these materials in the manufacturing process, weight could be saved.

The ability to confidently predict the compressive response of composite materials is of increasing importance. The compressive modulus and strength of a composite material are critical parameters for many structural uses. Thus, the full characterization of the properties of anisotropic and inhomogeneous composite materials for use in structural applications requires a wide range of mechanical tests. For instance, the tests have to be conducted over a range of temperatures in a variety of different environmental conditions, because the temperature can influence mechanical properties of a composite material.
Compression strength is determined by complex factors involving the fiber/matrix interface. The values of compressive strength can be much lower than values for tensile strength. Consequently, the design of a component with composites is complicated.

Another problem of the application of composite materials in structures is the lack of technology to ensure reliable designs and damage prediction. So far, uncertainties remain about the durability and aging of the materials. Thus, further studies are nec-

[1] Airbus A350, a long-range, twin-engine wide-body airplane.
[2] A two-seat light aircraft.

essary to ensure their integrity over long periods.
This work developed suitable composite compression test methods for testing composites cylinders loaded with an offset angle of the longitudinal direction. For this purpose, test fixtures are designed and fabricated for offset compression tests. Both experimental and numerical approaches are considered.

Figure 1.1.: Aquila A 210.

1.1. Compression Tests

For this research, two different types of composite cylinders are manufactured using the filament winding technique, with a winding angle of 45°. One type of cylinder is manufactured using two layers, while the other type of cylinder is manufactured using three layers. Thus, the influence of the number of layers on the compression strength of the cylinders can also be examined.
The cylinders are 101.6 mm long and tested with loading angles of 0°, 5°, 10°, and 15° to examine the compression strength for each different loading angle. Aluminum alloy cylinders, which also have a length of 101.6 mm, are also tested for the research of this thesis and also loaded with loading angles of 0°, 5°, 10° and, 15° to compare the results. Because of the loading angle and the applied force, it is suspected that one side of the cylinder will be shortened and the opposite side will be lengthened. Consequently, strain gauges have also been attached on these sides of the cylinders to measure the exact strain at these specific locations.
Two different test fixtures have been designed and used for the tests. The bottom part of the first test fixture used in chapters 6 and 7 had to be clamped with an offset in

the grip of the compression testing machine to cause loading angles of more than 0°. Because of that, the 858 MTS machine with a hydraulic grip had to be used to prevent the bottom part from slipping in the grip. In Figure 1.2, the first test fixture is clamped with the aluminum alloy cylinder and with an offset of 10° into the hydraulic grip of the compression testing machine.

The bottom part of the second test fixture was clamped without an offset in the grip. However, for each loading angle a new bottom part had to be clamped in the grip, due to the design of the bottom part. In Figure 1.3, the test fixture clamped without an offset into the grip of the testing machine is shown. A loading angle of 10° was caused by this test setup.

A numerical analysis of the experimental conducted compression tests of the aluminum alloy cylinders and the two-layered composite cylinders will also be conducted. For this analysis, the first test fixture was used. The numerical analysis was conducted to compare the computed results with the experimental determined results and to verify the computed results with the data obtained from the experimental results.

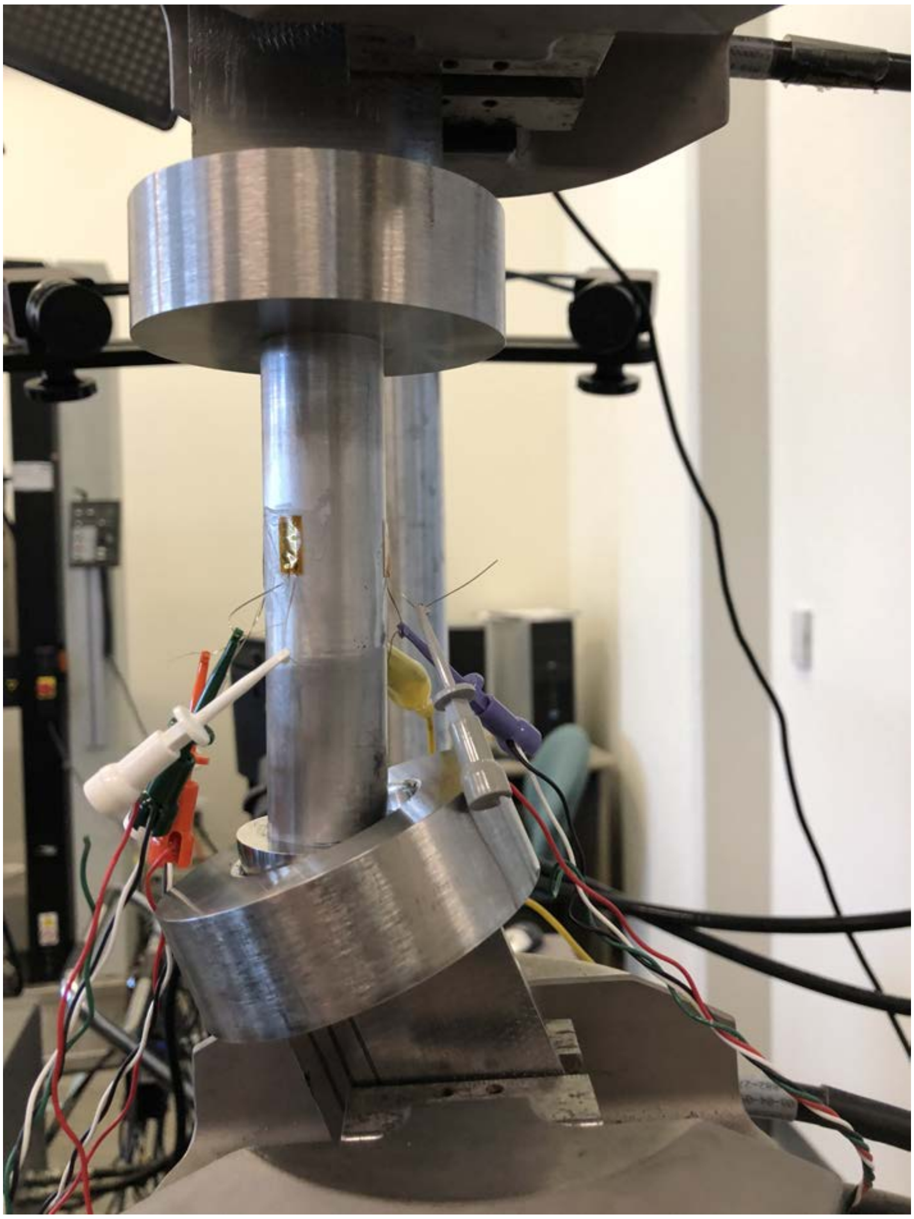

Figure 1.2.: Compression test setup at 10° offset—aluminum alloy cylinder.

Figure 1.3.: Compression test setup at 10° offset—new test fixture.

2. Composite Theory

Composite material is composed of at least two different elements which work together to produce material properties that differ from their original properties. Most composites consist of a matrix and a reinforcement of some kind which is primarily added to increase the strength and stiffness of the matrix. A fibre form is usually used as reinforcement. Almost all man-made composites can basically be divided into three different groups:

1. Ceramic matrix composites
2. Metal matrix composites
3. Polymer matrix composites

Ceramic matrix composites are used in environments which require high strength at high temperatures. Ceramic is used as the matrix and short fibres or whiskers, made from boron nitride or silicon carbide, are used to reinforce it.
The metal matrix composites are mostly used in the automotive industry. A metal (e.g., aluminum) is used as the matrix, and fibres or particles (e.g., silicon carbide) are used as reinforcement.
The polymer matrix composites, also known as FRP[1], are the most popular composites. A polymer-based resin is used as matrix, and fibres (e.g., aramid, carbon, glass) are used as reinforcement. For this thesis, polymer matrix composites will be used with UF3325 TCR epoxy resin as matrix and carbon fibre T700SC as reinforcement. Consequently, the polymer matrix composites will be discussed in the following section in more detail.

2.1. Polymer Matrix Composites

The strength of resin systems (e.g., polyesters, epoxies) is not very high when compared to other materials, like metals. However, these systems have desirable material properties and can easily be formed into complex shapes.
The reinforcement components (e.g., aramid, boron, carbon, glass) have a high tensile and compressive strength. However, when stressed, random surface defects might cause cracks and material failure even before reaching the fracture point. Hence, the high tensile and compressive strength are not readily apparent in solid forms. In order to restrict these defects to a small number of fibres, the material is produced in fibre form. Consequently, the theoretical strength of the material will not be affected. A fibre bundle alone has only a tensile strength along the fibre's length. In order to obtain the earlier mentioned material properties, the fibre has to be combined with the resin matrix, which spreads the load applied to the composite between each of the individual

[1] Fibre reinforced polymers.

fibres. Moreover, the matrix also protects the fibres from damage caused by impact and abrasion [1].

2.2. Fibres

In polymer matrix composites, a resin system and reinforcing fibres are combined. The properties of the resulting composite material will combine some of the properties of the resin with some of the properties of the fibres. The properties of the composite material are basically governed by the following aspects:

1. The properties of the fibre
2. The properties of the resin
3. The surface interaction of fibre and resin
4. The ratio of fibre resin in the composite
5. The geometry and orientation of the fibres in the composite [1]

The properties of the fibre and of the resin depend on the material and are determined by material tests. They cannot be influenced. However, these properties have to be taken into account by the composite designer and builder.
The surface interaction of fibre and resin depends on the degree of bonding between the matrix and the reinforcement.
The manufacturing process used to combine resin with fibre has a large influence on the ratio of fibre to resin in the composite. Moreover, the type of resin system and the form in which the fibres are incorporated also have an influence on the property of fibre resin.
The geometry and orientation of the fibres in the composites is important since fibres have their highest mechanical properties along their lengths and not across their widths. Consequently, composite materials have highly anisotropic properties. This means that the mechanical properties of the composites differ, unlike metals, when tested in different directions. Hence, it is important to understand the influence of the magnitude and the loading angle when considering the use of composite materials.

2.2.1. Carbon Fibre

Carbon fiber is made out of thin, strong crystalline filaments of carbon which are used to strengthen the material. It is produced by the controlled oxidation, carbonization and graphitization of carbon-rich organic precursors. The most popular precursor used for that process is polyacrylonitrile.
Carbon fibres are normally categorized according to the modulus band in which their properties fall. The following bands are commonly used: standard modulus, intermediate modulus, high modulus and, ultra high modulus [1]. The filament diameter of almost all types is about 5-7 µm. Moreover, carbon fibre possesses the highest specific

stiffness of any available fibre, a very high strength in tensile and compression, a high resistance to corrosion, fatigue, and creep. Nevertheless, the impact strength is lower than fiber glass. In tables 2.4 -2.1 a few examples for each band are listed.

Table 2.1.: Standard modulus (< 265 GPa).

Grade	Tensile Modulus [GPa]	Tensile strength [GPa]
T300	230	3.53
T700	235	5.3

Table 2.2.: Intermediate modulus (265-320 GPa).

Grade	Tensile Modulus [GPa]	Tensile strength [GPa]
T800	294	5.94
T40	290	5.65

Table 2.3.: High modulus (320-440 GPa).

Grade	Tensile Modulus [GPa]	Tensile strength [GPa]
HMA	358	3.0
UMS2526	395	4.56

Table 2.4.: Ultra high modulus (> 440 GPa).

Grade	Tensile modulus [GPa]	Tensile strength [GPa]
UHMS	441	3.45
UMS3536	435	4.5

2.2.2. Glass

Liquid glass is formed by blending quarry products (e.g., coelmanite, sand) at 1,600°C. This liquid passes then through micro-fine bushings and is cooled down. Glass fibre filaments with a diameter ranging from 5 to 24µm are then produced. The filaments are drawn together into a strand and coated with a size to protect the glass from abrasion and to provide filament cohesion [1].
The following different types of glass can be produced by varying the recipe:

1. E-glass

2. C-glass

3. R, S or T-glass

E-glass is one of the most commonly used fibers for various engineering applications. E-glass[2] is stronger than A-glass[3] and has a lower alkali content. Moreover, E-glass has both a good tensile and compressive strength, good electrical properties and the manufacturing costs are cheap. However, the impact resistance of this material is relatively poor. Carbon fibre and E-glass are the most common forms of reinforcing fibres used in polymer matrix composites due to their low costs [1].

2.3. Loads

In total, there are four main direct loads that a material in a structure is subjected to and has to withstand:

1. Flexure
2. Compression
3. Shear
4. Tension

The cylinders are tested under compression in this research. Hence, the compression load will be elaborated in the following section.

2.3.1. Compression

In a compressive loading condition, the stiffness and adhesive properties of the resin system are essential. The resin system is supposed to keep the fibres straight and to prevent fibre buckling. In Figure 2.1, a composite subjected to a compressive loading is shown.

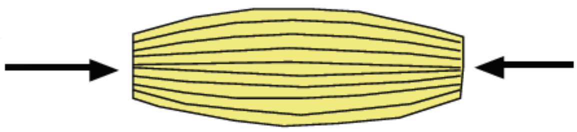

Figure 2.1.: Compressive loading [1].

[2] Electrical glass.
[3] Alkali glass.

2.4. Stress and Strain

The strength of a material is defined as the ability to withstand a specific load before the material fails (ultimate strength). Before a laminate[4] completely fails, a specific stress level has to be reached. At this level, the resin starts to crack from the fibres that are not aligned with the load. Consequently, these cracks will grow and spread through the resin matrix. This process is also known as microcracking. At this point, the resin shows a breakdown and the fibres will fail. The laminate has not failed yet; however, the breakdown process has started already.

The maximum possible strain a laminate is able to withstand before microcracking occurs depends on the adhesive properties of the resin system. For most polyesters, which are classified as a brittle resin system, microcracking takes place long before the laminate failure. Therefore, the possible strain of a laminate is limited.

In Figure 2.2, a typical stress-strain graph of a fibre-reinforced polymer is shown. Just a small deformation causes the first debonding and microcracking. The breakdown process starts at this point while a failure of the laminate has not occurred yet. The tensile stress is increased, which leads to an increased deformation and strain. While the slope gradient of the straight line in the first segment is high, the slope gradient in the second segment is slightly lower. The strain increases until the ultimate tensile strength point is reached. At this point the laminate fails abruptly.

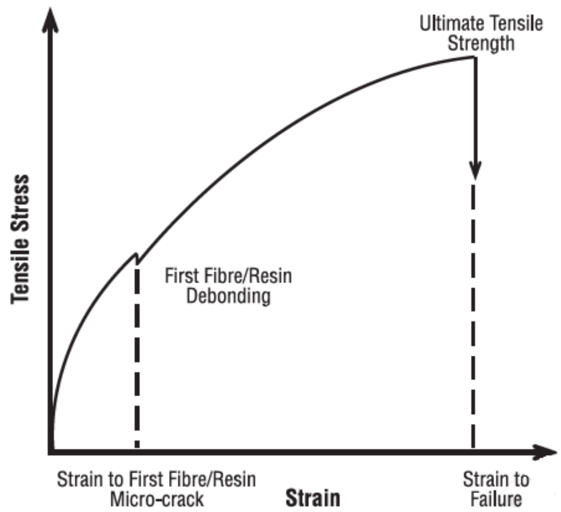

Figure 2.2.: Stress-strain graph of a typical fibre-reinforced polymer [1].

[4] Multiple assembled layers of fibrous composite materials.

3. Manufacturing of the Specimen and Experimental Test Setup

Many researchers and advanced material industries have recognized the composite material as a potential engineering material. Composite materials can replace the conventional and general materials in producing lightweight, low-costs products that need a high material strength. Various techniques for manufacturing composite materials exist so far. The most common techniques are:

1. Hand Lay-Up and Spray-Up
2. Pultrusion
3. Injection Molding
4. Resin Transfer Molding
5. Filament Winding [4]

The specimen used in the experiments are manufactured using the filament winding technique. Consequently only the filament winding technique will be elaborated in more detail.
Filament winding is a mature manufacturing process that produces a wide range of moderate and high mechanical performance parts. The first filament winding machine was used in 1950 in accordance with the revolutions of the filament winding application. Today, filament-wound applications are used to make pipe-shaped or tube-shape products, like rocket motor cases, launch tubes, and high-pressure storage tanks. However, filament-wound products can also be used for commercial equipment such as fishing rods, golf club shafts, and tennis rackets. Moreover, the filament winding method is also used for generally circular, hollow or oval sectioned components.
The following sections describe the filament winding process and give an overview of the compression test setup used for this thesis.

3.1. Filament Winding Process

The basic filament winding process is shown in Figure 3.1. T700 Carbon fibres preimpregnated with UF3325 resin are used to wind the cylindrical specimens tested in the experiments.
During the filament winding process, tows or fibre strands are wound and constantly passed through the resin bath, if they are not previously impregnated with a resin. By passing through the resin bath, the fibre strands or tows are impregnated with the epoxy

or the polyesters. At the end of the resin bath, the fibre strands are pulled through a wiping device where the excess resin is removed from the strands. After that, the related resin-impregnated fibre strands are wound on a rotating mandrel with a specific fibre orientation. The desired winding angle patterns are controlled by the winding speed of the mandrel and by the fibre feeding mechanism. Moreover, fibres with impregnated resin are wound around the rotating mandrel at different winding angles to satisfy mechanical requirements, such as elasticity, ductility, strength, fatigue strength, and stiffness [7]. A winding angle of ± 45° is used for manufacturing the cylinders. After the the winding process is finished, the component needs to be cured which is carried out in an oven. Afterwards the mandrel has to be removed. The used cure cycle for the UF3325 TCR Resin is as follows:

≤ 5°F-per-minute ramp up to 290°F, hold for 2 hours, <5°F-per-minute ramp down to at least 150°F before removing from oven.

The main advantages of the filament winding method are that it is fast and parts can be manufactured automatically at lower costs, compared to other techniques. Moreover, the filament winding method is highly repetitive and precise in fiber placement and large and thick-walled structures can be built.
The main disadvantages of the filament winding method is that the the shape of the component has to be selected such that it can be detached from the mandrel, the surface quality is low and the mandrel is generally complex and expensive.

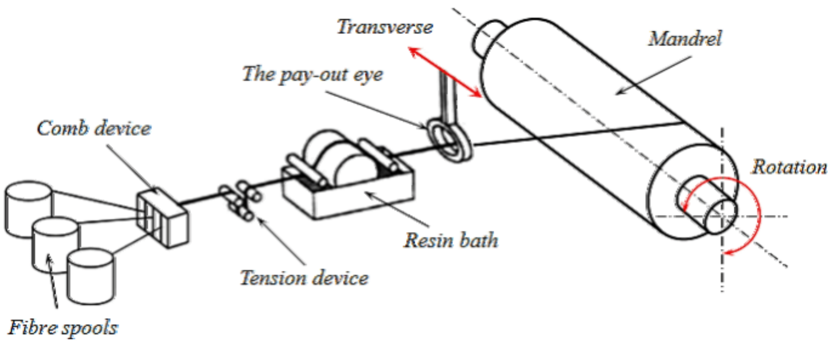

Figure 3.1.: Basic filament winding process [2].

3.2. Influence of the Winding Angle on the Compression Strength

The researchers Soden, P. D. et al. examined the influence of the winding angle on the strength and deformation of filament-wound composite tubes that are subjected to uniaxial and biaxial loads, both compression and tension [8]. For their study, they used ± 45°, ± 55°, ± 75° winding angles and compared both the tensile and compression strength of the material. They concluded that an increased winding angle leads to an increased tensile strength in the circumferential direction but decreased uniaxial tensile strength in the axial direction [8]. However, the compression strength is only influenced slightly by increasing the winding angle. The specimens were subjected to stress levels ranging from about 135 to 155 MPa.

3.3. Compression Test Setup

Two compression testing machines are used for the experiments. The Instron 5982 (Fig. 3.2) is equipped with a 100 kN load cell. A computer equipped with a data acquisition system[1] is linked to the machine. The strain rate[2] is also controlled by the computer. A strain rate of -2 $\frac{mm}{min}$ is used for tests. The force and displacement data is obtained during the test. The applied force pushes the test fixture down and compresses the cylinder. However, the clamping force of the mechanical grip was not strong enough to prevent the bottom part of the test fixture from moving and tilting. Hence, it was not possible to apply the desired force of 10,000 N and the results were distorted. Thus, the MTS 858 material testing system had to be used to solve this issue.
The MTS 858 provides a broad range of test-enhancing features and possesses the capability to perform tension, compression, fatigue, and bend tests. A force up to 10,000 N can be chosen for the material test. Because of that, the machine is perfectly suitable for testing lower-strength materials (e.g., plastics, aluminum). Moreover, hydraulic grips are installed on the MTS 858 and the clamping pressure can be controlled by a switch. Consequently, the clamping of the grip is strong enough to prevent the lower part of the test fixture from undesired tilting.
The lower part is clamped in the lower grip. The middle part and the cylinder are then inserted into the recess of the lower part. After that, the upper part is clamped in the upper grip and the hydraulic actuator is carefully lifted down until the surfaces of the different parts are touching each other. A slight adjustment of the test fixture is required to ensure that the cylinder and the upper part are perpendicular.

[1] Records the load versus displacement data throughout the duration of the compression test.
[2] Rate at which the specimens are compressed.

Figure 3.2.: Compression testing machine: Instron 5982.

Figure 3.3.: The MTS 858 Material Testing System.

4. Failure Mechanics

Composite materials are used in many structural applications and are exposed to high-velocity dynamic loading and high energy, causing multiaxial dynamic states of stress. Consequently, the application of composite materials causes new challenges to the designer. The matrix of a composite material has a wide range of functions. Such functions include acting as a glue to hold the reinforcing fibres together, protecting the reinforcement from mechanical abrasion, and distributing loads among the reinforcement [9]. Especially under these and the previously mentioned loading conditions, composite materials develop nonlinear and rate-dependent behavior. Therefore, the process of fabrication, testing and modeling of composites is time consuming and impedes the introduction of new materials [10].
The failure of composite materials has been investigated over many years on microscopic and macroscopic scales. Failure initiation and failure mechanisms differ with type of loading and are related to the mechanical, physical and geometric properties of the constituent phases on a microscopic scale.
On a macromechanical, scale numerous failure theories have been proposed for analysis of composites. In this section, the basics of failure mechanics for ductile metals and composite materials will be elaborated.

4.1. Yield Criteria for Metals

The yield criteria are used to predict the failure of ductile materials. A yield criterion describes the limit of elasticity in a material and the onset of plastic deformation under any combination of stresses [3]. Many possible yield criteria exist so far. However, the von Mises Yield criterion is one of the most popular and will be explained in this chapter.

In order to understand the combination of stresses, the idea of principal stress will be introduced. Any stress can be plotted as a point in 3D stress space using the orthogonal principal stress axes (Fig. 4.1). For instance, a purely hydrostatic stress ($\sigma_1 = \sigma_2 = \sigma_3 = \sigma_H$) lies along the vector $\vec{v} = (1, 1, 1)$ in principal stress space (Fig. 4.2). Hence, yielding will not occur since plastic deformation is not induced by hydrostatic stress [3].
Yielding will occur if Y is a uniaxial stress ($\sigma_1 = Y, \sigma_2 = \sigma_3 = 0$). The hydrostatic line is surrounded by a surface (yield criterion) passing through $(Y, 0, 0)$, which defines the boundary between elastic and plastic behavior. The surface needs to pass through the points $(0, Y, 0)$, $(0, 0, Y)$, $(-Y, 0, 0)$, $(0, -Y, 0)$ and $(0, 0, -Y)$ [3]. A cylinder with an axis along the hydrostatic line and an appropriate radius meets all these requirements for a yield criterion, which is described by equation 4.1.

$$\sigma_v = \left[(\sigma_1 - \sigma_2)^2 + (\sigma_2 - \sigma_3)^2 + (\sigma_3 - \sigma_1)^2\right] \tag{4.1}$$

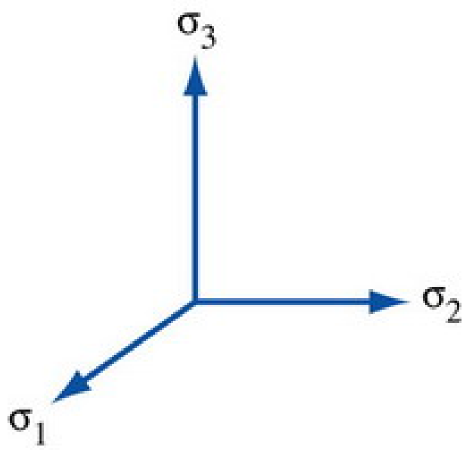

Figure 4.1.: Orthogonal principal stress axes [3].

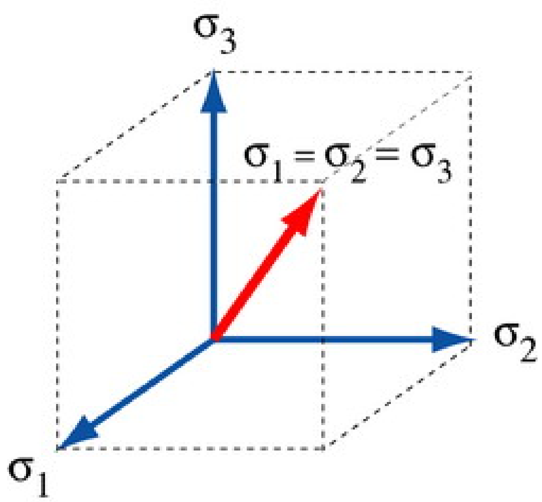

Figure 4.2.: Purely hydrostatic stress [3].

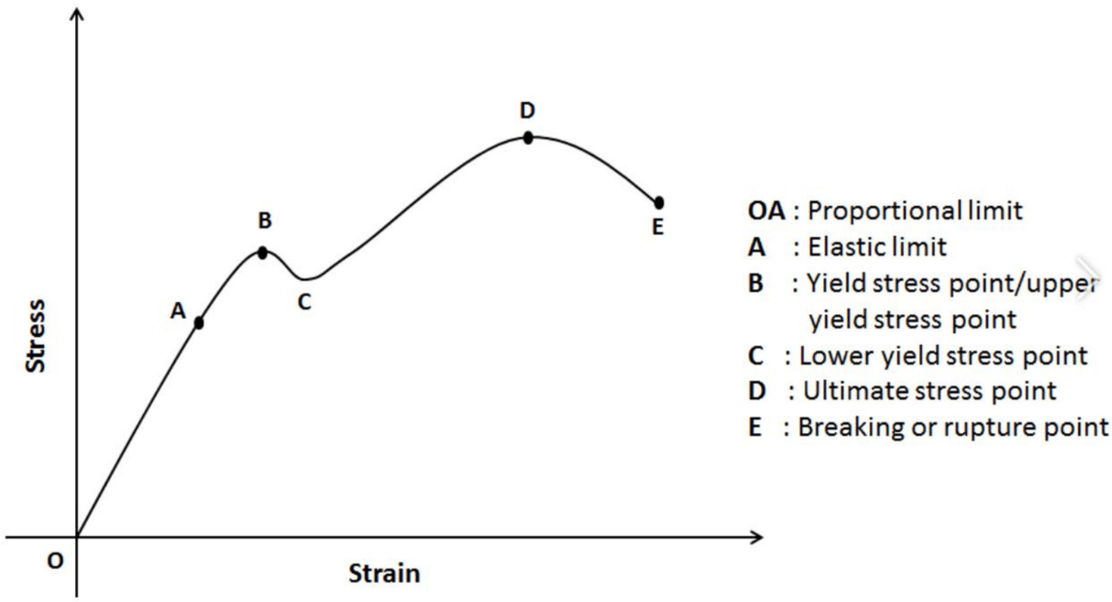

Figure 4.3.: A typical stress-strain graph [4].

In Figure 4.3, a typical stress/strain graph is shown. The different segments (A-E) of the material response can be seen. When a load is applied, the material will follow an elastic behavior and stay within the elastic limit (A). If the applied load will now be incrementally increased, the material will reach the yield stress point (B). At this point, the material starts to deform both plastically and elastically. Prior to reaching the yield point, the material will return to its original shape when the applied stress is removed. After passing the yield point, some fraction of the deformation will be permanent and non-reversible. The deformed material will not return to its original shape when the applied stress is removed. However, a quantity called yield strength[1] is used for many materials that do not have a well-defined yield point. Some materials start yielding or to flow plastically at a defined stress, upper yield point (B), that falls rapidly to a lower steady value, lower yield point (C) as deformation continues. This issue is shown in the stress/strain graph (Fig. 4.3). When the load is increased after the yield point is reached, a greater plastic deformation will occur, which can lead to a fracture (E).

4.1.1. Influencing Factors of the Yield Strength

The yield strength depends on both the strain rate and the temperature at which the deformation occurs. Usually, the yield strength increases with strain rate and decreases with higher temperatures. However, if it is not the case, the material exhibits yield strength anomaly. This is typically for super alloys (e.g., Hastelloy, Inconel, Incoloy, etc.). Therefore, they are used in applications requiring high strength at high tempera-

[1] The stress at which materials have undergone an arbitrarily chosen amount of permanent deformation is called yield strength. The deformation is often around 0.2 %.

tures such as turbines.
The complex relationship between the yield strength, the strain rate and the temperature is shown in equation 4.2:

$$\sigma_y = \frac{1}{\alpha} sinh^{-1} \left[\frac{Z}{A} \right]^{\frac{1}{n}} \tag{4.2}$$

where Z is the Zener-Hollomon parameter[2], and α and A are constants. In equation 4.3, the Zener-Hollomon parameter is described:

$$Z = (\dot{\epsilon}) exp \left(\frac{Q_{HW}}{RT} \right) \tag{4.3}$$

where ϵ is the strain rate, R is the gas constant, T is the absolute temperature and Q_{HW} is the activation energy for hot deformation.

4.2. Composite Failure Modes

The study of composite materials is a relatively new branch of engineering. Today much of the material properties and material behavior are well understood. However, much research continues on modeling the compressive strength because of its complexity.

Many factors (e.g., layup, loading, material imperfections—see chapter 2.2) can contribute to compressive failure. Therefore, empirical models are often developed around experimental data sets. The failure of composites is often determined by compressive stresses because the compressive strength is lower than the tensile strength.
A failure of a composite can basically be described by two phases: elastic phase and inelastic phase. During the elastic phase, damage does not appear in the structure, while damage will occur at certain stress levels during the inelastic phase.

Especially for multilayered composites, the damages can be classified in the following four types:

1. Microcracking of the matrix
2. Debonding
3. Delamination
4. Fibre breakage [11]

Microcracking of the matrix occurs when the resin starts to crack from the fibres that are not aligned with the load. These cracks will grow and spread through the resin matrix. A debonding failure can be caused by the separation of the interface between the fibers and the matrix or by a crack.

[2]Helps to describe high temperature creep strain of a material such as steel.

Delamination is one of the predominant forms of failure in laminated composites. Applied loads perpendicular to the layers and shear loads cause a separation of the laminae from each other. This separation leads to a lack of reinforcement in the thickness direction.
As a consequence of high stresses or sudden rise in temperatures, fibre breakage can occur. The mechanical performance of the composite material can be damaged when fibre breakage occurs. Moreover, breaking of the fibres is generally one of the last processes towards the final material failure [11].

4.2.1. Composite Failure Theories

Composite failure theories are required for predicting the strength of any laminated composite. Numerous failure theories have been proposed so far. They can be classified into the following three groups:

1. Failure mode-based theories (Hashin-Rotem, Puck)
2. Limit or non-interactive theories (max. strain, max. stress)
3. Interactive theories (Tsai-Wun, Tsai-Hill) [12]

Failure mode-based theories take the non-homogeneous character of composites into account. This non-homogeneous character of composites leads to different failure modes of a structure. The criteria are defined by mathematical expressions, which include the material strengths, and include the different failure modes of the structures. Therefore, the criteria can be used in a progressive damage analysis [12].
The following failure modes are covered by the criteria:

1. Shear matrix cracking.
2. Transverse matrix cracking.
3. Fibre fracture.

However, the failure mode-based theories can be further divided into the following two subgroups: interactive and non-interactive theories.
Non-interactive theories do not include the interactions between stresses and strains acting on a lamina. This lack of interactions leads to errors in the strength prediction when multi-axial states of stress in a structure occur. The limit or non-interactive theories are simple to apply and provide the mode of failure. However, they neglect the effect of stress interactions [13]. Therefore, these theories should only be used conservatively.
The interactive theories include the interactions between stresses and strains acting on a lamina in the failure mechanism and predict the first ply failure. However, for these theories, specific required parameters have to be determined. Moreover, these theories are more suitable for predicting failure of a single lamina.
The correct selection of a given theory depends on the convenience of application and

agreement with experimental results. The maximum stress and strain theories will be discussed in chapters 4.2.2 and 4.2.3 in more detail. These theories are extensively used in the industry because of their simplicity. Moreover, these theories comprise a simple and fast way to predict the failure of composite. However, the results should only be used as an overview or very conservatively.

4.2.2. Maximum Stress Theory

This theory uses uniaxial test data to predict the failure of the laminate. The theory considers only the ultimate strength of the laminate in a particular direction for the particular type of failure [14]. The composite fails when the stress exceeds a specific allowable value. No interaction between the stresses acting on the lamina is considered in this theory.
Three different failure conditions are described by the theory (see eqs. 4.4, 4.5, 4.6). If equation 4.4 is satisfied, then damage to the fibres will occur. If equation 4.5 is satisfied, then damage to the matrix is caused by the stress. If equation 4.6 is satisfied then shear stress occurs and delamination or debonding might occur. These equations are listed below:

$$|\sigma_{11}| \geq \sigma_{1C}^{u} \tag{4.4}$$

$$|\sigma_{22}| \geq \sigma_{2C}^{u} \tag{4.5}$$

$$|\tau_{12}| \geq \tau_{12C}^{u} \tag{4.6}$$

where σ_{1C}^{u}, σ_{2C}^{u} are the ultimate normal compressive stresses in the X, Y direction and τ_{12}^{u} is the ultimate shear stress in the XY plane. σ_{11}, σ_{22} are the normal stresses in the X, Y direction and τ_{12} is the shear stress in the XY plane.

4.2.3. Maximum Strain Theory

According to the maximum strain theory, the composite will fail when the strain exceeds a specific value. It is a simple and easy way to predict the material failure of composites. Three different failure conditions are described by the theory (see eqs. 4.7, 4.8, 4.9). If equation 4.7 is satisfied, then damage to the fibres will occur. If equation 4.8 is satisfied, then damage to the matrix is caused by the stress. If equation 4.9 is satisfied, then shear stress occurs and delamination or debonding might occur. The equations are as follows:

$$|\epsilon_{11}| \geq \epsilon_{1C}^{u} \tag{4.7}$$

$$|\epsilon_{22}| \geq \epsilon_{2C}^{u} \tag{4.8}$$

$$|\epsilon_{12}| \geq \epsilon_{12C}^{u} \tag{4.9}$$

where ϵ^u_{1C}, ϵ^u_{2C} are the ultimate compressive strain along the X, Y direction and ϵ^u_{12} is the ultimate shear stain. ϵ_{11}, ϵ_{22} are the strain along the X, Y direction and ϵ_{12} is the shear strain.

5. Numerical Modeling of the Test Fixture

In this chapter, the numerical modeling is explained in detail. The goal of the numerical analysis is to predict the failure of the cylinders subjected to compression loading. Moreover, the aim of this chapter is to investigate the influence of different loading angles on the stress and strain distribution and material strength. Different offsets of 0°, 5°, 10°, and 15° are used for the analysis.
Ansys[1] is used for the analysis. Stainless steel is used for test fixture and at first an aluminum alloy cylinder is used for the analysis. After that, a composite cylinder is used for the analysis. The detailed material properties of the stainless steel, of the aluminum alloy and the composite material used in the finite element analysis are shown in tables A.1, A.2, A.3 and A.4.
In the following sections, the implementation and modeling of the test fixture, which was originally constructed in SolidWorks, will briefly be described.

5.1. Modelling using SolidWorks

The whole test fixture is shown in Figure 5.1, and a section view of the fixture is shown in Figure 5.4. The technical drawing of each seperate part of the fixture can be seen in figures B.1, B.2, B.3, and B.4.
The test fixture consists of three parts: the upper, middle, and lower part. The upper and lower part are clamped in a grip of the compression testing machine. Then the middle part is inserted into the bottom of the cylinder (Fig. 5.3). The upper part of the fixture is then inserted into the top of the cylinder, to increase the buckling stability (Fig. 5.4).
However, the test fixture had to be slightly edited to make an offset of more than 12° possible. Therefore, the edges of hemispherical recess in the lower part needed to be rounded. The radius of the fillet was 0.1 in.
The lower part is then moved by using the rotate component feature and rotating the lower part around the Z-axis. The desired rotating angle can be defined by the user. Afterwards the model can be saved and exported as a .sat file using SolidWorks. For each different offset angle, a new SolidWorks file needs to be created and a new .sat file exported.

[1] A finite element analysis software used for the simulation of engineering problems.

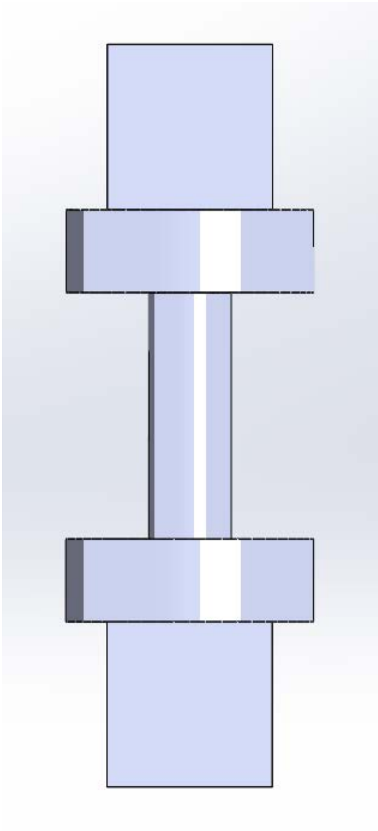

Figure 5.1.: Composite compression test fixture for filament-wound cylinders.

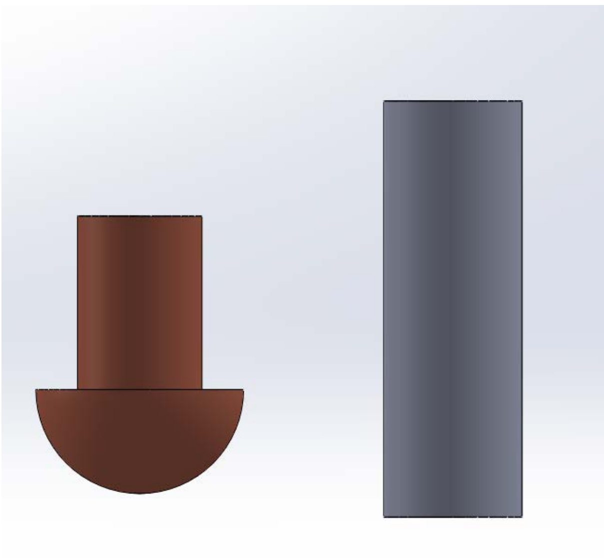

Figure 5.2.: Cylinder and middle part.

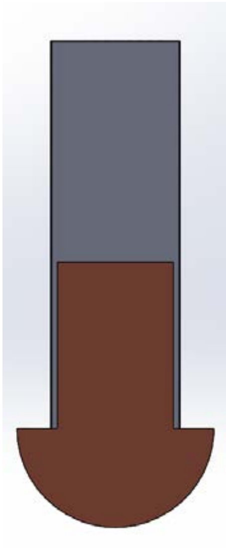

Figure 5.3.: Section view of cylinder inserted into the middle part.

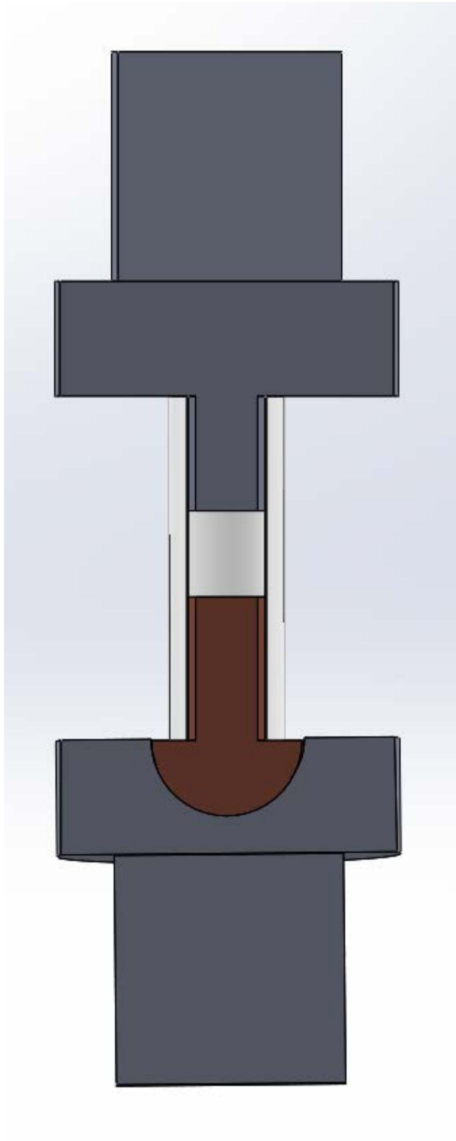

Figure 5.4.: Section view of the whole test fixture.

5.2. Implementation and Modelling of the Test Fixture in Ansys

A new project needs to be created in Workbench.[2] After selecting the static structural analysis system, the engineering data (material properties) can be defined, the geometry can be imported using the .sat file and the FEM model can be set up.

[2]A software environment of Ansys used for performing structural, electromagnetic, and thermal analyses.

A correct FEM model setup is important because the results of the analysis are directly affected by the setup. The setup consists of different steps, which will be elaborated in the following subsections:

1. Material property
2. Geometry and correct material assignment
3. Defining contact regions
4. Meshing of the geometry
5. Defining the boundary conditions
6. Selecting the desired solving options and the desired equations the user wants to be solved

5.2.1. Material Property

An important aspect for simulations is to know the exact material properties for the problem. An aluminum alloy cylinder cannot be simulated using steel properties. The elasto-plastic behavior of materials can be described by many models [15]. It is important to know the theory before using the different models since each model has its own characteristic and is appropriate to a certain type of problem. Some basic models are listed below:

1. Linear elastic
2. Elastic-perfectly plastic
3. Elasto-plastic with linear or nonlinear hardening
4. Istotropic or kinematic hardening

The multilinear isotropic hardening model is used in this thesis to implement the non-linear material response in the finite element analysis. This model can be used in large-strain analyses where kinematic hardening could exaggerate the Bauschinger effect,[3] in simulations of metal plasticity behavior under noncyclic loading or for those elements that do not support the multilinear kinematic hardening option. A piecewise linear total stress-total strain curve that starts at the origin with positive stress and strain values describes the uniaxial behavior starting at the origin [16]. This curve is continuously from the origin through max. one hundred material-specific stress-strain points defined by the user. The slope of the first segment of the curve has to correspond to the elastic modulus of the material and the slope of any other segment should not be larger [16].

[3]Effect by which the yield strength of a metal is increased by plastic deformation in the direction of plastic flow and is decreased in the opposite direction.

The isotropic hardening option uses the von Mises yield criteria (chapter 4.1) combined with an isotropic work-hardening assumption. The parameters of the multilinear isotropic hardening model used for the analysis of the aluminum cylinders are shown in table A.2.
The mulitlinear kinematic hardening model is the direct opposite and simulates plasticity behavior under cyclic loading.

5.2.2. Geometry, Material Assignment, and Contact Regions

After implementing the geometry, the material needs to be assigned to each part of the test fixture. Stainless steel is assigned to the upper, middle, and lower part. The desired aluminium alloy and later on the desired composite is assigned to the cylinder.

After that, it is important to check if the contact regions of the assembly are correctly imported. Beside that, the user needs to select the contact and target body for each contact region. A target body can penetrate a contact body, but a contact body is constrained against penetrating the target surface. There are three contact regions in total:

1. Contact region between the upper part and the cylinder (Fig. 5.5)
2. Contact region between the middle part and the cylinder (Fig. 5.6)
3. Contact region between the middle part and the lower part (Fig. 5.7)

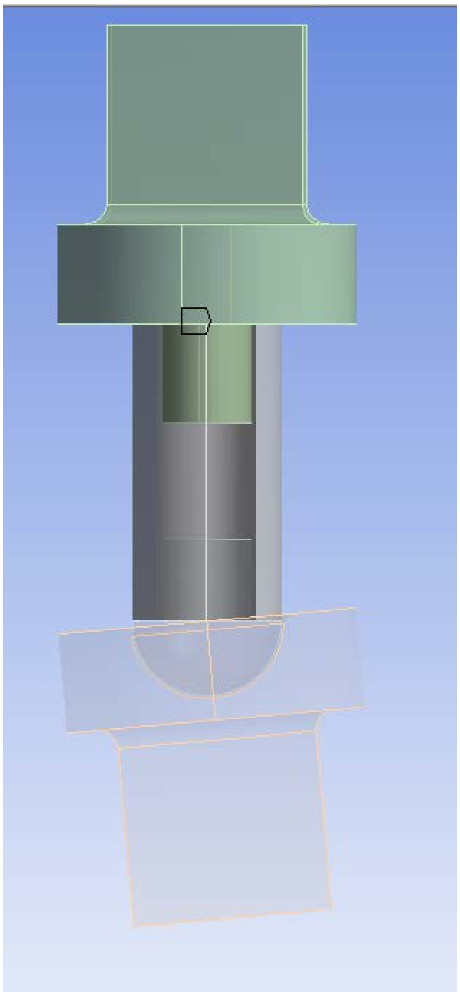

Figure 5.5.: Contact region 1.

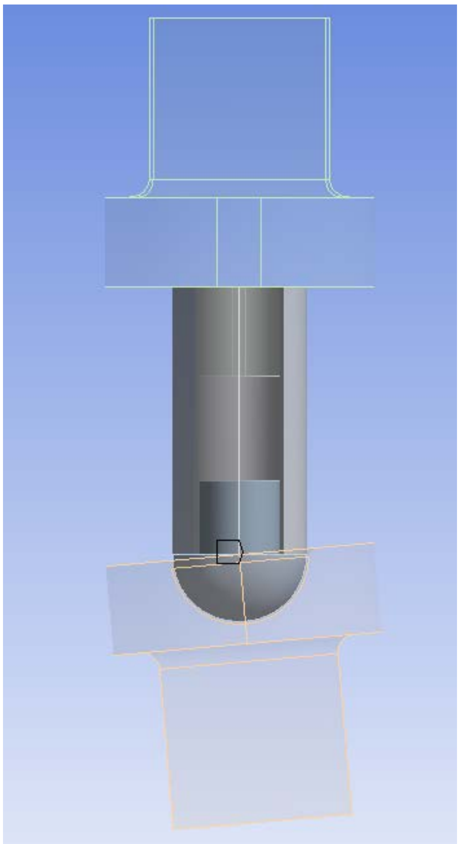

Figure 5.6.: Contact region 2.

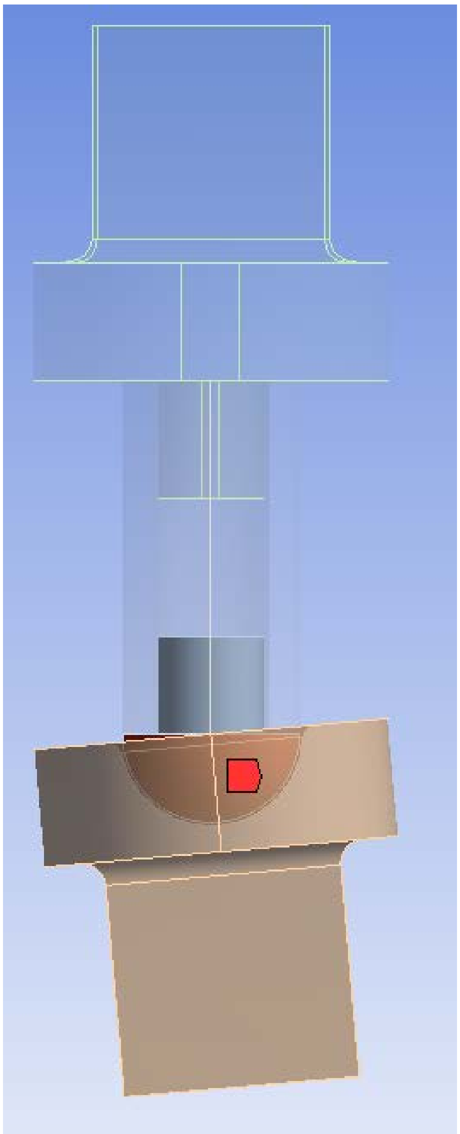

Figure 5.7.: Contact region 3.

5.2.3. Meshing of the Geometry

A correct meshing is needed to obtain a good solution. For this analysis, the tetrahredon, hexahedron, or the automatic meshing method can be used. The tetrahedron meshing method is more precise than the hexahedron method, compared to the analytical solution when analyzing tension and bending stresses. The contact regions can be meshed, too. Leaks discovered during meshing can be closed using the contact sizing method. A leakage is caused if any contact is larger than $\frac{1}{10}$ of the local minimum size.

The automatic method is used for the numerical analysis and the upper, lower part, and the cylinder are meshed using the body sizing function. The body sizing function gives a greater control over the distribution of the mesh size on a face or within a body. If turned on, a much more accurate sizing information to the mesher is provided. The middle part is meshed using the contact sizing function.

5.2.4. Defining the Boundary Conditions

A fixed support condition aligned with the offset of the lower part is assigned to the lower part. The effective direction of the fixed support can be seen in Figure 5.8. The test fixture is tilted to give a better view of the assigned boundary conditions.

The force is modeled using a force condition applied on the surface of the upper part. A force can either be applied on a vertex, an edge or a face. However, for this thesis the force is applied on the face, which distributes a force vector across one or more flat faces. The effective direction of the loading condition is perpendicular and acts along the Y-axis (Fig. 5.9).
In the analysis settings branch, large deflections can either be turned on or off. Activating large deflections will implement different nonlinear behaviors, like large strain, stress stiffening, spin softening, and large rotation in the solving process. The large deflection option has to be turned on for the simulations conducted for this thesis.

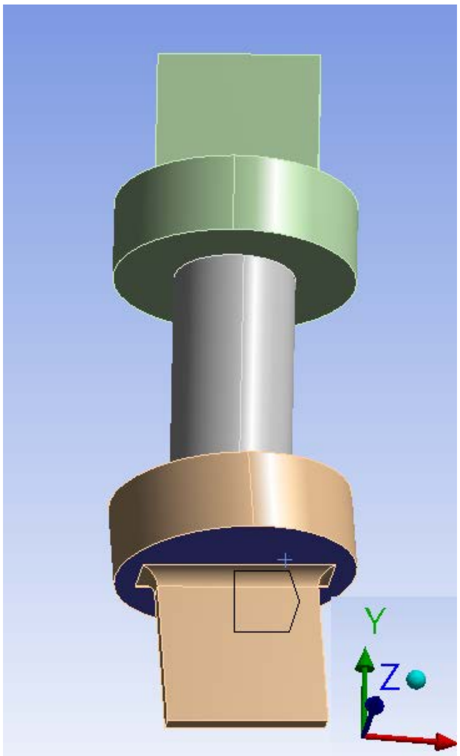

Figure 5.8.: Boundary condition: fixed support.

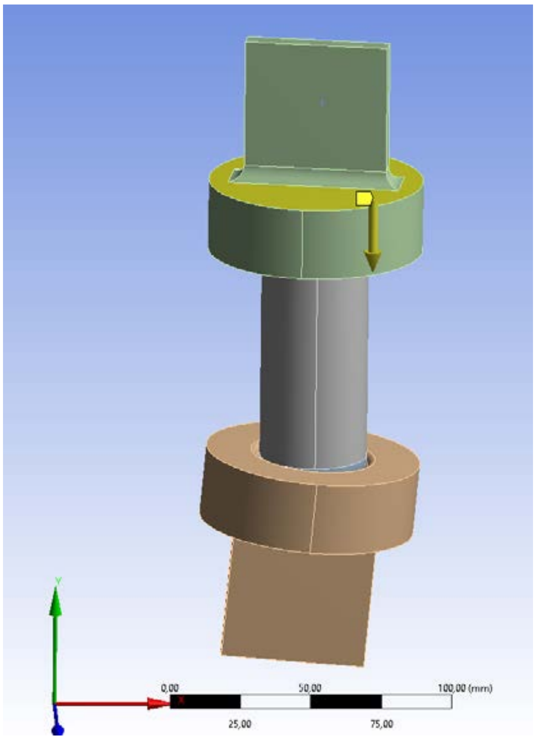

Figure 5.9.: Boundary condition: force (Y-axis is colored green).

5.2.5. Selecting the Desired Solving Options

The user can select different output options regarding the results he wants to obtain. Different deformation, stress, and strain results can be obtained.
The stress and strain distribution are relevant for this analysis. It is possible to predict safety factors, stresses, strains, and displacements for a particular structural loading environment because of the stress solutions [17]. Additionally, the physical deformations of the cylinders are also of interest for this thesis.

Deformations

Deformations are calculated relative to the part or assembly coordinate system [5]. The deformation data of each component U_x, U_y, and U_z can be retrieved. The deformed shape U can be calculated using equation 5.1. In Figure 5.10, the three different components U_x, U_y, and U_z and the deformed shape U are shown.

$$U = \sqrt{U_x^2 + U_y^2 + U_z^2} \tag{5.1}$$

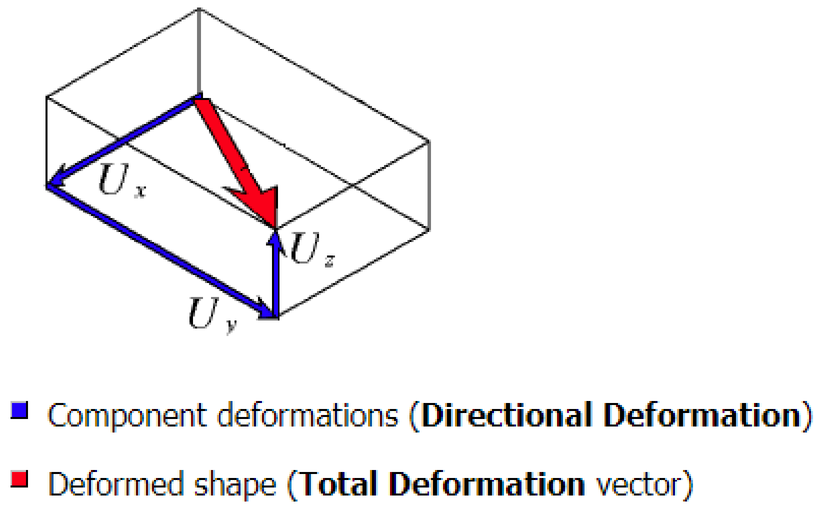

Figure 5.10.: Three component deformations [5].

Stress and Strain

The following stress and strain solutions are of interest for the numerical simulation of the compression tests:

1. Equivalent (von Mises)
2. Maximum, middle, and minimum principal

The equivalent stress, which is a part of the maximum equivalent stress failure theory, can be related to the principal stresses by using equation 5.11. The von Mises yield criterion is often used to predict yielding in a ductile material. Moreover, the equivalent stress allows any three-dimensional stress state to be represented as a single positive stress value. Therefore, it is commonly used in design work [18].
According to the elasticity theory, an infinitesimal volume of material at an arbitrary point on a solid body can be rotated such that only normal stresses remain and all shear stresses are zero. These three normal stresses that remain are called principal stresses [6]. The direction of each principal stress component is shown in Figure 5.11. The principal stresses are ordered such that $\sigma_1 > \sigma_2 > \sigma_3$. Hence, each principal stress is named as follows:

σ_1 - Maximum

σ_2 - Middle

σ_3 - Minimum

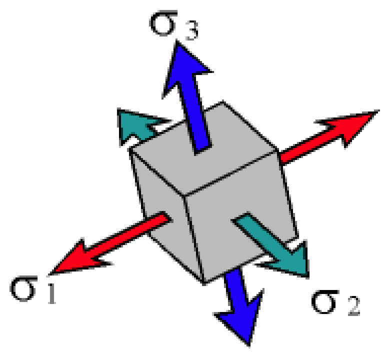

Figure 5.11.: Directions of the principal stresses [6].

von Mises Yield Criterion

The von Mises Yield criterion is based on the determination of the distortion energy in a given material. The material will not fail as long as the maximum value of the distortion energy per unit volume remains smaller than the distortion energy per unit volume needed to cause yield in a tensile test specified of the same material.
The yield function for the von Mises condition can be mathematically expressed as derived from the following equations:

$$f(J_2) = \sqrt{J_2} - k = 0 \qquad |^2; +k \tag{5.2}$$

$$J_2 = k^2 \tag{5.3}$$

where k is the yield stress of a material in pure shear [19]. At the onset of yielding, the magnitude of the shear yield stress in pure shear is $\sqrt{3}$ times lower than the tension yield stress. Therefore, k can be defined as shown in equation 5.4:

$$k = \frac{\sigma_y}{\sqrt{3}} \tag{5.4}$$

where σ_y is the tensile yield strength of the specific material. If the von Mises stress σ_v is set equal to the tensile yield strength and inserted into equations 5.3 and 5.4, the von Mises yield criterion is derived in the following equations and can be expressed as shown in equation 5.9:

$$k = \frac{\sigma_v}{\sqrt{3}} \tag{5.5}$$

$$\sqrt{J_2} - k = 0 \qquad |insert\ k \tag{5.6}$$

$$\sqrt{J_2} - \frac{\sigma_v}{\sqrt{3}} = 0 \qquad | + \frac{\sigma_v}{\sqrt{3}};\ * \sqrt{3} \tag{5.7}$$

$$\sigma_v = \sqrt{3J_2} \tag{5.8}$$

$$\sigma_v = \sigma_y = \sqrt{3J_2} \tag{5.9}$$

Substituting J_2 with the Cauchy stress sensor components in terms of the principal stresses (Fig. 5.11) leads to the following equation [19]:

$$\left[(\sigma_1 - \sigma_2)^2 + (\sigma_2 - \sigma_3)^2 + (\sigma_1 - \sigma_3)^2\right]^{\frac{1}{2}} = 6k^2 = 2\sigma_y^2 \tag{5.10}$$

where σ_1, σ_2, and σ_3 are the principal stresses.

The von Mises stress σ_v, which is obtained during the numerical analysis, is used to predict yielding of the cylinders under multiaxial loading conditions. In equation 5.11, the mathematical formulation of the von Mises stress is shown [19]:

$$\sigma_v = \left[\frac{(\sigma_1 - \sigma_2)^2 + (\sigma_2 - \sigma_3)^2 + (\sigma_3 - \sigma_1)^2}{2}\right]^{\frac{1}{2}} \tag{5.11}$$

The equation of the equivalent strain ϵ_e is shown in equation 5.14:

$$\epsilon = \frac{\Delta L}{L} \tag{5.12}$$

$$\nu = -\frac{\epsilon_{lateral}}{\epsilon_{axial}} \tag{5.13}$$

$$\epsilon_v = \frac{1}{1+\nu'}\left(\frac{1}{2}\left[(\epsilon_1 - \epsilon_2)^2 + (\epsilon_2 - \epsilon_3)^2 + (\epsilon_3 - \epsilon_1)^2\right]\right)^{\frac{1}{2}} \tag{5.14}$$

where ϵ_1, ϵ_2, and ϵ_3 are the principal strains. The definition of ϵ can be found in equation 5.12. ν' is the effective Poisson's ratio and is defined in equation 5.13.

6. Results of the Compression Testing of the Aluminum Alloy Cylinders

In this chapter, the different experimental compression tests of the aluminum alloy cylinders, which are conducted by varying the loading angle, are described. After that, the results of the tests are presented and then the results of each experiment are discussed. Moreover, the experimental compression tests of the aluminum alloy cylinders are conducted to compare the numerical results (see Chapter 9) with the experimental results and to verify the numerical results.

For this research, the influence of the strain on each side of the cylinder with an increasing offset is the focus. Consequently, four precision linear strain gauges have been attached on each specimen. The strain gauges are attached in the middle of each side of the cylinder to measure the strain of each side separately and are shown in the figures of each subsection.

The FEM strain was computed along the longitudinal direction of the front side of the cylinder. In Figure 6.1, the previously described location is shown by the green line.

The bottom part of the test fixture has to be clamped with an offset in the lower hydraulic grip to vary the loading angle. However, the bottom part started to slip in the grip when clamped with an offset of 5° or greater in the grip. The slipping is more severe with increasing offset and increasing loadings. Therefore, the applicable force varies for each loading angle. Hence, the results can be compared up to the specific applied force.

In Figure 6.2, the different stress/strain graphs, which are determined of the force/displacement data of the compression testing machine are combined in one graph to provide a first overview.

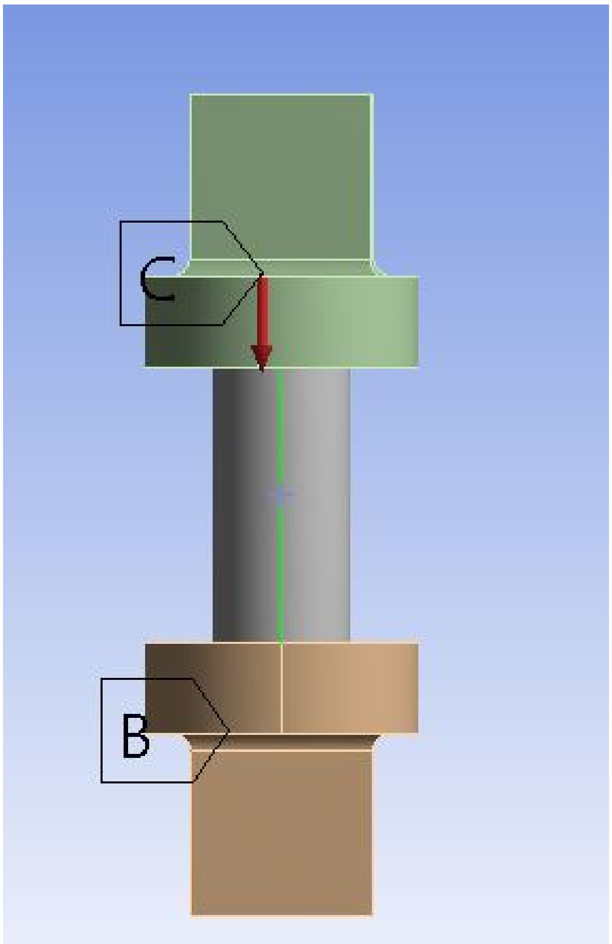

Figure 6.1.: Location of the computational determined FEM strain.

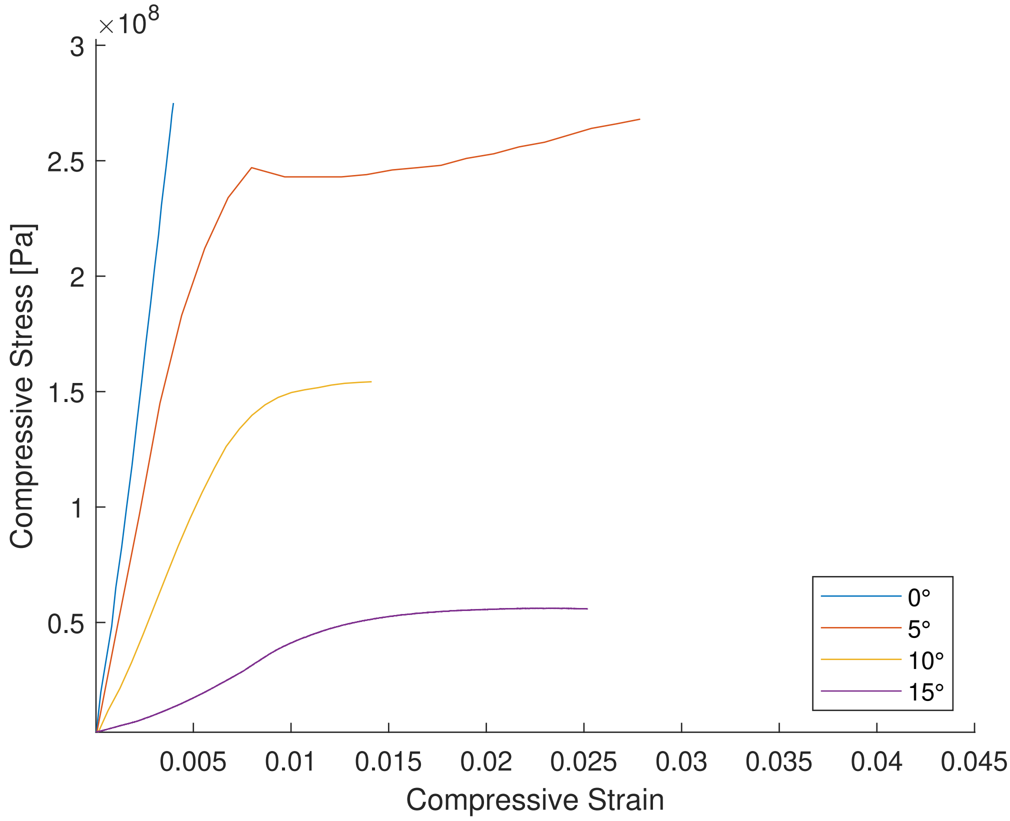

Figure 6.2.: Comparison of the different stress/strain graphs, different loadings.

6.1. Result of Compression Test Using an Offset of 0°

In Figure 6.3, the test fixture clamped in the two hydraulic grips of the compression testing machine is shown. In this figure, the strain gauges attached to the specimen can also be seen and are labeled. SG1[1] is indicated by the blue arrow, SG2 is pointed by the red arrow, SG3 is on the opposite side of SG1 and SG4 is on the opposite side of SG2. The measured values of each strain gauge are plotted in relation to the stress depicted in Figure 6.4. This figure also plots the average strain and the numerical stress/strain curve for comparison.

The values of the applied force, the determined stress, the strain gauges, and the average strain can be found in table 6.1. The calculated stress and strain data of the numerical analysis can be found in table 6.2 to facilitate comparison of the results obtained by the experimental test and the numerical analysis.

The specimen was subjected to a compression load of 9,610.0 N. A maximum stress of $\sigma_{max} = 275$ MPa and an average strain of $\epsilon_{avg} = 4.91 \times 10^{-3}\,\frac{\text{mm}}{\text{mm}}$ occurred when the force was applied. At $\sigma_{max} = 275$ MPa, the maximum measured strain occurred in SG1 with a value of $\epsilon = 2.191 \times 10^{-3}\,\frac{\text{mm}}{\text{mm}}$, while the minimum measured strain occurred in SG4

[1] Strain gauge.

with a value of $\epsilon = 1.971 \times 10^{-3}\,\frac{\text{mm}}{\text{mm}}$.
All six lines rise all linearly. The average strain line and the FEM line are almost parallel to each other. Moreover, the four SG lines are parallel to each other.
The slope of the FEM line is lower than the slope of the SG lines because the Young's modulus was assumed and is lower than the actual Young's modulus. The average strain line differs from the SG line because the strain was calculated from the measured displacement of the compression testing machine. This displacement is measured from grip to grip. Consequently, the average strain is higher than the actual strain measured by the SGs.
A plastic deformation did not occur because σ_{max} is less than the yield strength of the material $\sigma_y = 276$ (see Eq. 6.1). Thus, the specimen shrinks back to its original size after removing the load.

$$\sigma_{max} \leq \sigma_y \tag{6.1}$$

Figure 6.3.: Compression test setup at 0° offset.

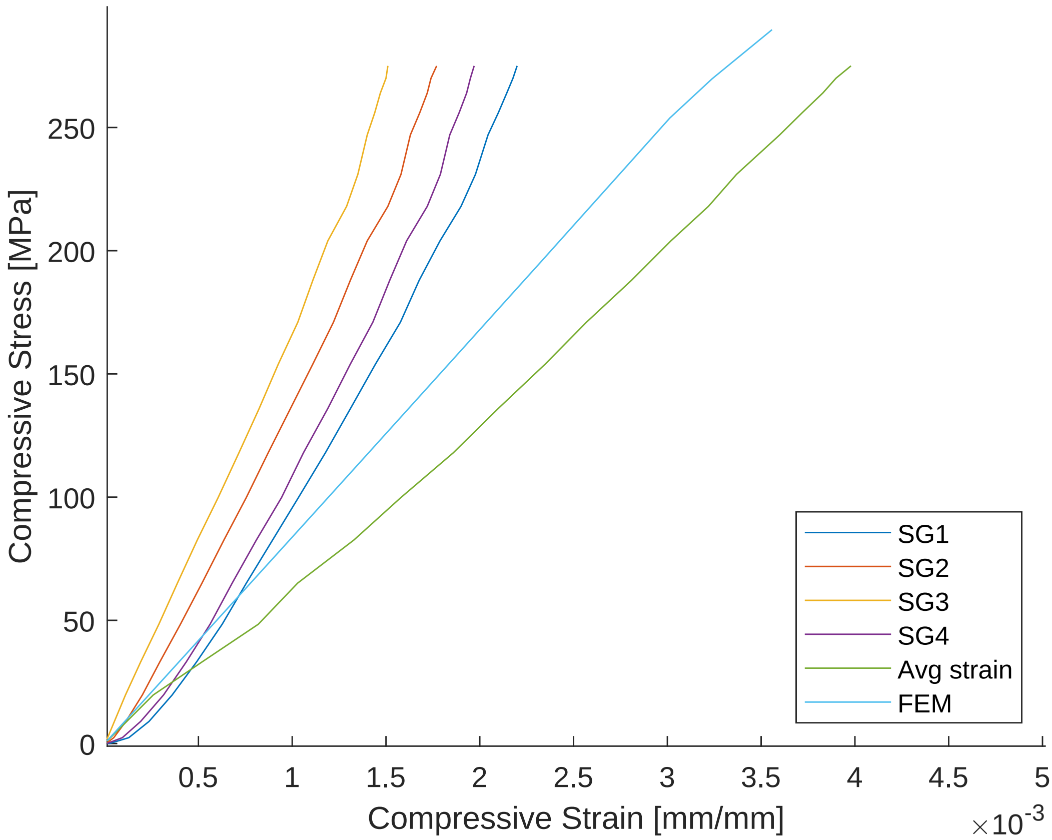

Figure 6.4.: Stress/strain graph 0° offset, loading 9,610.0 N.

Table 6.1.: Experimental determined stress and strain of the aluminum cylinder 0° offset, 9,610.0 N.

F [N]	σ [MPa]	SG1 $[\frac{mm}{mm}]$	SG2 $[\frac{mm}{mm}]$	SG3 $[\frac{mm}{mm}]$	SG4 $[\frac{mm}{mm}]$	ϵ_{avg} $[\frac{mm}{mm}]$
0	0	0	0	0	0	0
1.45	0.0416	2.70×10^{-5}	8.44×10^{-6}	6.30×10^{-6}	1.28×10^{-5}	3.28×10^{-4}
83.1	2.38	1.28×10^{-4}	4.86×10^{-5}	1.58×10^{-5}	9.44×10^{-5}	6.31×10^{-4}
313	8.97	2.36×10^{-4}	1.13×10^{-4}	5.20×10^{-5}	1.92×10^{-4}	9.31×10^{-4}
689	19.7	3.59×10^{-4}	2.01×10^{-4}	1.11×10^{-4}	3.14×10^{-4}	1.19×10^{-3}
1160	33.1	4.90×10^{-4}	2.94×10^{-4}	1.92×10^{-4}	4.35×10^{-4}	1.45×10^{-3}
1690	48.4	6.26×10^{-4}	4.04×10^{-4}	2.89×10^{-4}	5.62×10^{-4}	1.75×10^{-3}
2280	65.1	7.55×10^{-4}	5.19×10^{-4}	3.88×10^{-4}	6.80×10^{-4}	1.96×10^{-3}
2890	82.6	8.95×10^{-4}	6.36×10^{-4}	4.94×10^{-4}	8.09×10^{-4}	2.26×10^{-3}
3490	99.8	1.03×10^{-3}	7.55×10^{-4}	6.05×10^{-4}	9.43×10^{-4}	2.51×10^{-3}
4120	118	1.17×10^{-3}	8.72×10^{-4}	7.16×10^{-4}	1.06×10^{-3}	2.79×10^{-3}
4740	136	1.31×10^{-3}	9.91×10^{-4}	8.24×10^{-4}	1.19×10^{-3}	3.03×10^{-3}
5370	154	1.44×10^{-3}	1.11×10^{-3}	9.26×10^{-4}	1.31×10^{-3}	3.28×10^{-3}
5990	171	1.57×10^{-3}	1.22×10^{-3}	1.03×10^{-3}	1.43×10^{-3}	3.50×10^{-3}
6570	188	1.67×10^{-3}	1.31×10^{-3}	1.11×10^{-3}	1.52×10^{-3}	3.74×10^{-3}
7120	204	1.78×10^{-3}	1.40×10^{-3}	1.19×10^{-3}	1.61×10^{-3}	3.95×10^{-3}
7610	218	1.90×10^{-3}	1.51×10^{-3}	1.29×10^{-3}	1.72×10^{-3}	4.15×10^{-3}
8070	231	1.97×10^{-3}	1.58×10^{-3}	1.35×10^{-3}	1.79×10^{-3}	4.30×10^{-3}
8630	247	2.04×10^{-3}	1.63×10^{-3}	1.40×10^{-3}	1.84×10^{-3}	4.53×10^{-3}
8950	256	2.09×10^{-3}	1.68×10^{-3}	1.44×10^{-3}	1.89×10^{-3}	4.65×10^{-3}
9210	264	2.14×10^{-3}	1.72×10^{-3}	1.47×10^{-3}	1.93×10^{-3}	4.76×10^{-3}
9430	270	2.17×10^{-3}	1.74×10^{-3}	1.50×10^{-3}	1.95×10^{-3}	4.83×10^{-3}
9610	275	2.19×10^{-3}	1.77×10^{-3}	1.51×10^{-3}	1.97×10^{-3}	4.91×10^{-3}

Table 6.2.: Numerical determined stress and strain of the aluminum cylinder 0° offset, 9,679.94 N.

F [N]	σ_v [MPa]	ϵ_v [$\frac{mm}{mm}$]
657.10	19.47	2.3291×10^{-4}
1314.14	38.94	4.6562×10^{-4}
1971.55	58.42	6.9814×10^{-4}
2629.29	77.91	9.3047×10^{-4}
3287.37	97.41	1.1626×10^{-3}
3945.79	116.92	1.3946×10^{-3}
4604.55	136.44	1.6263×10^{-3}
5434.79	155.97	1.8579×10^{-3}
5923.41	175.52	2.0893×10^{-3}
6581.50	195.02	2.3205×10^{-3}
7243.63	214.64	2.5515×10^{-3}
7904.75	234.23	2.7823×10^{-3}
8566.90	253.85	3.0132×10^{-3}
9105.16	269.80	3.2391×10^{-3}
9776.40	289.69	3.5581×10^{-3}

6.2. Result of Compression Test Using an Offset of 5°

In Figure 6.5, the test fixture clamped in the two hydraulic grips of the compression testing machine is shown. In this figure, the strain gauges attached to the specimen can also be seen and are labeled. The measured values of each strain gauge are plotted in relation to the stress in Figure 6.6. This figure also plots the average strain and the numerical stress/strain curve for comparison.
The values of the applied force, the determined stress, the strain gauges, and the average strain can be found in table 6.3. The calculated stress and strain data of the numerical analysis can be found in table 6.4 to facilitate comparison of the results obtained by the experimental test and the numerical analysis.
The specimen was subjected to a compression load of 9,380.0 N. However, the test fixture started to slip at a force of 8,490 N and a stress of $\sigma = 243$ MPa. A maximum stress of $\sigma_{max} = 268$ MPa and and an average strain of $\epsilon_{avg} = 2.911 \times 10^{-3} \, \frac{\text{mm}}{\text{mm}}$ occurred when the force was applied. At σ_{max}, the maximum measured strain occurred in SG3 with a value of $\epsilon = 6.02 \times 10^{-3} \, \frac{\text{mm}}{\text{mm}}$, while the minimum measured strain occurred in SG2 with a value of $\epsilon = 2.78 \times 10^{-3} \, \frac{\text{mm}}{\text{mm}}$.
The SG lines and the FEM line all rise linearly. Moreover, the SG lines are parallel to each other. The average strain line can be divided into two parts. The first part rises steep to $\sigma = 248$ MPa and $\epsilon_{avg} = 1.89 \times 10^{-2} \, \frac{\text{mm}}{\text{mm}}$ while the slope of the second part is small.
The average strain is larger than the strain measured by the strain gauges or calculated

by the numerical analysis, because the average strain is measured from grip to grip and the test fixture slipped in the grip. Consequently, the average strain is higher than the actual strain measured by the SGs.
Moreover, the average strain line indicates yielding of the material. However, the aluminum cylinder did not yield. The deviation from the other measured values occurred because of the slipping of the test fixture.
A plastic deformation did not occur because $\sigma_{max} \leq \sigma_y$. Thus, the specimen shrinks back to its original size after removing the load.

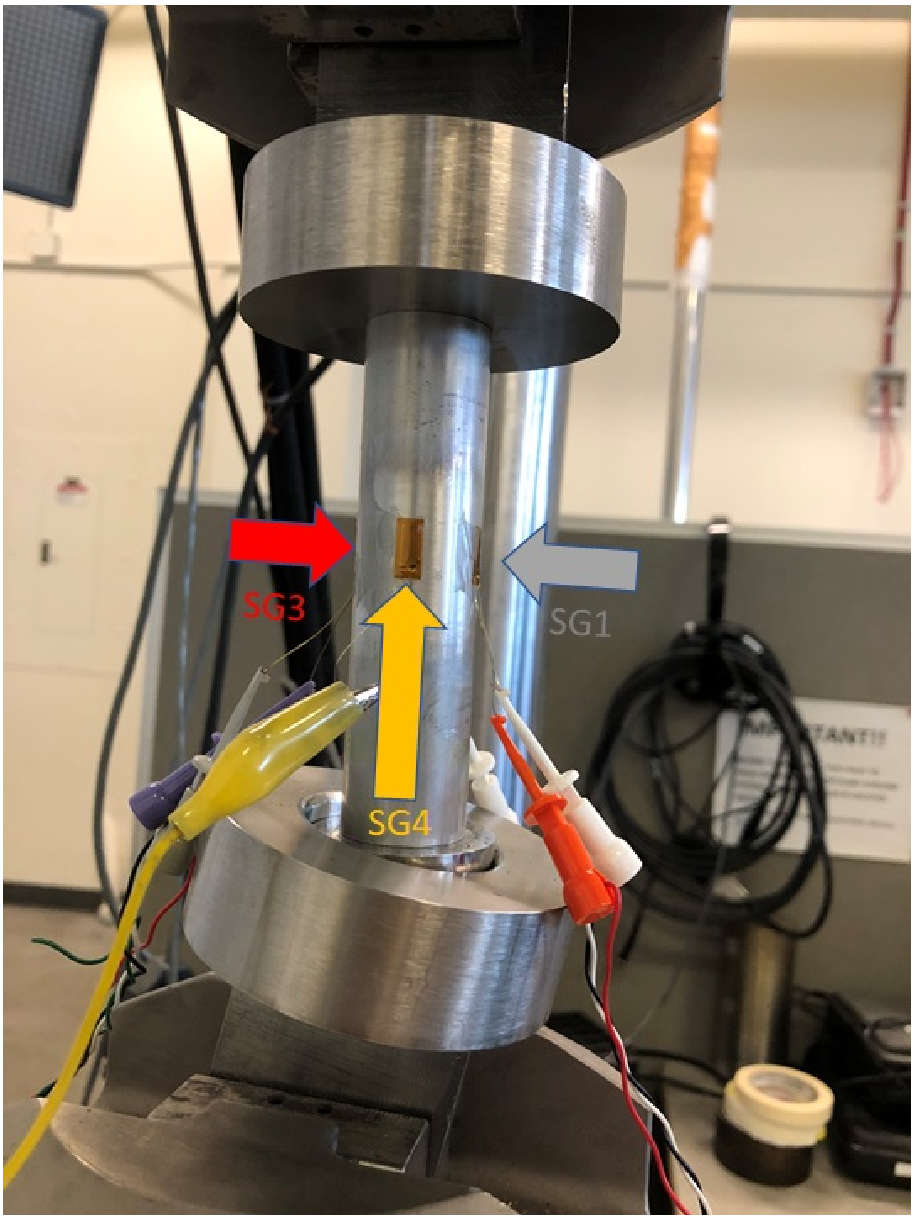

Figure 6.5.: Compression test setup at 5° offset.

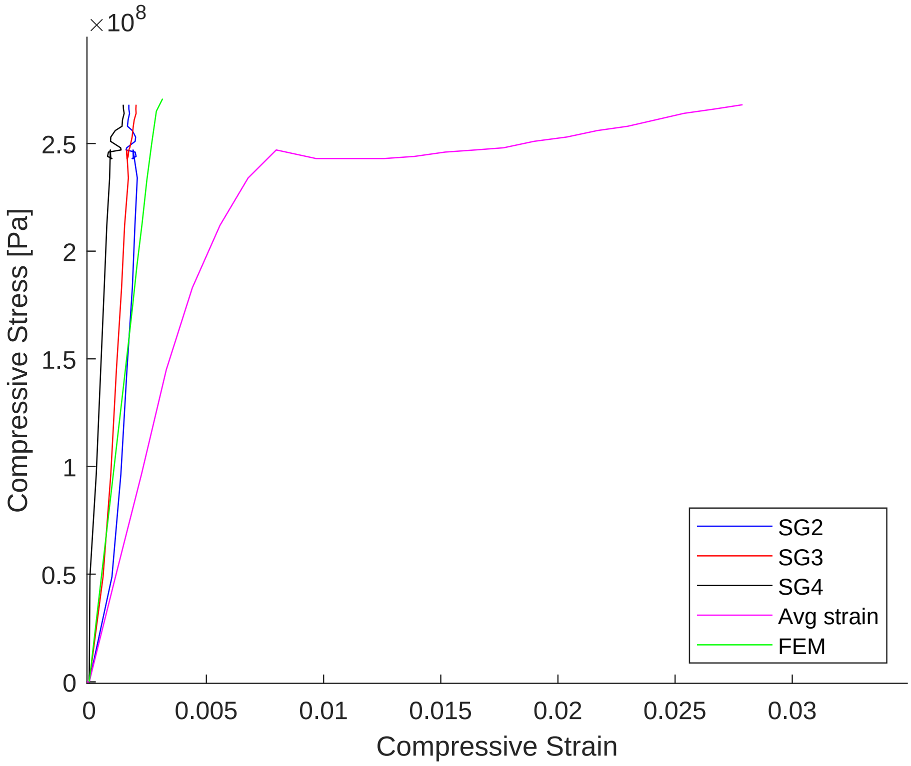

Figure 6.6.: Stress/strain graph 5° offset, loading 9,436.0 N.

Table 6.3.: Experimental determined stress and strain of the aluminum cylinder 5° offset, 9,380.0 N.

F [N]	σ [MPa]	SG2 $[\frac{mm}{mm}]$	SG3 $[\frac{mm}{mm}]$	SG4 $[\frac{mm}{mm}]$	ϵ_{avg} $[\frac{mm}{mm}]$
0	0	0	0	0	0
363	10.4	1.09×10^{-3}	4.02×10^{-3}	1.71×10^{-3}	1.22×10^{-3}
171	48.8	2.06×10^{-3}	4.61×10^{-3}	1.74×10^{-3}	2.34×10^{-3}
3370	96.4	2.44×10^{-3}	4.94×10^{-3}	2.01×10^{-3}	3.45×10^{-3}
5070	14.5	2.70×10^{-3}	5.18×10^{-3}	2.20×10^{-3}	4.51×10^{-3}
6400	183	2.96×10^{-3}	5.40×10^{-3}	2.35×10^{-3}	5.62×10^{-3}
7420	212	3.04×10^{-3}	5.53×10^{-3}	2.46×10^{-3}	6.80×10^{-3}
8160	234	3.14×10^{-3}	5.69×10^{-3}	2.58×10^{-3}	8.00×10^{-3}
8620	247	2.96×10^{-3}	5.62×10^{-3}	2.61×10^{-3}	9.20×10^{-3}
8490	243	2.97×10^{-3}	5.63×10^{-3}	2.63×10^{-3}	1.09×10^{-2}
8490	243	2.96×10^{-3}	5.64×10^{-3}	2.63×10^{-3}	1.24×10^{-2}
8490	243	2.92×10^{-3}	5.65×10^{-3}	2.68×10^{-3}	1.38×10^{-2}
8520	244	3.09×10^{-3}	5.68×10^{-3}	2.49×10^{-3}	1.51×10^{-2}
8590	246	3.05×10^{-3}	5.70×10^{-3}	2.53×10^{-3}	1.64×10^{-2}
8640	247	2.66×10^{-3}	5.71×10^{-3}	3.07×10^{-3}	1.77×10^{-2}
8660	248	2.69×10^{-3}	5.75×10^{-3}	3.05×10^{-3}	1.89×10^{-2}
8760	251	3.05×10^{-3}	5.81×10^{-3}	2.62×10^{-3}	2.02×10^{-2}
8850	253	3.07×10^{-3}	5.85×10^{-3}	2.63×10^{-3}	2.16×10^{-2}
8950	256	2.93×10^{-3}	5.88×10^{-3}	2.82×10^{-3}	2.29×10^{-2}
9030	258	2.72×10^{-3}	5.90×10^{-3}	3.11×10^{-3}	2.42×10^{-2}
9110	261	2.75×10^{-3}	5.94×10^{-3}	3.13×10^{-3}	2.54×10^{-2}
9210	264	2.81×10^{-3}	6.02×10^{-3}	3.20×10^{-3}	2.66×10^{-2}
9310	266	2.78×10^{-3}	6.01×10^{-3}	3.17×10^{-3}	2.79×10^{-2}
9380	268	2.78×10^{-3}	6.02×10^{-3}	3.16×10^{-3}	2.91×10^{-2}

Table 6.4.: Numerical determined stress and strain of the aluminum cylinder 5° offset, 9,436.0 N.

F [N]	σ_v [MPa]	ϵ_v [$\frac{mm}{mm}$]
646.80	19.197	2.06040×10^{-4}
1294.75	38.428	4.11920×10^{-4}
1943.87	57.694	6.17650×10^{-4}
2594.24	76.997	8.23401×10^{-4}
3245.96	96.34	1.02870×10^{-3}
3898.93	115.72	1.23401×10^{-3}
4553.58	135.15	1.43920×10^{-3}
5209.58	154.62	1.64430×10^{-3}
8567.26	174.14	1.84920×10^{-3}
7188.02	193.71	2.05410×10^{-3}
7433.85	213.34	2.25890×10^{-3}
7851.10	233.02	2.46360×10^{-3}
8504.39	252.41	2.66790×10^{-3}
9021.92	267.77	2.87330×10^{-3}
9436.0	280.06	3.42410×10^{-3}

6.3. Result of Compression Test Using an Offset of 10°

In Figure 6.7, the test fixture clamped in the two hydraulic grips of the compression testing machine is shown. The measured values of each strain gauge are plotted in relation to the stress in Figure 6.8. This figure also plots the average strain and the numerical stress/strain curve for comparison.
The values of the applied force, the determined stress, the strain gauges, and the average strain can be found in table 6.5. The calculated stress and strain data of the numerical analysis can be found in table 6.6.
The specimen was subjected to a compression load of 5,390.0 N. However, the test fixture started to slip at a force of approx. 5,230.0 N and a stress of $\sigma = 150$ MPa. A maximum stress of $\sigma_{max} = 154$ MPa and and an average strain of $\epsilon_{avg} = 1.54 \times 10^{-2} \, \frac{\mathrm{mm}}{\mathrm{mm}}$ occurred when the force was applied. At σ_{max}, the maximum measured strain occurred in SG2 with a value of $\epsilon = 2.97 \times 10^{-3} \, \frac{\mathrm{mm}}{\mathrm{mm}}$, while the minimum measured strain occurred in SG4 with a value of $\epsilon = 2.54 \times 10^{-3} \, \frac{\mathrm{mm}}{\mathrm{mm}}$.
In Figure 6.8, it is possible to see that all lines, except the average strain line, rise linearly. The FEM line rises until a stress of $\sigma = 154.34$ MPa and a strain of $\epsilon = 1.54 \times 10^{-2} \, \frac{\mathrm{mm}}{\mathrm{mm}}$ are reached. The SG lines climb almost parallel to the ordinate. Moreover, the SG lines are parallel to each other. The average strain line can be divided into two parts. The first part rises to $\sigma = 134$ MPa and $\epsilon = 8.64 \times 10^{-3} \, \frac{\mathrm{mm}}{\mathrm{mm}}$. The slope of the second part is smaller and almost parallel to the abscissa until $\epsilon = 1.54 \times 10^{-2} \, \frac{\mathrm{mm}}{\mathrm{mm}}$ is reached.

The average strain is larger than the strain measured by the strain gauges or calculated by the numerical analysis. Moreover, the average strain line indicates yielding of the material. However, the aluminum cylinder did not yield. The deviation from the measured and numerical calculated values occurred because of slipping of the test fixture.

A plastic deformation did not occur because $\sigma_{max} \leq \sigma_y$. Thus, the specimen shrinks back to its original size after removing the load.

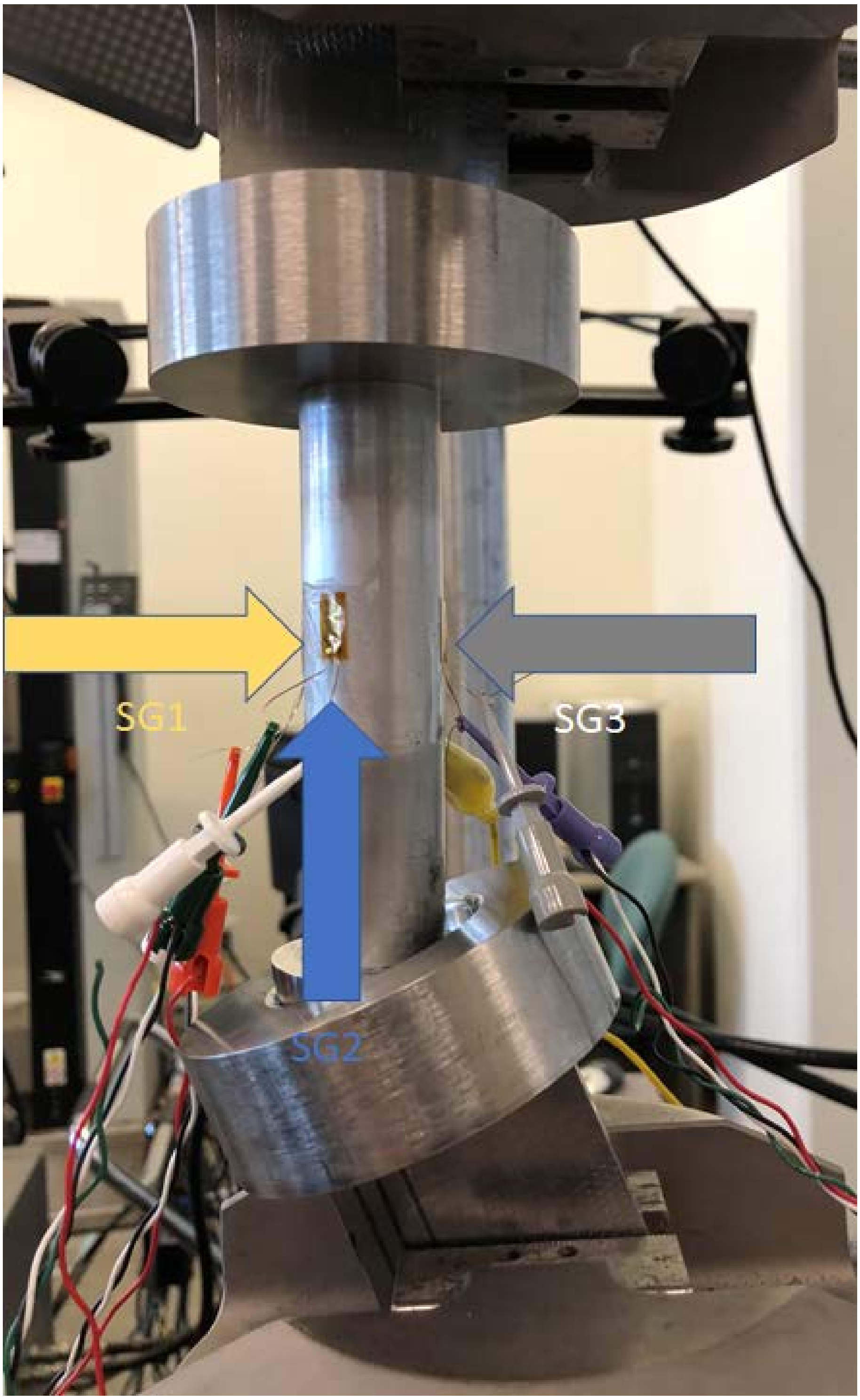

Figure 6.7.: Compression test setup at 10° offset.

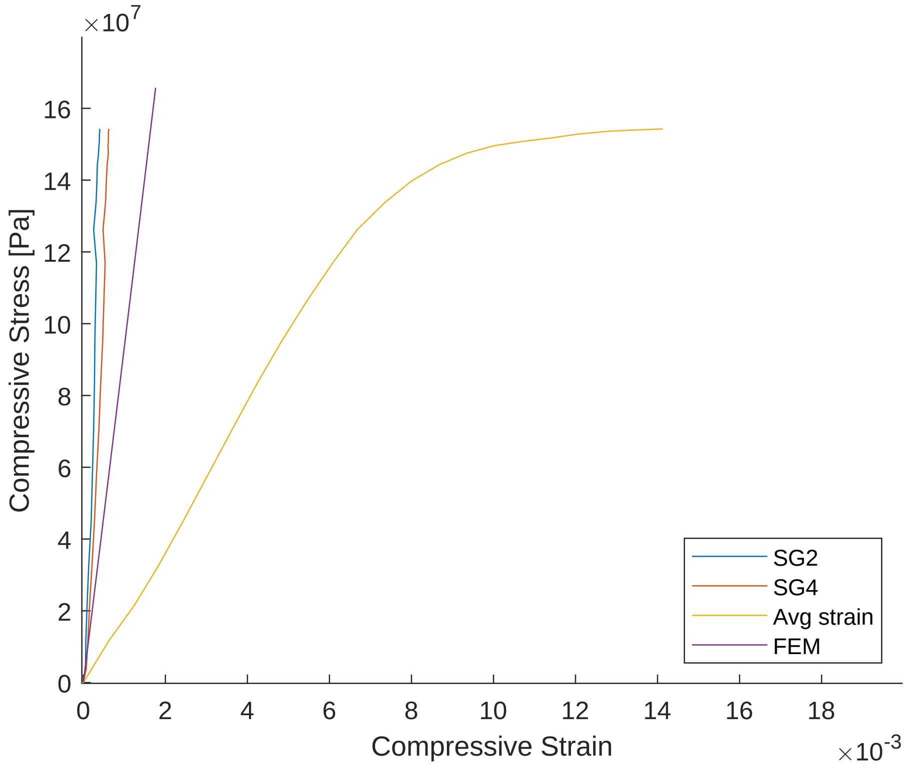

Figure 6.8.: Stress/strain graph 10° offset, loading 5,394.50 N.

Table 6.5.: Experimental determined stress and strain of the aluminum cylinder 10° offset, 5,390.0 N.

F [N]	σ [MPa]	SG2 $[\frac{mm}{mm}]$	SG4 $[\frac{mm}{mm}]$	ϵ_{avg} $[\frac{mm}{mm}]$
0	0	0	0	0
0.08	0.0228	2.600×10^{-3}	1.920×10^{-3}	1.710×10^{-4}
13.50	0.386	2.580×10^{-3}	1.990×10^{-3}	7.120×10^{-4}
131.20	3.753	2.630×10^{-3}	2.030×10^{-3}	1.310×10^{-3}
412.60	11.805	2.640×10^{-3}	2.070×10^{-3}	1.900×10^{-3}
750.33	21.470	2.670×10^{-3}	2.130×10^{-3}	2.520×10^{-3}
1138.69	32.582	2.710×10^{-3}	2.190×10^{-3}	3.110×10^{-3}
1569.40	44.906	2.770×10^{-3}	2.224×10^{-3}	3.710×10^{-3}
2025.77	57.965	2.800×10^{-3}	2.230×10^{-3}	4.300×10^{-3}
2473.71	70.782	2.830×10^{-3}	2.300×10^{-3}	4.910×10^{-3}
2901.38	83.019	2.850×10^{-3}	2.340×10^{-3}	5.500×10^{-3}
3321.65	95.045	2.860×10^{-3}	2.390×10^{-3}	6.100×10^{-3}
3716.48	106.342	2.880×10^{-3}	2.420×10^{-3}	6.710×10^{-3}
4080.84	116.768	2.900×10^{-3}	2.450×10^{-3}	7.410×10^{-3}
4411.68	126.235	2.830×10^{-3}	2.400×10^{-3}	8.010×10^{-3}
4677.99	133.855	2.890×10^{-3}	2.460×10^{-3}	8.610×10^{-3}
4883.62	139.739	2.910×10^{-3}	2.480×10^{-3}	9.310×10^{-3}
5041.66	144.261	2.920×10^{-3}	2.500×10^{-3}	9.910×10^{-3}
5153.97	147.474	2.950×10^{-3}	2.530×10^{-3}	1.060×10^{-2}
5228.28	149.601	2.960×10^{-3}	2.520×10^{-3}	1.130×10^{-2}
5270.05	150.796	2.970×10^{-3}	2.530×10^{-3}	1.200×10^{-2}
5302.00	151.710	2.970×10^{-3}	2.530×10^{-3}	1.217×10^{-2}
5341.39	152.838	2.970×10^{-3}	2.530×10^{-3}	1.330×10^{-2}
5367.23	153.576	2.980×10^{-3}	2.530×10^{-3}	1.410×10^{-2}
5381.19	153.972	2.980×10^{-3}	2.540×10^{-3}	1.470×10^{-2}
5390.00	154.265	2.970×10^{-3}	2.540×10^{-3}	1.544×10^{-2}

Table 6.6.: Numerical determined stress and strain of the aluminum cylinder 10° offset, 5,391.0 N.

F [N]	σ_v [MPa]	ϵ_v [$\frac{mm}{mm}$]
356.80	10.97	1.1775×10^{-4}
713.60	21.94	2.3545×10^{-4}
1071.04	32.93	3.5309×10^{-4}
1428.82	43.93	4.7069×10^{-4}
1786.92	54.94	5.8823×10^{-4}
2145.34	65.96	7.0573×10^{-3}
2504.42	77.00	8.2318×10^{-4}
2863.50	88.04	9.4059×10^{-4}
3223.22	99.10	1.0586×10^{-3}
3583.30	110.17	1.1753×10^{-3}
3943.97	121.26	1.2925×10^{-3}
4304.99	132.36	1.4098×10^{-3}
4666.35	143.47	1.5270×10^{-3}
5028.35	154.60	1.6442×10^{-3}
5391.0	165.75	1.7613×10^{-3}

6.4. Result of Compression Test Using an Offset of 15°

In Figure 6.7, the test fixture clamped in the two hydraulic grips of the compression testing machine is shown. The average strain/stress and the numerical stress/strain curves are plotted in Figure 6.8.
The values of the applied force, the determined stress, and the average strain can be found in table 6.7. The calculated stress and strain data of the numerical analysis can be found in table 6.8.
The specimen was subjected to a compression load of 1,960.0 N. However, the test fixture started to slip at a force of approx. 1000 N. A maximum stress of $\sigma_{max} = 56$ MPa and an average strain of $\epsilon_{avg} = 2.91 \times 10^{-2} \frac{\text{mm}}{\text{mm}}$ occurred when the force was applied.
In Figure 6.10, it is possible to see that the both lines rise linearly. The FEM line rises until a stress of $\sigma = 58.20$ MPa and a strain of $\epsilon = 1.509760 \times 10^{-3} \frac{\text{mm}}{\text{mm}}$ are reached. The average strain line can be divided into two parts. The first part rises to $\sigma = 51.0$ MPa and $\epsilon = 1.85 \times 10^{-2} \frac{\text{mm}}{\text{mm}}$. The slope of the second part is smaller and almost parallel to the abscissa until $\epsilon = 2.91 \times 10^{-2} \frac{\text{mm}}{\text{mm}}$ is reached.
The average strain values deviate from the numerical calculated values tremendously. Moreover, the average strain line indicates yielding of the material. However, the aluminum cylinder did not yield. The deviation from the numerical calculated values occurred because of slipping of the test fixture.
A plastic deformation did not occur because $\sigma_{max} \leq \sigma_y$. Thus, the specimen shrinks back to its original size after removing the load.

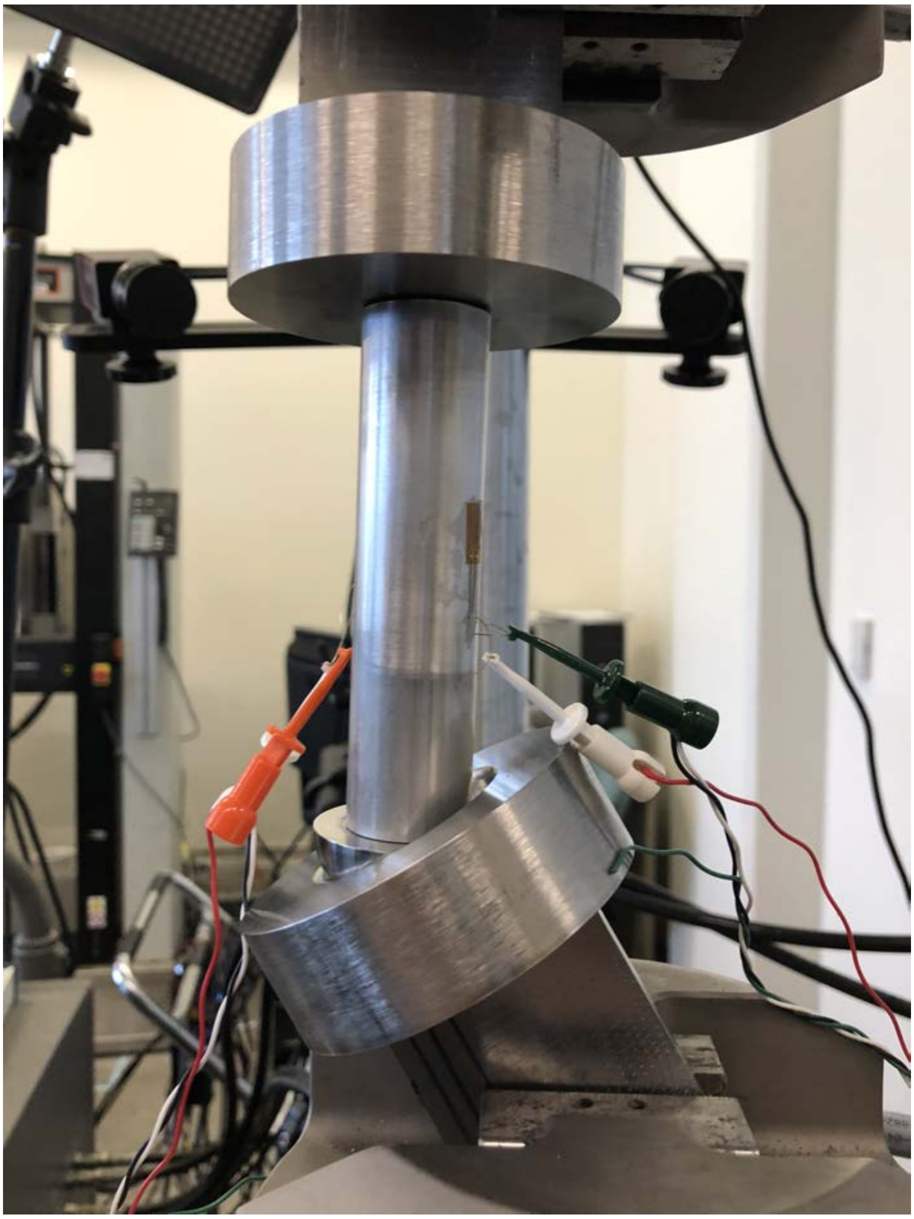

Figure 6.9.: Compression test setup at 15° offset.

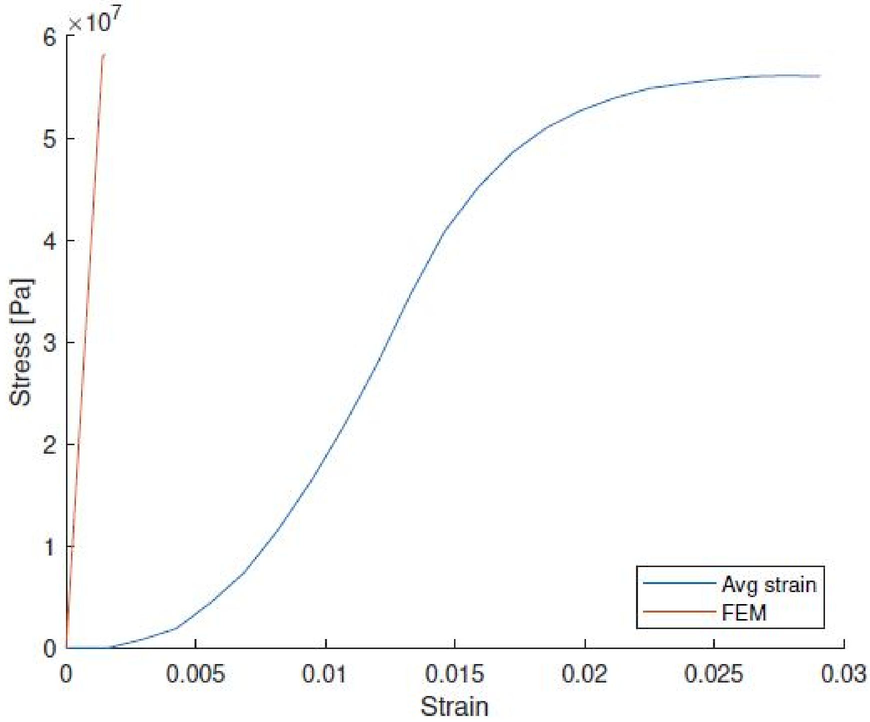

Figure 6.10.: Stress/strain graph 15° offset, loading 1,960.0 N.

Table 6.7.: Experimental determined stress and strain of the aluminum cylinder 15° offset, 1,960.0 N.

F [N]	σ [MPa]	ϵ_{avg} $[\frac{mm}{mm}]$
0	0	0
0.77	0.022	3.42×10^{-4}
1.46	0.0419	1.66×10^{-3}
30.2	0.863	2.96×10^{-3}
67.0	1.92	4.25×10^{-3}
154	4.42	5.57×10^{-3}
258	7.38	6.87×10^{-3}
404	11.50	8.17×10^{-3}
571	16.40	9.45×10^{-3}
765	21.90	1.07×10^{-2}
975	27.90	1.20×10^{-2}
1220	34.80	1.33×10^{-2}
1430	40.80	1.46×10^{-2}
158	45.20	1.59×10^{-2}
1700	48.60	1.72×10^{-2}
1780	51.0	1.85×10^{-2}
1840	52.70	1.99×10^{-2}
1890	54.0	2.12×10^{-2}
1920	54.90	2.25×10^{-2}
1930	55.30	2.38×10^{-2}
1950	55.70	2.51×10^{-2}
1960	56.0	2.65×10^{-2}
1960	56.1	2.78×10^{-2}
1960	56.0	2.91×10^{-2}

Table 6.8.: Numerical determined stress and strain of the aluminum cylinder 15° offset, 2,032.0 N.

F [N]	σ_v [MPa]	ϵ_v [$\frac{mm}{mm}$]
135.10	4.13	4.4437×10^{-5}
270.12	8.26	8.8867×10^{-5}
405.50	12.40	1.3329×10^{-4}
540.73	16.54	1.7770×10^{-4}
675.95	20.67	2.2211×10^{-4}
811.33	24.81	2.6651×10^{-4}
946.72	28.95	3.1091×10^{-4}
1082.43	33.10	3.5529×10^{-4}
1217.82	37.24	3.9967×10^{-4}
1353.21	41.38	4.4405×10^{-4}
1488.92	45.53	4.8841×10^{-4}
1624.63	49.68	5.3277×10^{-4}
1760.35	53.83	5.7712×10^{-4}
1896.06	57.98	6.2147×10^{-4}
2032.0	62.14	6.6580×10^{-4}

7. Results of the Compression Testing of the Composite Cylinders

In this chapter, the different experimental tests conducted by varying the loading angle are described. After that, the results of the tests are discussed. The specimens were manufactured by using two layers and a winding angle of 45°.

The bottom part of the test fixture has to be clamped with an offset in the lower hydraulic grip to vary the loading angle. However, the bottom part started to slip in the grip when clamped with an offset in the grip and force was applied. Therefore, the applicable force varies for each loading angle.
The experimental compression tests of the composite cylinders are conducted to compare the numerical results (see Chapter 10) with the experimental results and to verify the numerical results. The FEM strain was computed along the longitudinal direction of the front side of the cylinder. In Figure 7.1, the previously described location is shown by the green line.
However, it is to be expected that the compression load causes a certain stress level in the cylinders at which microcracking might occur and both fibre and resin might start to debond. However, the results will vary because of the above described issue regarding the grip and the different loading angle.
In Figure 7.2, the different stress/strain curves for each loading angle are shown.

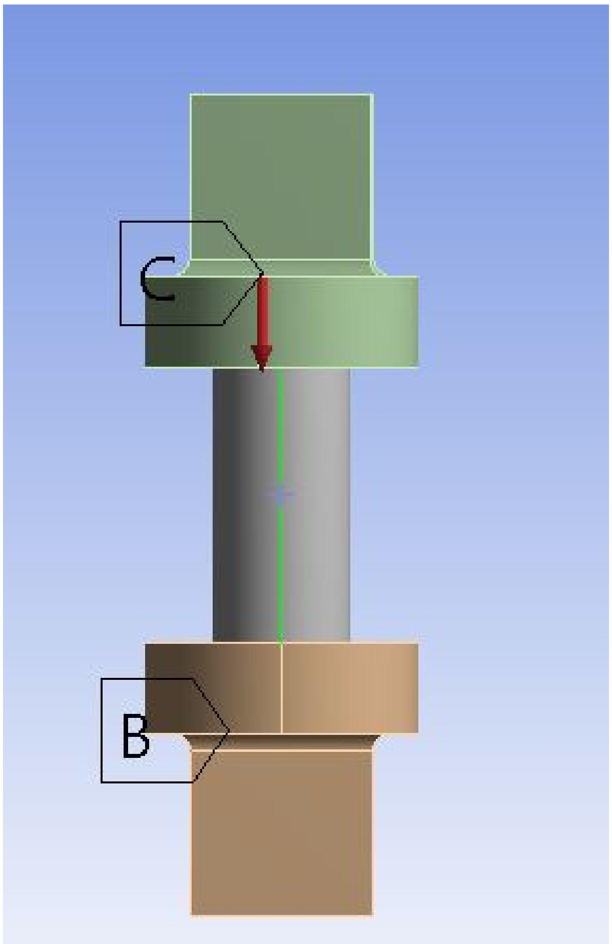

Figure 7.1.: Location of the computational determined FEM strain.

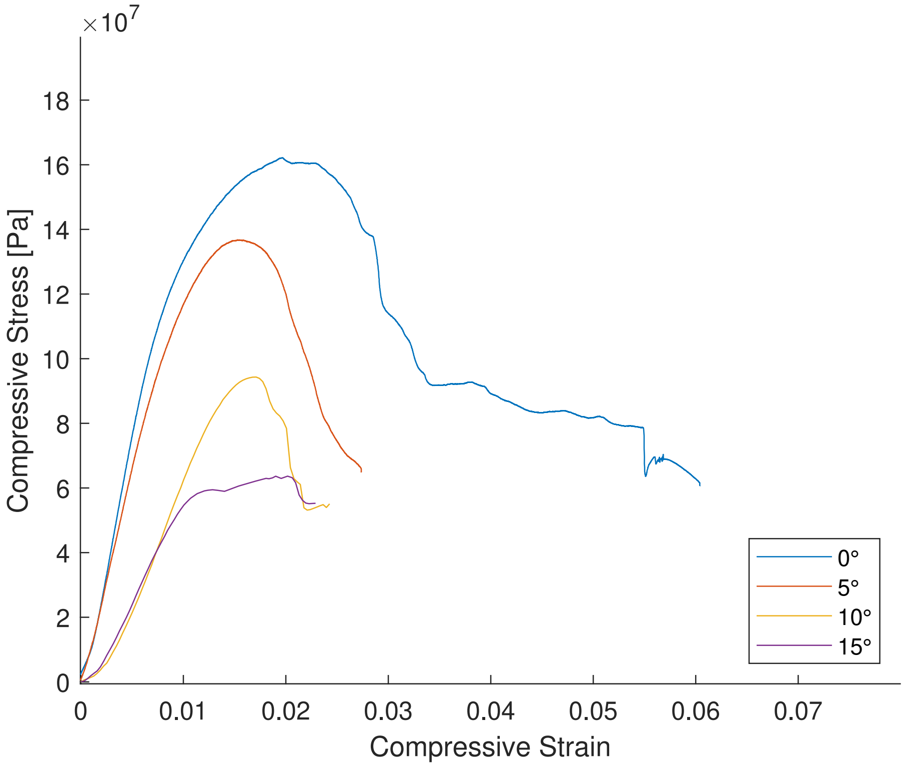

Figure 7.2.: Comparison of the different stress/strain graphs, different loadings.

7.1. Result of Compression Test Using an Offset of 0°

In Figure 7.3, the test fixture clamped in the two hydraulic grips of the compression testing machine is shown. The stress/strain graph and the numerical stress/strain curve as comparison are shown in Figure 7.4.

The values of the applied force, the determined stress and strain values can be found in table 7.1. The calculated stress and strain data of the numerical analysis can be found in table 7.2 to facilitate the comparison of the results obtained by the experimental test and the numerical analysis.

It was not possible to apply the desired force of 10,000.0 N because debonding and fibre breakage occurred before reaching the desired force. Therefore, it was only possible to apply a force of 5,674.86 N, which caused a maximum stress of $\sigma_{max} = 162.14$ MPa and a strain of $\epsilon = 2.0520 \times 10^{-2} \frac{\text{mm}}{\text{mm}}$ to the specimen. However, the maximum strain $\epsilon_{max} = 6.1228 \times 10^{-2} \frac{\text{mm}}{\text{mm}}$ was reached after the maximum possible force was applied and the force was decreased to an unloaded condition. ϵ_{max} was caused by a stress of $\sigma = 60.60$ MPa.

The average stress/strain curve can be divided into four parts. The first part of the stress/strain curve rises parabolically until σ_{max} is reached. At the inflection point, the curve falls almost straight, except for some outliers, until a stress of approx. $\sigma = 90$

MPa is reached. The slope of the third part is flatter than the slope of the second part and falls until $\sigma = 83.40$ MPa is reached. The curve of the fourth part includes the perpendicular drop from $\sigma = 83.40$ MPa to $\sigma = 65$ MPa and falls until $\sigma = 60.60$ MPa is reached.
The FEM line rises linearly and the slope of the FEM line is lower than the slope of the average strain line because the Young's modulus was only assumed and is lower than the actual Young's modulus. The average strain line differs from the SG line because the strain was calculated from the measured displacement of the compression testing machine. This displacement is measured from grip to grip. Consequently, the average strain is higher than the actual strain measured by the SGs. Moreover, the line remains below the average strain line. However, the maximum stress and strain value of the line is reached directly below the inflection point of the average strain curve.
According to the shape of the average stress/strain curve, microcracking takes place at a stress of approx. $\sigma = 130$ MPa and the first fibre/resin debonding is caused by a strain of approx. $\epsilon = 1.20 \times 10^{-2} \frac{\text{mm}}{\text{mm}}$. After the microcracking is initiated and σ_{max} is reached, fibre breakage of some fibres of the bottom face of the cylinder occurs due to the debonding of the matrix and reinforcement. The damage of the cylinder can be seen in Figure 7.5.

Figure 7.3.: Compression test setup at 0° offset.

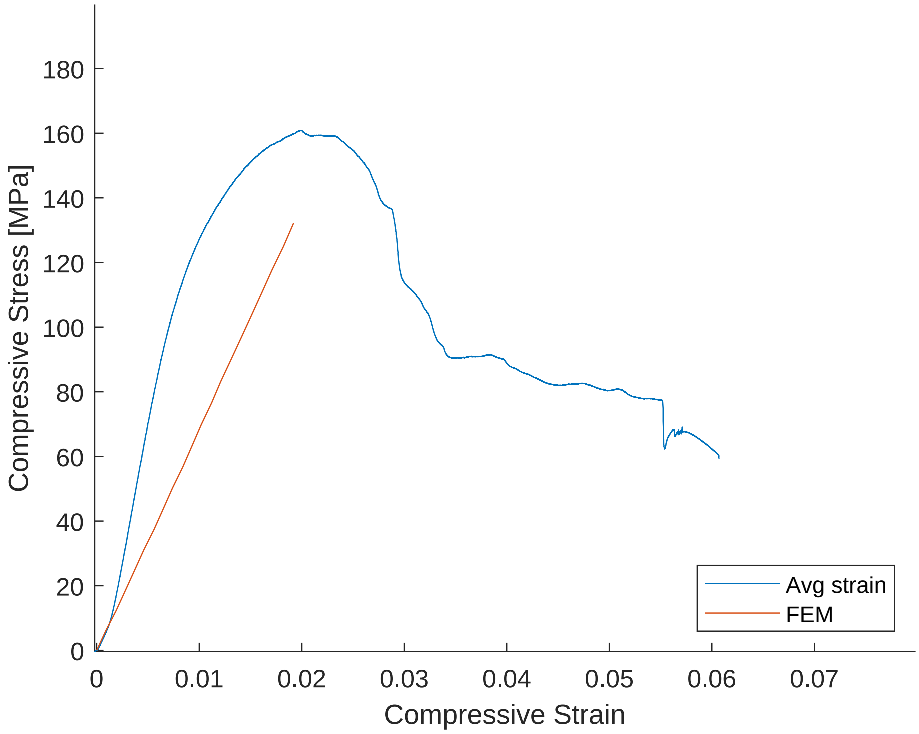

Figure 7.4.: Stress/strain graph 0° offset, loading 5,674.86 N.

Figure 7.5.: Damage of the composite cylinder 0° offset, loading 5,674.86 N.

Table 7.1.: Experimental determined stress and strain of the composite cylinder 0° offset, 5,674.86 N.

F [N]	σ [MPa]	ϵ_{avg} [$\frac{mm}{mm}$]
1327.77	37.94	3.6130×10^{-3}
2089.50	59.70	4.8530×10^{-3}
2500.96	71.46	5.5375×10^{-3}
3354.07	95.83	7.1687×10^{-3}
3550.27	101.44	7.5992×10^{-3}
3736.32	106.75	8.0478×10^{-2}
4552.83	130.10	1.0790×10^{-2}
5070.32	144.90	1.3590×10^{-2}
5368.68	153.40	1.5890×10^{-2}
5547.24	158.50	1.8120×10^{-2}
5674.86	162.14	2.0520×10^{-2}
5637.00	161.10	2.0962×10^{-2}
4531.65	129.48	2.9789×10^{-2}
3939.71	112.56	3.1338×10^{-2}
2919.47	83.40	4.8557×10^{-2}
2120.57	60.60	6.1228×10^{-2}

Table 7.2.: Numerical determined stress and strain of the composite cylinder 0° offset, 5,674.86 N.

F [N]	σ_{III} [MPa]	ϵ_{III} $[\frac{mm}{mm}]$
263.91	6.1479	9.020×10^{-4}
529.37	12.3320	$1.91\ 0 \times 10^{-3}$
796.46	18.5540	2.820×10^{-3}
1065.17	24.8140	3.730×10^{-3}
1335.70	31.1160	4.620×10^{-3}
1607.98	37.4590	5.610×10^{-3}
1882.20	43.8470	6.540×10^{-3}
2158.40	50.2810	7.410×10^{-3}
2436.63	56.7630	8.420×10^{-3}
2717.11	63.2970	9.310×10^{-3}
2999.77	69.8820	1.020×10^{-2}
3284.90	76.5240	1.120×10^{-2}
3572.46	83.2230	1.210×10^{-2}
3862.64	89.9830	1.310×10^{-2}
4155.90	96.8140	1.410×10^{-2}
4451.89	103.7100	1.510×10^{-2}
4751.51	110.6900	1.610×10^{-2}
5054.60	117.7500	1.710×10^{-2}
5323.60	124.9200	1.820×10^{-2}
5674.86	132.2200	1.920×10^{-2}

7.2. Result of Compression Test Using an Offset of 5°

The stress/strain graph and the numerical stress/strain curve as comparison are shown in Figure 7.6. This figure also plots the numerical stress/strain curve for comparison.
The values of the applied force, the determined stress and strain values can be found in table 7.3. The calculated stress and strain data of the numerical analysis can be found in table 7.4 to facilitate the comparison of the results obtained by the experimental test and the numerical analysis.
The bottom part of the test fixture tilted slightly in the hydraulic grip due to the loading angle. Therefore it was only possible to apply a force of 4,786.8 N, which caused a maximum stress of $\sigma_{max} = 136.77$ MPa and a strain of $\epsilon = 1.58147 \times 10^{-2}\ \frac{\text{mm}}{\text{mm}}$ to the specimen. However, the maximum strain $\epsilon_{max} = 2.78832 \times 10^{-2}\ \frac{\text{mm}}{\text{mm}}$ was reached after the maximum possible force was applied and the force was decreased to an unloaded condition. ϵ_{max} was caused by a stress of $\sigma = 64.81$ MPa.
The stress/strain curve can be divided into three parts. The first part of the stress/strain curve rises parabolic until σ_{max} and a strain of $\epsilon = 1.58147 \times 10^{-2}\ \frac{\text{mm}}{\text{mm}}$ is reached at the inflection point. Then the second part of the curve falls until a stress of $\sigma = 83.40$ MPa

and a strain of $\epsilon = 2.40395 \times 10^{-2}\,\frac{\text{mm}}{\text{mm}}$ is reached. The third part of the curve falls flatter than the second part until a stress of $\sigma = 64.81$ MPa is reached.
The FEM line rises linearly and has a flatter slope gradient, compared to the average strain line. Moreover, the line is below the average strain line until the intersection of both graphs at a stress of $\sigma = 64.81$ MPa and a strain of $\epsilon = 2.11096 \times 10^{-2}\,\frac{\text{mm}}{\text{mm}}$. However, the maximum stress and strain value of the line is reached, directly below the inflection point of the average strain curve.
According to the shape of the average stress/strain curve, microcracking takes place at a stress of approx. $\sigma = 82.99$ MPa and the first fibre/resin debonding is caused by a strain of $\epsilon = 1.28741 \times 10^{-2}\,\frac{\text{mm}}{\text{mm}}$. After the microcracking is initiated and the maximum stress level is reached, fibre breakage of some fibres of the bottom part of the cylinder occur due to the debonding of the matrix and reinforcement. Consequently, less stress is required to cause a larger strain. In Figure 7.7, the damaged cylinder on the right is compared to the unloaded cylinder on the left.

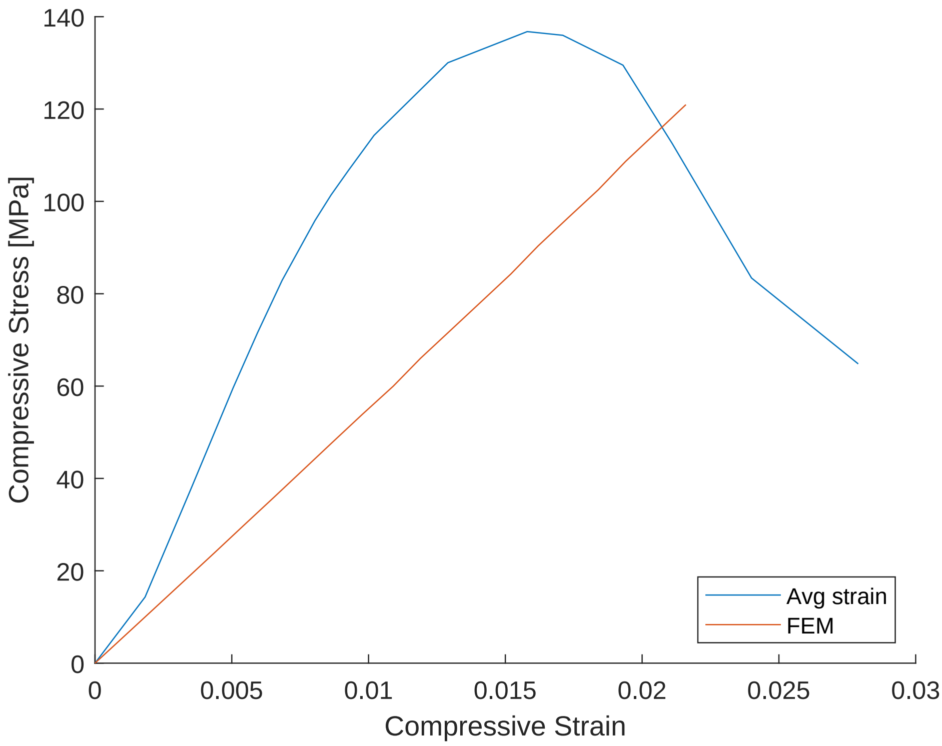

Figure 7.6.: Stress/strain graph 5° offset, loading 4,786.8 N.

Figure 7.7.: Damage of the composite cylinder 5° offset, loading 4,786.8 N.

Table 7.3.: Experimental determined stress and strain of the composite cylinder 5° offset, 4,786.8 N.

F [N]	σ [MPa]	ϵ_{avg} $[\frac{mm}{mm}]$
500.88	14.31	1.83356×10^{-3}
1327.03	37.92	3.51564×10^{-3}
2086.96	59.63	5.05487×10^{-3}
2503.78	71.54	5.93630×10^{-3}
2901.58	82.90	6.83570×10^{-3}
3354.45	95.84	8.04489×10^{-3}
3548.78	101.40	8.62540×10^{-3}
3736.75	106.76	9.26647×10^{-3}
4000.28	114.30	1.01922×10^{-2}
4550.89	130.03	1.28741×10^{-2}
4786.79	136.77	1.58147×10^{-2}
4758.86	135.97	1.70617×10^{-2}
4531.85	129.50	1.92948×10^{-2}
3938.54	112.53	2.11096×10^{-2}
2918.29	83.40	2.40395×10^{-2}
2268.18	64.81	2.78832×10^{-2}

Table 7.4.: Numerical determined stress and strain of the composite cylinder 5° offset.

F [N]	σ_{III} [MPa]	ϵ_{III} [$\frac{mm}{mm}$]
235.47	5.9498	1.09060×10^{-3}
471.36	11.91	2.18010×10^{-3}
707.63	17.88	3.26860×10^{-3}
944.30	23.86	4.35610×10^{-3}
1181.40	29.851	5.44250×10^{-3}
1418.94	35.853	6.52780×10^{-3}
1656.88	41.865	7.61190×10^{-3}
1895.30	47.889	8.69490×10^{-3}
2134.10	53.923	9.77670×10^{-3}
2373.33	59.968	1.08570×10^{-2}
2613.05	66.025	1.19370×10^{-2}
2853.20	72.093	1.30150×10^{-2}
3093.87	78.174	1.40910×10^{-2}
334.97	84.266	1.51660×10^{-2}
3576.43	90.367	1.6240×10^{-2}
3818.64	96.487	1.73120×10^{-2}
4057.80	102.53	1.83790×10^{-2}
4301.19	108.68	1.94470×10^{-2}
453.80	114.81	2.05120×10^{-2}
4786.80	120.95	2.15750×10^{-2}

7.3. Result of Compression Test Using an Offset of 10°

In Figure 7.8, the test fixture clamped in the two hydraulic grips of the compression testing machine is shown. The stress/strain graph and the numerical stress/strain curve as comparison are shown in Figure 7.9. The calculated stress and strain data of the numerical analysis can be found in table 7.6 to facilitate the comparison of the results obtained by the experimental test and the numerical analysis.
The bottom part of the test fixture tilted in the hydraulic grip due to the loading angle and the applied load. Therefore, it was only possible to apply a force of 3,302.90 N, which caused a maximum stress of $\sigma_{max} = 94.40$ MPa and a strain of $\epsilon = 1.69441 \times 10^{-2} \frac{\text{mm}}{\text{mm}}$ to the specimen. However, the maximum strain $\epsilon_{max} = 2.20410 \times 10^{-2} \frac{\text{mm}}{\text{mm}}$ was reached after the maximum possible force was applied and the force was decreased to an unloaded condition. ϵ_{max} was caused by a stress of $\sigma = 29.74$ MPa.
The average stress/strain curve can be divided into three different parts depending on their slope. The first part of the stress/strain curve rises parabolically until the inflection point is reached at σ_{max}. The second part falls almost straight until a stress of $\sigma = 53.16$ MPa is reached. After reaching a force of 1,327.54 N, the test fixture tilted in the grip, which also changed the longitudinal alignment of the cylinder due to the design of the

test fixture (Fig. 7.8). Because of the slip, the slope of the second part is flatter and the line falls in the third part of the stress/strain curve.
The FEM line rises linearly and has a flatter slope gradient, compared to the first part of the average strain line. The maximum point of the line is reached directly below the inflection point of the average strain curve.
The average stress/strain curve indicates that a damage (e.g., Fibre/Resin debonding) in the material occurred. Consequently, less stress is required to cause a larger strain. However, the cylinder did not fail during this test. In Figure 7.10, the loaded cylinder on the is right compared to the unloaded cylinder.

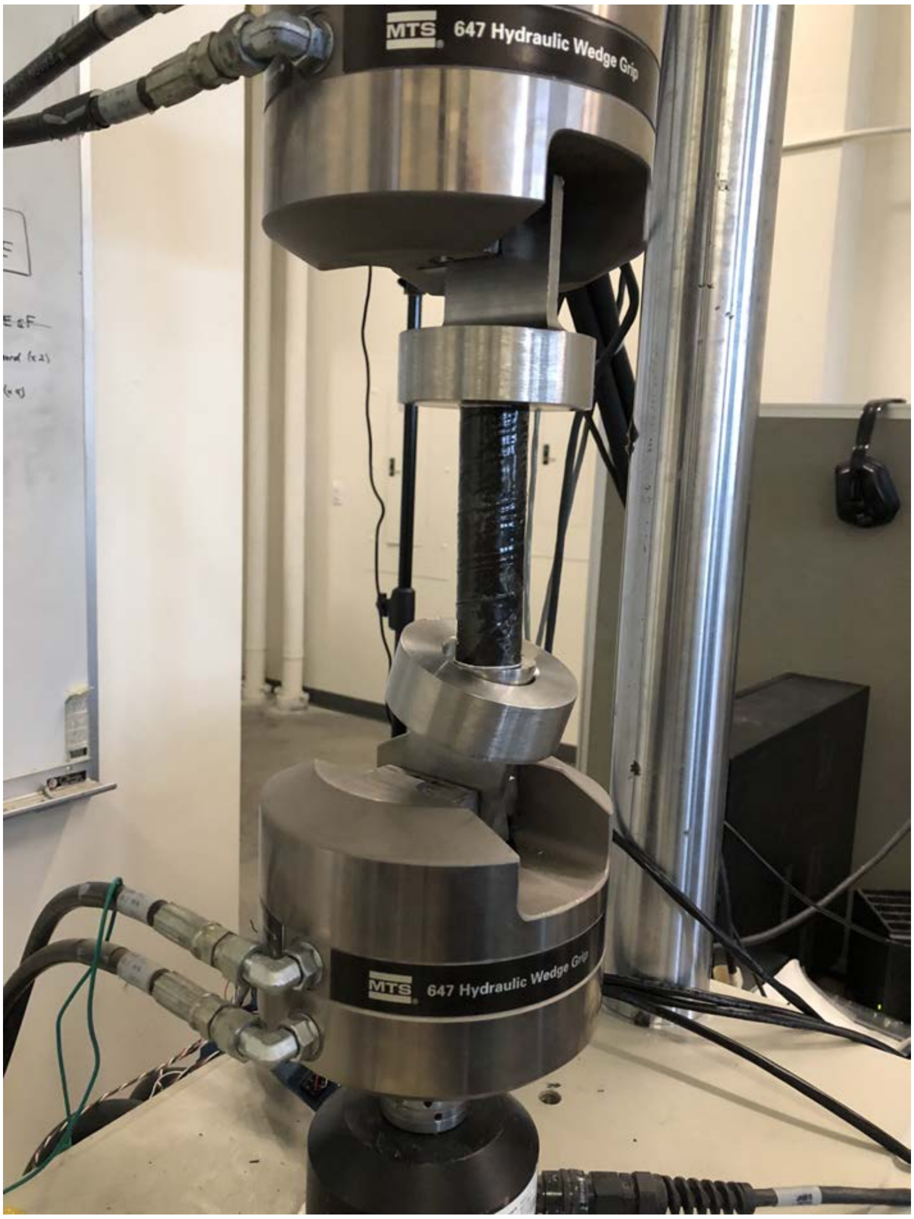

Figure 7.8.: Compression test setup at 10° offset.

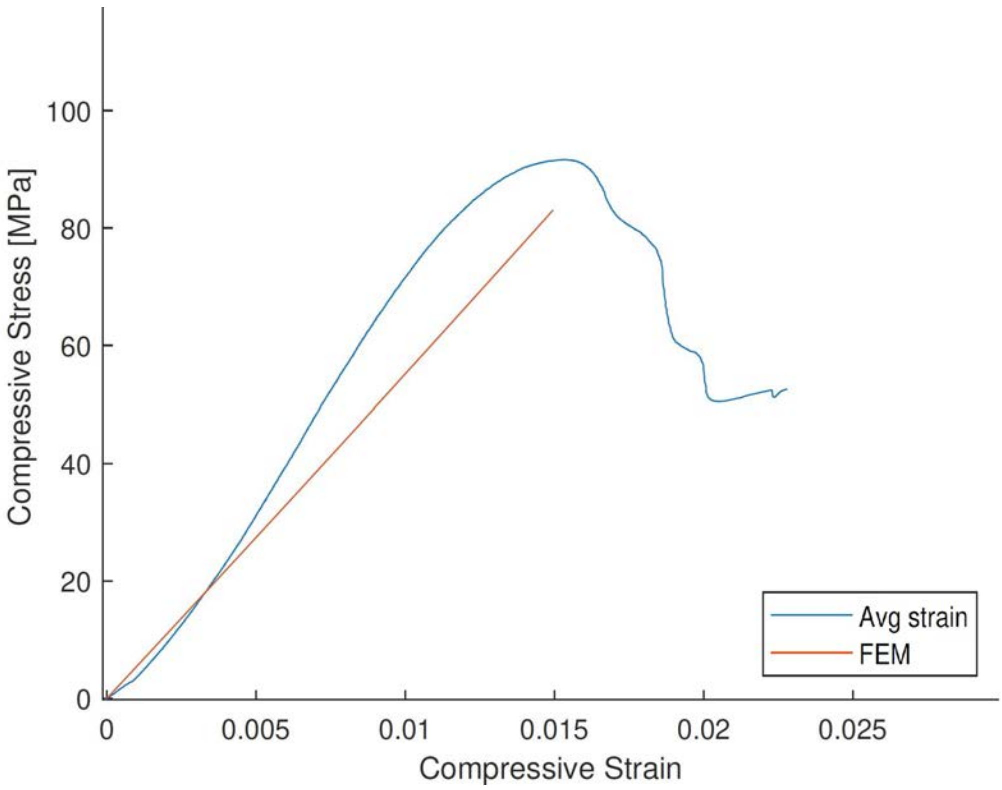

Figure 7.9.: Stress/strain graph 10° offset, loading 3,302.9 N.

Figure 7.10.: Loaded composite cylinder 10° offset, loading 3,302.9 N.

Table 7.5.: Experimental determined stress and strain of the composite cylinder 10° offset, 3,302.9 N.

F [N]	σ [MPa]	ϵ_{avg} $[\frac{mm}{mm}]$
499.89	14.28	3.96593×10^{-3}
1327.54	37.93	7.08909×10^{-3}
2086.57	59.62	9.67484×10^{-3}
2505.01	71.57	1.12225×10^{-2}
2900.46	82.87	1.29743×10^{-2}
3293.94	94.11	1.64103×10^{-2}
3302.90	94.40	1.69441×10^{-2}
2918.65	83.39	1.90250×10^{-2}
2264.10	64.69	2.05466×10^{-2}
1860.65	53.16	2.20410×10^{-2}

Table 7.6.: Numerical determined stress and strain of the composite cylinder 10° offset.

F [N]	σ_{III} [MPa]	ϵ_{III} $[\frac{mm}{mm}]$
163.23	4.1045	7.52490×10^{-4}
326.66	8.2138	1.50450×10^{-3}
490.27	12.328	2.25610×10^{-3}
654.10	16.447	3.00710×10^{-3}
818.10	20.571	3.75760×10^{-3}
982.30	24.70	4.50770×10^{-3}
1146.70	28.834	5.25720×10^{-3}
1311.27	32.972	6.00620×10^{-3}
1476.07	37.116	6.75470×10^{-3}
1641.11	41.266	7.50260×10^{-3}
1806.31	45.42	8.25011×10^{-3}
1971.71	49.579	8.99680×10^{-3}
2137.35	53.744	9.74310×10^{-3}
2303.19	57.914	1.04890×10^{-2}
2469.26	62.09	1.12340×10^{-2}
2635.54	66.271	1.19780×10^{-2}
2802.05	70.458	1.27220×10^{-2}
2968.76	74.65	1.34650×10^{-2}
3135.71	78.848	1.42080×10^{-2}
3302.90	83.052	1.49501×10^{-2}

7.4. Result of Compression Test Using an Offset of 15°

In Figure 7.11, the test fixture clamped in the two hydraulic grips of the compression testing machine is shown. The stress/strain graph is shown in Figure 7.12. The calculated stress and strain data of the numerical analysis can be found in table 7.8 to facilitate the comparison of the results obtained by the experimental test and the numerical analysis.

It was only possible to apply a force of 2,231.74 N, which caused a maximum stress of $\sigma_{max} = 63.76$ MPa and a strain of $\epsilon = 1.94594 \times 10^{-2} \frac{\text{mm}}{\text{mm}}$ to the specimen. However, the maximum strain $\epsilon_{max} = 2.30108 \times 10^{-2} \frac{\text{mm}}{\text{mm}}$ was reached after the maximum possible force was applied and the force was decreased to an unloaded condition. ϵ_{max} was caused by a stress of $\sigma = 54.83$ MPa.

The average strain curve can be divided into three parts. The first part of the curve rises with almost a constant slope gradient until the inflection point of $\sigma = 57.15$ MPa and a strain of $\epsilon = 1.082484 \times 10^{-2} \frac{\text{mm}}{\text{mm}}$ are reached. Then, the curve rises with a flatter slope gradient and almost straight until σ_{max} MPa is reached. The third part of the curve is falling until $\sigma = 54.83$ MPa is reached.

The FEM line rises linearly and is almost parallel to the first part of the average strain curve. Both graphs intersect each other at a stress of $\sigma = 53.13$ MPa and a strain of $\epsilon = 9.61350 \times 10^{-3} \frac{\text{mm}}{\text{mm}}$.

The curve indicates that a damage (e.g., Fibre/Resin debonding) in the material occurred. Consequently, less stress is required to cause a larger strain. However, the cylinder did not fail during this test. In Figure 7.13, the loaded cylinder on the right is compared to the unloaded cylinder.

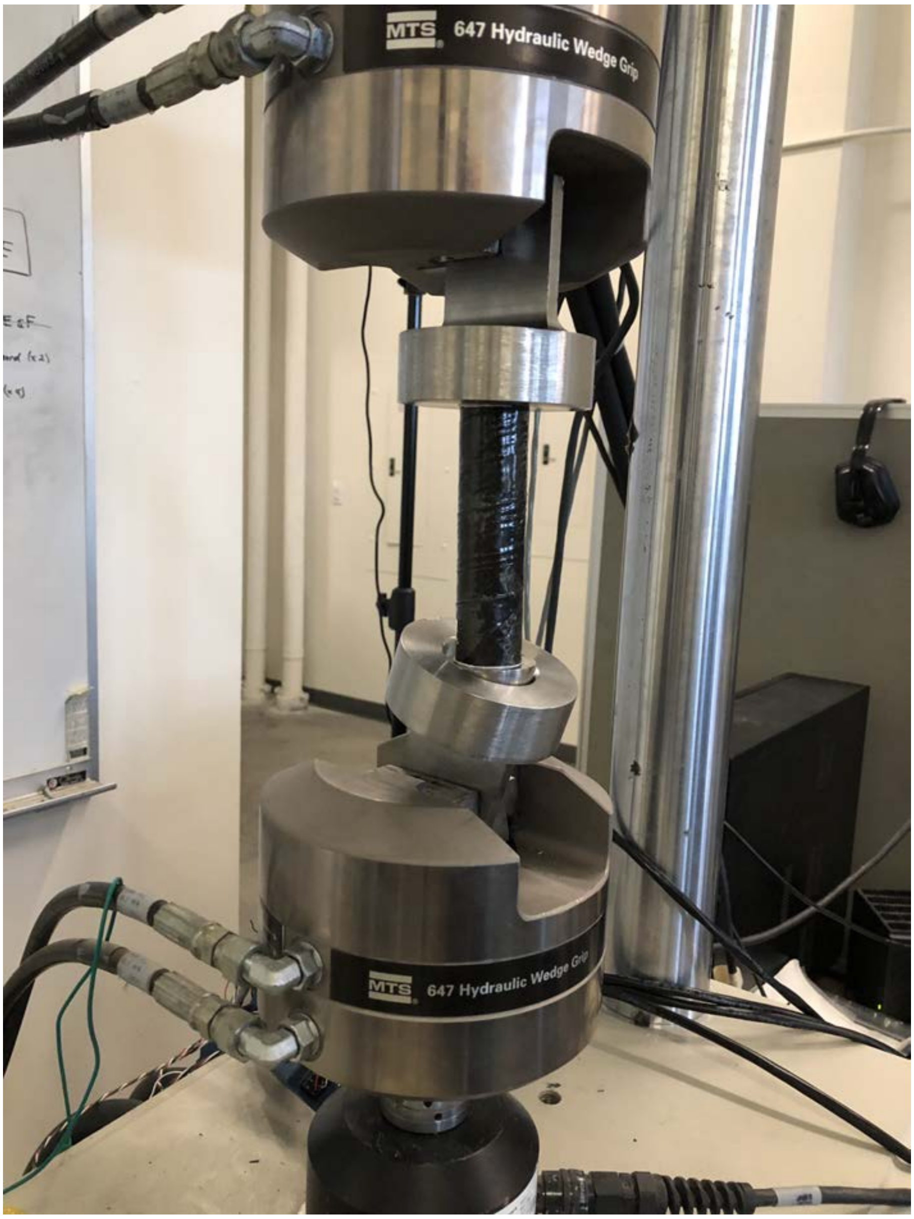

Figure 7.11.: Compression test setup at 15° offset.

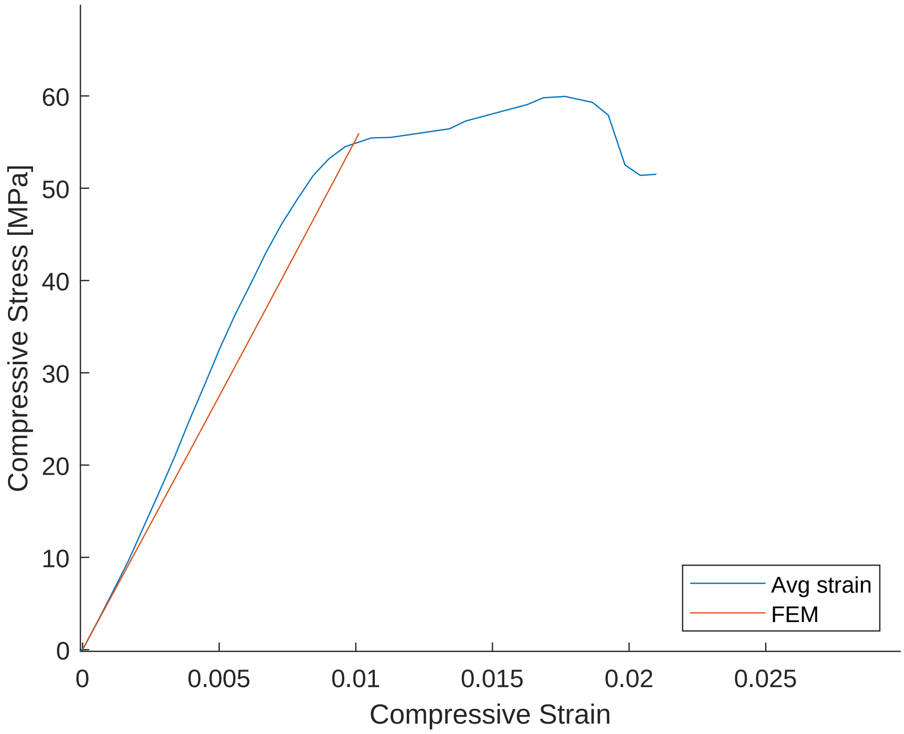

Figure 7.12.: Stress/strain graph 15° offset, loading 2,231.7 N.

Figure 7.13.: Loaded composite cylinder 15° offset, loading 2,231.7 N.

Table 7.7.: Experimental determined stress and strain of the composite cylinder 15° offset, 2,231.7 N.

F [N]	σ [MPa]	ϵ_{avg} $[\frac{mm}{mm}]$
28.76	0.82	5.90×10^{-4}
82.48	2.36	1.150×10^{-3}
129.81	3.71	1.730×10^{-3}
236.97	6.77	2.280×10^{-3}
350.15	10.00	2.840×10^{-3}
464.81	13.28	3.400×10^{-3}
592.32	16.92	3.950×10^{-3}
721.20	20.61	4.510×10^{-3}
856.34	24.47	5.080×10^{-3}
999.65	28.56	5.640×10^{-3}
1137.45	32.50	6.210×10^{-3}
1271.87	36.34	6.750×10^{-3}
1401.69	40.05	7.320×10^{-3}
1520.63	43.45	7.900×10^{-3}
1637.08	46.77	8.450×10^{-3}
1744.74	49.85	9.020×10^{-3}
1839.60	52.56	9.600×10^{-3}
1927.81	55.08	1.0170×10^{-2}
1991.24	56.89	1.0740×10^{-2}
2037.31	58.21	1.1340×10^{-2}
2070.58	59.16	1.2300×10^{-2}
2072.71	59.22	1.3020×10^{-2}
2105.66	60.16	1.5170×10^{-2}
2134.74	60.99	1.5750×10^{-2}
2197.16	62.78	1.8010×10^{-2}
2222.81	63.51	1.8590×10^{-2}
2228.01	63.66	1.9380×10^{-2}
2205.24	63.01	2.0390×10^{-2}
2157.16	61.63	2.0970×10^{-2}
1968.08	56.23	2.1580×10^{-2}
1928.41	55.10	2.2140×10^{-2}
1932.71	55.22	2.2730×10^{-2}

Table 7.8.: Numerical determined stress and strain of the composite cylinder 15° offset.

F [N]	σ_{III} [MPa]	ϵ_{III} [$\frac{mm}{mm}$]
110.70	2.7753	5.08020×10^{-4}
221.49	5.5529	1.01580×10^{-3}
332.37	8.3327	1.52340×10^{-3}
443.35	11.115	2.03080×10^{-3}
554.39	13.899	2.53790×10^{-3}
665.56	16.686	3.04480×10^{-3}
776.81	19.475	3.55160×10^{-3}
888.13	22.266	4.05810×10^{-3}
999.58	25.06	4.56430×10^{-3}
1111.10	27.856	5.07030×10^{-3}
1222.75	30.655	5.57610×10^{-3}
1334.43	33.455	6.08160×10^{-3}
1446.28	36.259	6.58690×10^{-3}
1558.16	39.064	7.09210×10^{-3}
1670.17	41.872	7.59680×10^{-3}
1782.29	44.683	8.10140×10^{-3}
2006.81	47.496	8.60570×10^{-3}
2119.2	50.312	9.10970×10^{-3}
2119.22	53.13	9.61350×10^{-3}
2231.7	55.95	1.01170×10^{-2}

8. Results of the Compression Testing of the Composite Cylinders—New Test Fixture

In this chapter, the composite cylinders, manufactured using the filament-winding technique, are subjected to compression. Because of the issues with the slipping of the test fixture in the grip in the previous tests (see chapter 7), a new test fixture was designed and used for these tests. With the new design, the test fixture did not have to be clamped with an offset into the grip. Consequently, it did not slip in the grip.
Two different cylinders are used for each test. One cylinder (Cyl. 1) is winded with two layers and the other cylinder (Cyl. 2) is winded with three layers.
Due to the offset, one side of the cylinder will be shortened and one side will be lengthened. For this research, the influence of the strain on these sides of the cylinder is the focus. Consequently, two precision linear strain gauges have been attached on Cyl. 1 specimens. The strain gauges, attached at the lower third of the two earlier described sides of the cylinder, measure the strain of each side separately. The assignments of SG1 and SG2 to the position on the cylinders are shown in the figures of each subsection.

In Figure 8.1, the average stress/strain curves of both cylinders are plotted for each offset. With some exceptions (see chapters 8.1 and 8.4), a higher force is required to cause a failure in Cyl. 2 compared to Cyl. 1. Moreover, less force is required to cause failure with increasing offset. However, because of some material imperfections, Cyl. 1 with an offset of 0° failed at a lower load than Cyl. 1 with an offset of 5° (see chapter 8.1, 8.3).

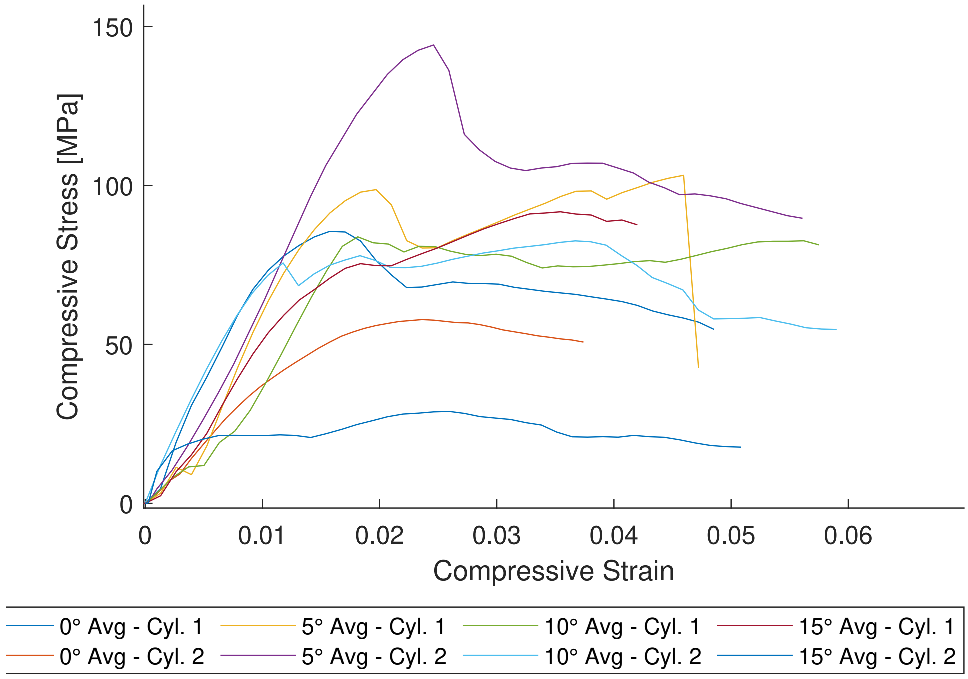

Figure 8.1.: Comparison of the different stress/strain graphs, different loadings.

8.1. Result of Compression Test Using an Offset of 0°

In Figure 8.2, the setup of the test fixture is shown. The stress/strain graph is shown in Figure 8.3. In this graph, the average strain and the actual strain, measured by the two SGs, of the cylinder winded with two layers are plotted. The average strain of Cyl. 2 is also plotted in this graph. The values of the applied force and the determined stress and strain values for both cylinders can be found in table 8.1.

In this paragraph, the results of Cyl. 1 will be discussed in more detail. The first debonding and microcracking of the composite material of the first cylinder was caused by a stress of $\sigma_1 = 70.25$ MPa and an average strain of $\epsilon_{1,avg} = 1.439 \times 10^{-2} \frac{\text{mm}}{\text{mm}}$. At this stress level, the breakdown process of the material started. However, the laminate did not fail at this point. After reaching $\sigma_{1,max} = 88.47$ MPa and an average strain of $\epsilon_{1,avg} = 2.095 \times 10^{-2} \frac{\text{mm}}{\text{mm}}$, the material fails abruptly. However, some local matrix failure had started already, before reaching the inflection point of the average strain line of Cyl. 1.

In figures 8.4 and 8.5, the damaged cylinder is shown. The right cylinder is Cyl. 1 and the left cylinder is Cyl. 2. In these figures, the delamination of the composite material, which was caused by compression load of the cylinder, is also shown. In this test, the delamination of the cylinder occurred at the upper area of the back side of the cylinder

and leads to the middle area of the front side of the cylinder.
Cyl. 2 shows the same damage type in the same area of the cylinder.
The only difference between both cylinders is the required force to cause the failure. In this test, Cyl. 2 failed at a force of 2,722.25 N, which is lower than the force applied on Cyl. 1. Because of material imperfections, the stress concentration in Cyl. 2 was locally higher, which caused a local damage to the structure. Consequently, less force was required to cause the failure.

Figure 8.2.: Compression test setup at 0° offset.

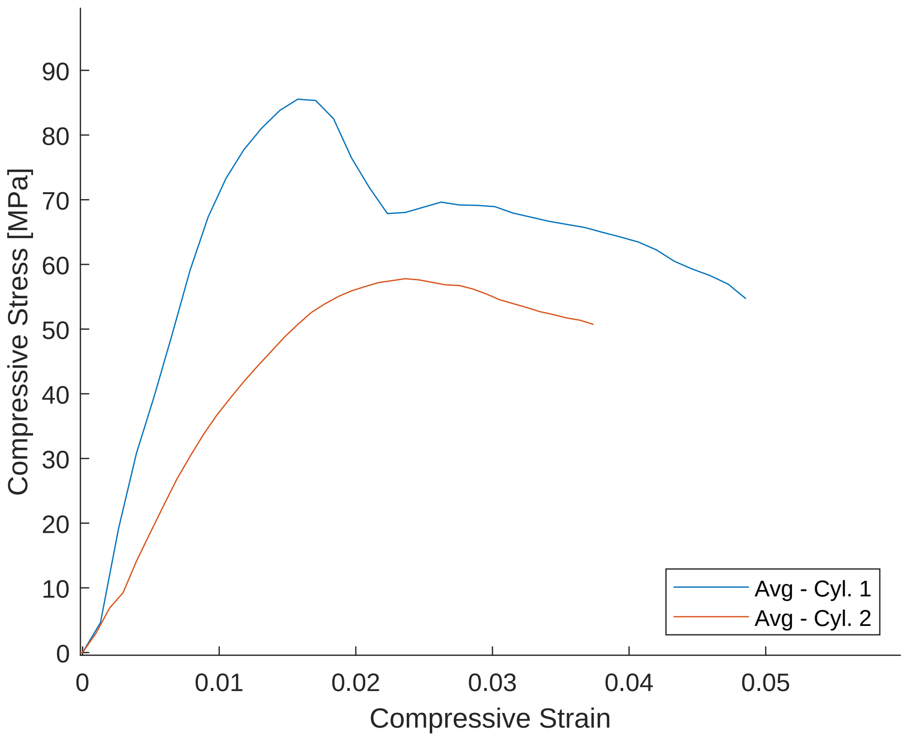

Figure 8.3.: Stress/strain graph 0° offset—new test fixture.

Figure 8.4.: Damage of the composite cylinder 0° offset—front side.

Table 8.1.: Experimental determined stress and strain of the composite cylinder 0° offset—new test fixture.

F_1 [N]	σ_1 [MPa]	$\epsilon_{1,avg}$ $[\frac{mm}{mm}]$	F_2 [N]	σ_2 [MPa]	$\epsilon_{2,avg}$ $[\frac{mm}{mm}]$
0	0	0	0	0	0
57.71	1.65	0.00126	4.86	0.10	0.00095
59.12	1.69	0.00258	5.31	0.11	0.00193
100.06	2.86	0.00389	5.79	0.12	0.00291
102.63	2.93	0.0052	147.21	3.13	0.0039
264.31	7.55	0.00651	329.48	7.01	0.00489
772.2	22.06	0.00783	439.52	9.35	0.00587
1179.66	33.7	0.00914	668.32	14.22	0.00685
1490.59	42.59	0.01045	871.22	18.54	0.00784
1827.47	52.21	0.01177	1068.88	22.74	0.00882
2171.07	62.03	0.01307	1263.31	26.88	0.0098
2458.6	70.25	0.01439	1433.11	30.49	0.01079
2668.04	76.23	0.0157	1592.98	33.89	0.01178
2823.53	80.67	0.01701	1734.08	36.90	0.01276
2940.57	84.02	0.01832	1856.58	39.50	0.01374
3035.73	86.74	0.01964	1976.35	42.05	0.01473
3096.43	88.47	0.02095	2085.86	44.38	0.01571
3089.3	88.27	0.02226	2190.6	46.61	0.01669
2990.63	85.45	0.02357	2296.94	48.87	0.01768
2777.84	79.37	0.02489	2389.39	50.84	0.01866
2617.31	74.78	0.0262	2476.22	52.69	0.01965
2477.62	70.79	0.02751	2538.28	54.01	0.02063
2483.58	70.96	0.02882	2592.31	55.16	0.02162
2511.48	71.76	0.03013	2633.91	56.04	0.0226
2539.72	72.56	0.03145	2664.65	56.69	0.02358
2524.12	72.12	0.03276	2693.62	57.31	0.02457
2521.94	72.06	0.03407	2707.75	57.61	0.02555
2515.01	71.86	0.03538	2722.25	57.92	0.02654
2480.51	70.87	0.0367	2713.54	57.73	0.02752
2458.57	70.24	0.03801	2695.4	57.35	0.02851
2436.12	69.6	0.03932	2677.34	56.96	0.02949
2419.34	69.12	0.04063	2672.7	56.87	0.03047
2402.29	68.64	0.04195	2647.69	56.33	0.03146
2376.12	67.89	0.04325	2611.6	55.57	0.03245
2351.00	67.17	0.04457	2569.93	54.68	0.03342
2323.71	66.39	0.04588	2541.42	54.07	0.03441
2281.77	65.19	0.04719	2513.06	53.47	0.0354
2219.61	63.42	0.04851	2482.57	52.82	0.03638
2177.75	62.22	0.04982	2461.37	52.37	0.03736
2141.92	61.2	0.05113	2436.82	51.85	0.03835
2095.66	59.88	0.05245	2420.09	51.49	0.03933
2017.16	57.63	0.05375	2389.48	50.84	0.04031

8.2. Result of Compression Test Using an Offset of 5°

In Figure 8.6, the setup of the test fixture is shown. The stress/strain graph is shown in Figure 8.7. In this graph, the average strain and the actual strain, measured by the two SGs, of the cylinder manufactured with two layers are plotted. The average strain of Cyl. 2 is also plotted in this graph. The average strain line differs from the SG lines, because the strain was calculated from the measured displacement of the compression testing machine. This displacement is measured from grip to grip. Consequently, the average strain is higher than the actual strain measured by the SGs. The values of the applied force and the determined stress and strain values for both cylinders can be found in table 8.2.

In this paragraph, the results of Cyl. 1 will be discussed in more detail. The first debonding and microcracking of the composite material of the first cylinder was caused by a stress of $\sigma_1 = 98.67$ MPa and an average strain of $\epsilon_{1,avg} = 1.9697 \times 10^{-2} \frac{\text{mm}}{\text{mm}}$. At this stress level, the breakdown process of the material started. However, the laminate did not fail at this point. After that, less force is required to cause a larger strain. However, after reaching a strain of $\epsilon_{1,avg} = 2.429 \times 10^{-2} \frac{\text{mm}}{\text{mm}}$, more force is required to cause a larger strain. After reaching $\sigma_{1,max} = 103.18$ MPa and an average strain of $\epsilon_{1,avg} = 4.7222 \times 10^{-2} \frac{\text{mm}}{\text{mm}}$, the ultimate compression strength of the cylinder is reached and the material fails abruptly. However, some local matrix failure started already, before reaching the inflection point of the average strain line of Cyl. 1.

The maximum strains of $\epsilon_{SG1} = 6.722 \times 10^{-3} \frac{\text{mm}}{\text{mm}}$ and $\epsilon_{SG2} = 5.030 \times 10^{-3} \frac{\text{mm}}{\text{mm}}$ were measured by the attached SGs.

In figures 8.8 and 8.9, the damaged cylinders are shown. The left cylinder is Cyl. 2 and the right cylinder is Cyl. 1. In these figures, the delamination of the composite material, which was caused by buckling of the cylinder, is also shown. In this test, the delamination of the cylinder occurred only at the shortened side of the upper third area of the cylinder.

Cyl. 2 shows the same damage type in the same, upper third, area of the cylinder. Additionally, the delamination occurred also in the lower area of the cylinder at the opposite side.

A higher force of 6,775.83 N had to be applied to cause the failure of Cyl. 2.

Figure 8.6.: Compression test setup at 5° offset.

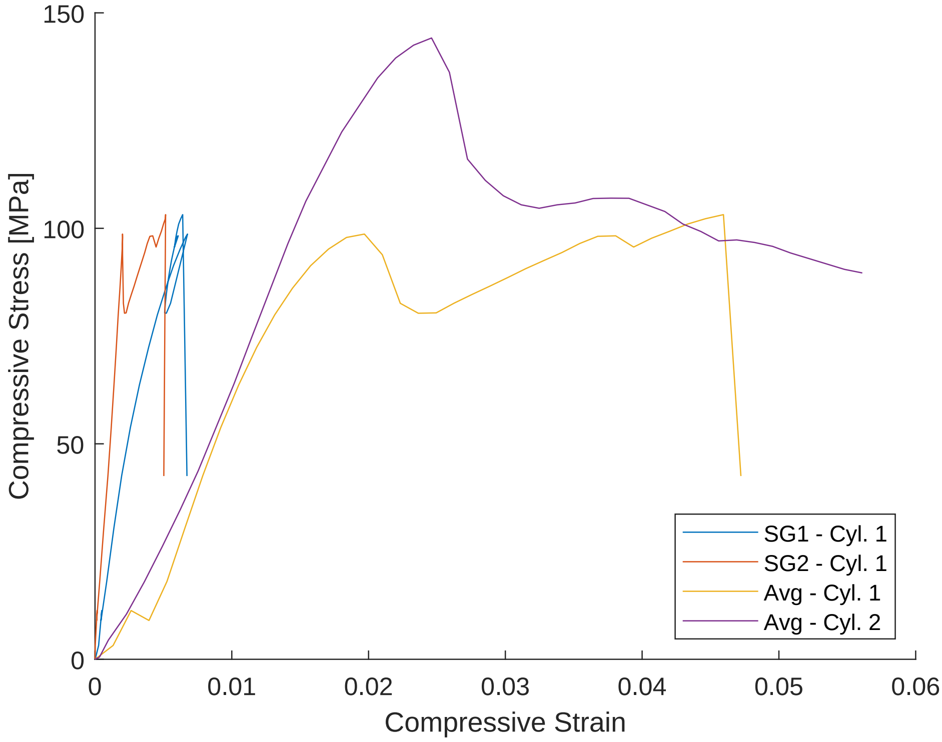

Figure 8.7.: Stress/strain graph 5° offset—new test fixture.

Figure 8.8 : Damage of the composite cylinder 5° offset - front side

Figure 8.9.: Damage of the composite cylinder 5° offset—back side.

Table 8.2.: Experimental determined stress and strain of the composite cylinder 5° offset—new test fixture.

F_1 [N]	σ_1 [MPa]	$SG1_1$ [$\frac{mm}{mm}$]	$SG2_1$ [$\frac{mm}{mm}$]	$\epsilon_{1,avg}$ [$\frac{mm}{mm}$]	F_2 [N]	σ_2 [MPa]	$\epsilon_{2,avg}$ [$\frac{mm}{mm}$]
0	0	0	0	0	0	0	0
18.6	0.01	0.000017	0.000002	0.000008	23.95	0.51	0.000327
130.72	3.21	0.000263	0.000015	0.001323	209.92	4.47	0.000979
414.01	11.31	0.000493	0.000154	0.002638	491.41	10.46	0.002294
333.72	9.01	0.000438	0.000118	0.003946	844.76	17.97	0.003606
650.85	18.07	0.000856	0.000344	0.005261	1229.82	26.17	0.004918
1084.29	30.46	0.00138	0.000639	0.006573	1631.11	34.70	0.006229
1511.35	42.66	0.001952	0.000946	0.007885	2056.06	43.75	0.007545
1901.73	53.81	0.002587	0.001187	0.009199	3006.72	63.97	0.01017
2247.47	63.69	0.003248	0.001387	0.010509	3520.05	74.89	0.011478
2551.8	72.39	0.00392	0.001557	0.01182	4534.59	96.48	0.014105
2815.83	79.93	0.004559	0.001696	0.013139	4995.86	106.29	0.015414
3032.77	86.13	0.005176	0.001824	0.014442	5751.44	122.37	0.01804
3214.96	91.33	0.005737	0.001921	0.015763	6340.64	134.91	0.020665
3349.64	95.18	0.006225	0.001986	0.017069	6557.17	139.51	0.021978
3444.21	97.88	0.006613	0.002016	0.018384	6697.37	142.50	0.02329
3471.83	98.67	0.006761	0.00201	0.019697	6775.83	144.17	0.024605
3303.77	93.87	0.006395	0.002014	0.021007	6401.65	136.21	0.025911
2909.23	82.6	0.005521	0.002075	0.02232	5454.8	116.06	0.027232
2828.9	80.3	0.005216	0.002155	0.023635	5222.39	111.11	0.028538
2831.45	80.38	0.00509	0.002275	0.024942	5055.04	107.55	0.029853
2911.06	82.65	0.005143	0.002453	0.026262	4956.42	105.46	0.031164
2981.17	84.66	0.005212	0.002656	0.027567	4918.91	104.66	0.032475
3049.55	86.61	0.005293	0.00286	0.028883	4956.53	105.46	0.033794
3119.69	88.61	0.005379	0.003054	0.030195	4976.63	105.89	0.0351
3191.39	90.66	0.005486	0.003259	0.031504	5025.26	106.92	0.036414
3257.26	92.54	0.005589	0.003449	0.032824	5029.19	107.00	0.037727
3321.25	94.37	0.005714	0.003633	0.034129	5027.75	106.97	0.039037
3395.49	96.49	0.005864	0.00382	0.035446	4883.56	103.91	0.041663
3453.44	98.15	0.006011	0.004012	0.036756	4747.44	101.01	0.042973
3457.4	98.26	0.006085	0.00422	0.038068	4665.89	99.27	0.044293
3366.45	95.66	0.00581	0.004464	0.039381	4562.65	97.08	0.045596
3438.06	97.71	0.005898	0.004666	0.040696	4573.62	97.31	0.046916
3494.07	99.31	0.005996	0.004851	0.042003	4545.79	96.72	0.048223
3553.02	100.99	0.006116	0.005006	0.043322	4503.55	95.82	0.049538
3596.34	102.23	0.006267	0.005141	0.044627	4431.4	94.29	0.05085
3629.47	103.18	0.006409	0.00516	0.045946	4252.71	90.48	0.054789
1506.44	42.52	0.006722	0.00503	0.047222	4213.54	89.65	0.056097

8.3. Result of Compression Test Using an Offset of 10°

In Figure 8.10, the setup of the test fixture is shown. The stress/strain graph is shown in Figure 8.11. In this graph, the average strain and the actual strain, measured by the two SGs, of the cylinder manufactured with two layers are plotted. The average strain of the cylinder manufactured with three layers is also plotted in this graph. The average strain line differs from the SG lines, because the strain was calculated from the measured displacement of the compression testing machine. This displacement is measured from grip to grip. Consequently, the average strain is higher than the actual strain measured by the SGs. The values of the applied force and the determined stress and strain values for both cylinders can be found in table 8.3.
In this paragraph, the results of Cyl. 1 will be discussed in more detail. The first debonding and microcracking of the composite material of the first cylinder was caused by a stress of $\sigma_1 = 83.82$ MPa and an average strain of $\epsilon_{1,avg} = 1.814 \times 10^{-2} \frac{\text{mm}}{\text{mm}}$. At this stress level, the breakdown process of the material started. However, the laminate did not fail at this point. Less force is required to cause a larger strain, until $\sigma_1 = 74.40$ MPa and an average strain of $\epsilon_{1,avg} = 3.651 \times 10^{-2} \frac{\text{mm}}{\text{mm}}$ are reached. Some local matrix failure had started already, before reaching the inflection point of the average strain line of Cyl. 1.
The maximum strains of $\epsilon_{SG1} = 1.190 \times 10^{-2} \frac{\text{mm}}{\text{mm}}$, $\epsilon_{SG2} = 1.1107 \times 10^{-2} \frac{\text{mm}}{\text{mm}}$ were measured by the attached SG.
In figures 8.12, 8.13 and 8.14, the damaged cylinder is shown. The left cylinder is Cyl. 2 and the right cylinder is Cyl. 1. In these figures, the delamination of the composite material, which was caused by buckling of the cylinder, is also shown. The delamination at the upper area of the cylinder occurred at the shortened side of the upper third of the cylinder. The delamination of the lower area of the cylinder occurred at the opposite side.
Cyl. 2 shows the same damage type in the same areas of the cylinder. The only difference between both cylinders is the required force to cause the failure. In this test,
Cyl. 2 failed at a force of 3,857.41 N, which is lower than the force applied on Cyl. 1.

Figure 8.10.: Compression test setup at 10° offset.

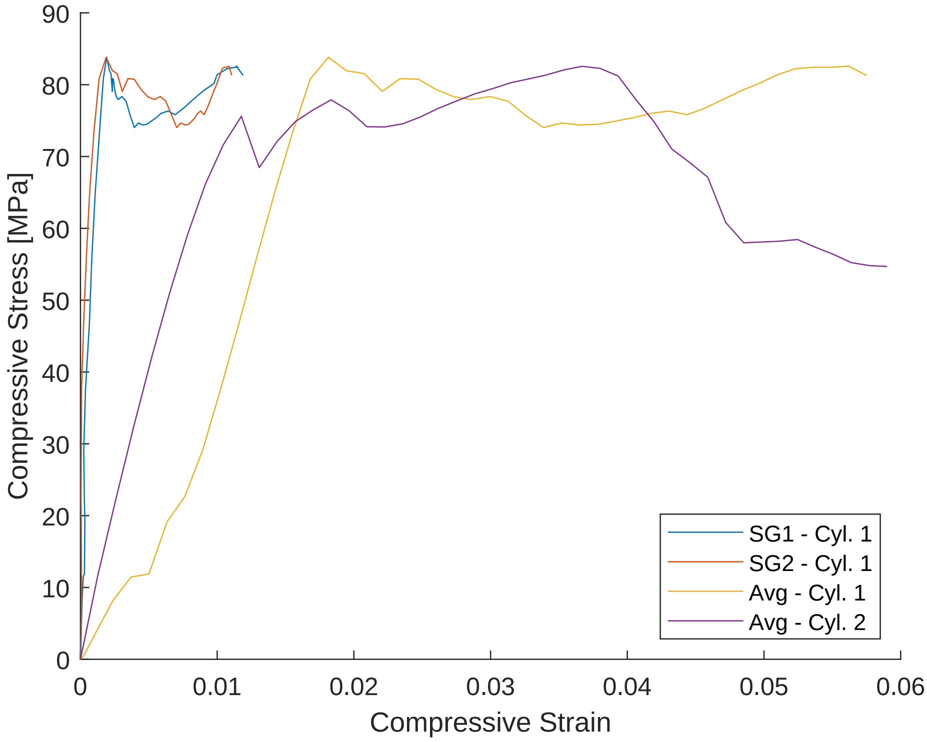

Figure 8.11.: Stress/strain graph 10° offset—new test fixture.

Figure 8.13.: Damage of the composite cylinder 10° offset—right side.

Figure 8.14.: Damage of the composite cylinder 10° offset—back side.

Table 8.3.: Experimental determined stress and strain of the composite cylinder 10° offset—new test fixture.

F_1 [N]	σ_1 [MPa]	$SG1_1$ [$\frac{mm}{mm}$]	$SG2_1$ [$\frac{mm}{mm}$]	$\epsilon_{1,avg}$ [$\frac{mm}{mm}$]	F_2 [N]	σ_2 [MPa]	$\epsilon_{2,avg}$ [$\frac{mm}{mm}$]
0	0	0	0	0	0	0	0
125.12	3.57	0.00005	0.00006	0.00108	1044.96	22.23	0.00258
288.12	8.23	0.00012	0.00008	0.00239	1520.96	32.36	0.00389
400.88	11.45	0.0002	0.00008	0.0037	1976.42	42.05	0.00521
416.12	11.89	0.00029	0.00007	0.00501	2395.75	50.97	0.00652
669.55	19.13	0.00032	0.00006	0.00633	2777.88	59.10	0.00783
793.88	22.68	0.00028	0.00004	0.00764	3109.77	66.17	0.00914
1021.8	29.19	0.00024	0.00006	0.00895	3367.42	71.65	0.01045
1318.21	37.66	0.00037	0.00008	0.01026	3553.09	75.60	0.01177
1633.31	46.67	0.00065	0.00023	0.01158	3217.23	68.45	0.01308
1957.53	55.93	0.00083	0.00043	0.01289	3389.2	72.11	0.01439
2566.17	73.32	0.00139	0.00098	0.01551	3594.33	76.48	0.01701
2829.04	80.83	0.00167	0.00136	0.01682	3660.87	77.89	0.01833
2933.84	83.82	0.00192	0.00188	0.01814	3590.28	76.39	0.01964
2868.33	81.95	0.00212	0.00234	0.01945	3484.91	74.15	0.02095
2853.84	81.54	0.00223	0.00269	0.02076	3483.43	74.12	0.02226
2767.05	79.06	0.00233	0.00306	0.02208	3504.06	74.55	0.02358
2829.69	80.85	0.00235	0.00348	0.02338	3549.76	75.53	0.02489
2827.04	80.77	0.00241	0.00393	0.0247	3606.1	76.73	0.0262
2776.84	79.34	0.0025	0.00443	0.02601	3652.99	77.72	0.02751
2740.85	78.31	0.00262	0.00494	0.02732	3699.53	78.71	0.02883
2727.68	77.93	0.00276	0.0054	0.02864	3733.84	79.44	0.03014
2742.13	78.35	0.00303	0.00584	0.02995	3772.21	80.26	0.03145
2720.32	77.72	0.00333	0.00624	0.03126	3797.33	80.79	0.03276
2649.94	75.71	0.00364	0.00668	0.03257	3823.37	81.35	0.03407
2591.09	74.03	0.00394	0.00704	0.03388	3857.41	82.07	0.03539
2613.43	74.67	0.00424	0.00734	0.0352	3879.85	82.55	0.0367
2606.95	74.48	0.00484	0.0079	0.03782	3816.57	81.20	0.03933
2622.17	74.92	0.00518	0.00814	0.03914	3661.48	77.90	0.04064
2639.03	75.4	0.00554	0.00837	0.04044	3518.18	74.85	0.04195
2660.78	76.02	0.00591	0.00858	0.04176	3338.59	71.03	0.04326
2671.53	76.33	0.0064	0.00879	0.04307	3250.59	69.16	0.04457
2653.86	75.82	0.00692	0.00904	0.04438	3154.17	67.11	0.04589
2686.73	76.76	0.00756	0.00928	0.0457	2858.07	60.81	0.0472
2727.98	77.94	0.00824	0.00952	0.04701	2725.76	57.99	0.04852
2770.26	79.15	0.00899	0.00976	0.04832	2730.36	58.09	0.04982
2805.87	80.17	0.00977	0.00999	0.04963	2735.7	58.21	0.05114
2877.31	82.21	0.0107	0.01037	0.05226	2696.36	57.37	0.05376
2884.53	82.42	0.0113	0.01051	0.05357	2650.11	56.39	0.05507
2885.04	82.43	0.0115	0.01069	0.05488	2595.55	55.22	0.05639
2890.18	82.58	0.0114	0.01087	0.0562	2576.33	54.82	0.0577
2845.06	81.29	0.0119	0.01107	0.0575	2570.15	54.68	0.05901

8.4. Result of Compression Test Using an Offset of 15°

In Figure 8.15, the setup of the test fixture is shown. The stress/strain graph is shown in Figure 8.16. In this graph, the average strain and the actual strain, measured by the two SGs, of the cylinder manufactured with two layers are plotted. The average strain of the cylinder manufactured with three layers is plotted in this graph, too. The values of the applied force and the determined stress and strain values for both cylinders can be found in table 8.4.

In this paragraph, the results of Cyl. 1 will be discussed in more detail. The first debonding and microcracking of the composite material of the first cylinder was caused by a stress of $\sigma_1 = 78.96$ MPa and an average strain of $\epsilon_{1,avg} = 2.3625 \times 10^{-2} \frac{\text{mm}}{\text{mm}}$. At this stress level, the breakdown process of the material started. However, the laminate did not fail at this point. Less force is required to cause a larger strain, until $\sigma_{1,max} = 99.85$ MPa and an average strain of $\epsilon_{1,avg} = 4.3311 \times 10^{-2} \frac{\text{mm}}{\text{mm}}$ are reached. The maximum strains of $\epsilon_{SG1} = 1.0900 \times 10^{-2} \frac{\text{mm}}{\text{mm}}$ and $\epsilon_{SG2} = 4.810 \times 10^{-3} \frac{\text{mm}}{\text{mm}}$ were measured by the attached SG.

In figures 8.17, 8.18 and 8.19, the damaged cylinder is shown. The left cylinder is Cyl. 2 and the right cylinder is Cyl. 1. In these figures, the delamination of the composite material, which was caused by buckling of the cylinder, is also shown. The delamination at the upper area of the cylinder occurred at the shortened side of the upper third of the cylinder. The delamination of the lower area of the cylinder occurred at the opposite side.

Cyl. 2 shows the same damage type in the same, upper third, area of the cylinder. The only difference between both cylinders is the required force to cause the failure. In this test, Cyl. 2 failed at a force of 1,359.01 N, which is lower than the force applied on Cyl. 1. Because of material imperfections, the stress concentration in Cyl. 2 was locally higher, which caused a local damage to the structure. Consequently, less force was required to cause the failure.

Figure 8.15.: Compression test setup at 15° offset.

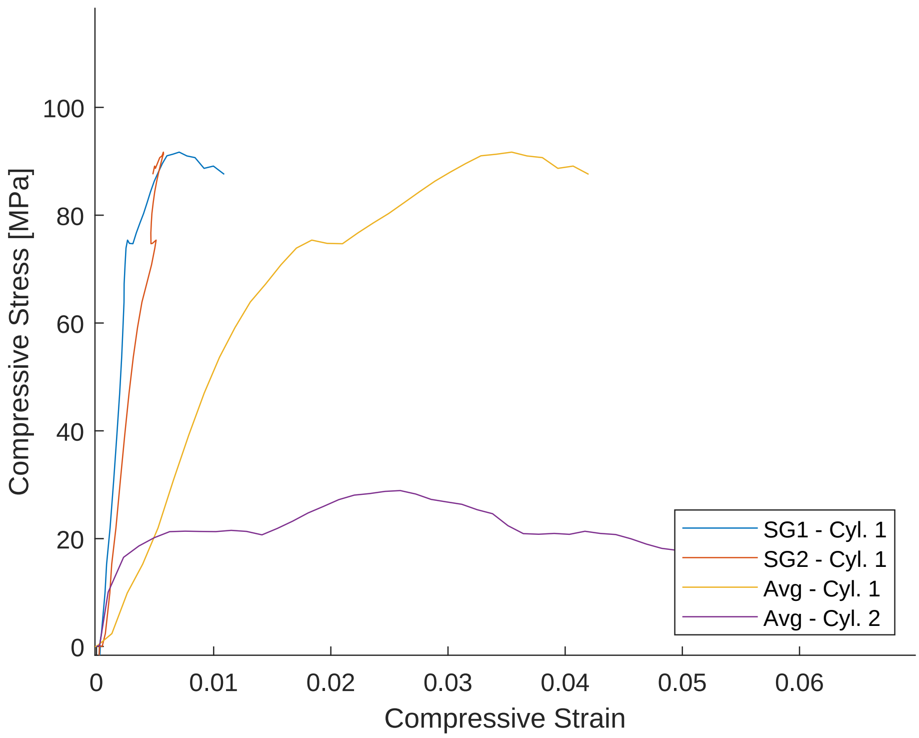

Figure 8.16.: Stress/strain graph 15° offset—new test fixture.

Figure 8.18.: Damage of the composite cylinder 15° offset—right side.

Figure 8.19.: Damage of the composite cylinder 15° offset—top side.

Table 8.4.: Experimental determined stress and strain of the composite cylinder 15° offset—new test fixture.

F_1 [N]	σ_1 [MPa]	$SG1_1$ [$\frac{mm}{mm}$]	$SG2_1$ [$\frac{mm}{mm}$]	$\epsilon_{1,avg}$ [$\frac{mm}{mm}$]	F_2 [N]	σ_2 [MPa]	$\epsilon_{2,avg}$ [$\frac{mm}{mm}$]
0	0	0	0	0	0	0	0
0.19	0.53	0.00002	0.000025	0.001264	7.83	0.17	0.000268
40.81	0.64	0.000061	0.000092	0.000009	473.47	10.07	0.000997
119.87	2.9	0.000152	0.000148	0.001313	777.18	16.54	0.002312
190.52	4.92	0.000221	0.000179	0.002629	876.04	18.64	0.003619
260.98	6.94	0.0003	0.000233	0.00394	948.51	20.18	0.004938
309.7	8.33	0.000319	0.000252	0.005252	1000.9	21.30	0.006244
306.57	8.24	0.000264	0.00026	0.006569	1005.17	21.39	0.007559
303.5	8.15	0.000257	0.000484	0.007876	1002.69	21.33	0.008872
386.63	10.53	0.00042	0.000757	0.009189	1001.28	21.30	0.010181
650.22	18.06	0.000728	0.00114	0.010503	1012.19	21.54	0.0115
837.38	23.4	0.000863	0.0013	0.011815	1003.1	21.34	0.012807
1072.28	30.12	0.00116	0.00166	0.013127	973.06	20.70	0.014123
1382.38	38.98	0.00147	0.00204	0.01444	1028.95	21.89	0.015432
1674.97	47.34	0.00174	0.00241	0.015749	1092.52	23.25	0.016745
1948.12	55.14	0.00198	0.00278	0.017069	1164.01	24.77	0.018059
2180.82	61.79	0.00215	0.00314	0.018373	1220.98	25.98	0.019371
2372.98	67.28	0.00226	0.0035	0.019691	1280.06	27.24	0.02068
2539.21	72.03	0.00235	0.00388	0.020999	1319.53	28.08	0.021998
2656.97	75.39	0.00236	0.00428	0.022314	1332.82	28.36	0.023305
2782.01	78.96	0.00244	0.0047	0.023625	1351.98	28.77	0.024621
2889.97	82.05	0.00252	0.00498	0.024938	1359.01	28.92	0.02593
2941.91	83.53	0.00265	0.00509	0.02625	1329.04	28.28	0.027244
2920.52	82.92	0.00281	0.00477	0.027565	1282.14	27.28	0.028558
2918.29	82.86	0.00311	0.00465	0.028872	1260.35	26.82	0.029868
2988.83	84.87	0.0034	0.00464	0.03019	1239.44	26.37	0.03118
3053.04	86.71	0.00371	0.00468	0.031499	1192.1	25.36	0.032495
3114.39	88.46	0.00402	0.00473	0.032811	1157.3	24.62	0.033805
3184.68	90.47	0.00432	0.00484	0.034126	1052.84	22.40	0.035119
3255.32	92.49	0.00461	0.00497	0.035434	983.62	20.93	0.03643
3324.03	94.45	0.00493	0.00514	0.036752	978.48	20.82	0.037742
3382.86	96.13	0.00528	0.00531	0.03806	985.42	20.97	0.03906
3438.47	97.72	0.00562	0.00549	0.039375	977.62	20.80	0.040363
3489.3	99.17	0.00601	0.00566	0.040686	1004.27	21.37	0.041685
3499.28	99.46	0.00651	0.00572	0.041998	985.36	20.97	0.042989
3513.08	99.85	0.00706	0.00571	0.043311	975.85	20.76	0.044305
3488.21	99.14	0.00772	0.00559	0.044624	938.57	19.97	0.045618
3477.2	98.83	0.00841	0.0054	0.045933	892.66	18.99	0.046928
3407.65	96.84	0.00918	0.00503	0.047251	855.26	18.20	0.048242
3422.24	97.26	0.00998	0.00496	0.048556	837.97	17.83	0.049556
3369.02	95.74	0.0109	0.00481	0.049875	830.34	17.67	0.050862

9. Results of the Numerical Analysis of the Aluminum Alloy Cylinders

In this chapter, the results of the experiments of the numerical analysis of the aluminum alloy cylinders are presented.
In Figure 9.1, the different stress/strain graphs are combined in one graph to provide a first overview. The load applied in the numerical analysis is adjusted to the applied loads in the experimental tests (see chapter 6). Consequently, a comparison between the different graphs in figure 9.1 is only possible up to a specific load.
In this paragraph, the similarities of the tests are described. The yielding point of the material was reached in the tests with an offset of 0° and 5°. Consequently, plasticity did occur and the deformations of these two cylinders were irreversible in the tests. However, the yielding point was not reached in the tests conducted with an offset of 10° and 15°. Hence, plasticity did not occur during these tests and the deformation of these two cylinders was reversible.
The 0° and 5° lines can be divided into two parts. The first parts of these lines rise steeply compared to the second parts. Then after the specific yielding points are reached, the second parts rise less steeply and have a flatter slope gradient. The 10° and 15° lines rise linearly and have a constant slope gradient.
The strain, force and stress values deviate from the experimental data. However, a slight deviation is acceptable. Reasons for the slight deviations of the values might be a too coarse mesh. Refining the mesh leads to more precise results. However, the solving time will increase if the mesh is refined. The correct balance between desired precision of the results and solving time has to be found. Moreover, the test fixture was prevented from slipping because of the fixed support boundary condition. In addition to that, the material properties were only assumed and not exactly determined. Consequently, the assumed Young's modulus is too low in comparison to the actual Young's modulus.

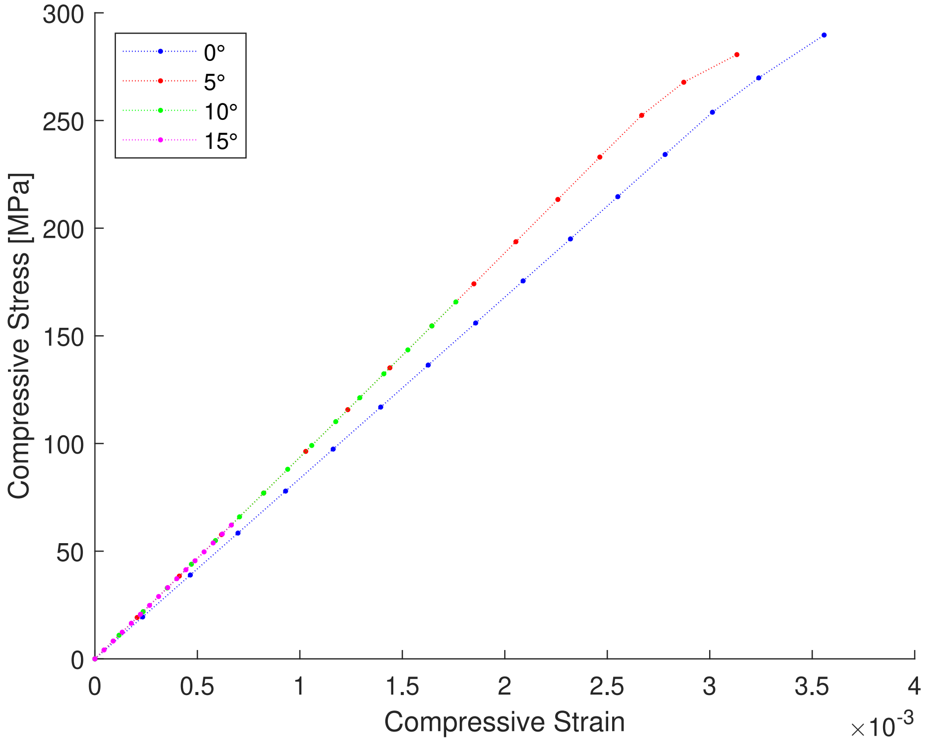

Figure 9.1.: Comparison of the different stress/strain graphs, different loadings.

9.1. Result of Compression Test Using an Offset of 0°

In Figure 9.3, the equivalent stress distribution of the test fixture and the specimen with an offset of 0° is shown. The stress/strain graph is shown in Figure 9.2. The calculated stress and strain values can be found in table 9.1.
A force of 9,776.40 N, which caused a stress of $\sigma_{v,max} = 289.69$ MPa and a strain of $\epsilon_{v,max} = 3.55851 \times 10^{-3} \frac{\text{mm}}{\text{mm}}$, has been applied to the specimen.
The line rises linearly and can be divided into two parts. The first part of the line rises with a steep slope until a stress of approx. $\sigma_v = 269.80$ MPa and a strain of $\epsilon_v = 3.2391 \times 10^{-3} \frac{\text{mm}}{\text{mm}}$ are reached. The slope of the second part of the line is flatter. Consequently, a plastic deformation occurred. Moreover, the maximum stress that occurred is greater than the yield strength of the material $\sigma_y = 276$ (see Eq. 9.1). Thus, the specimen experienced an irreversible deformation.

$$\sigma_{v,max} \geq \sigma_y \tag{9.1}$$

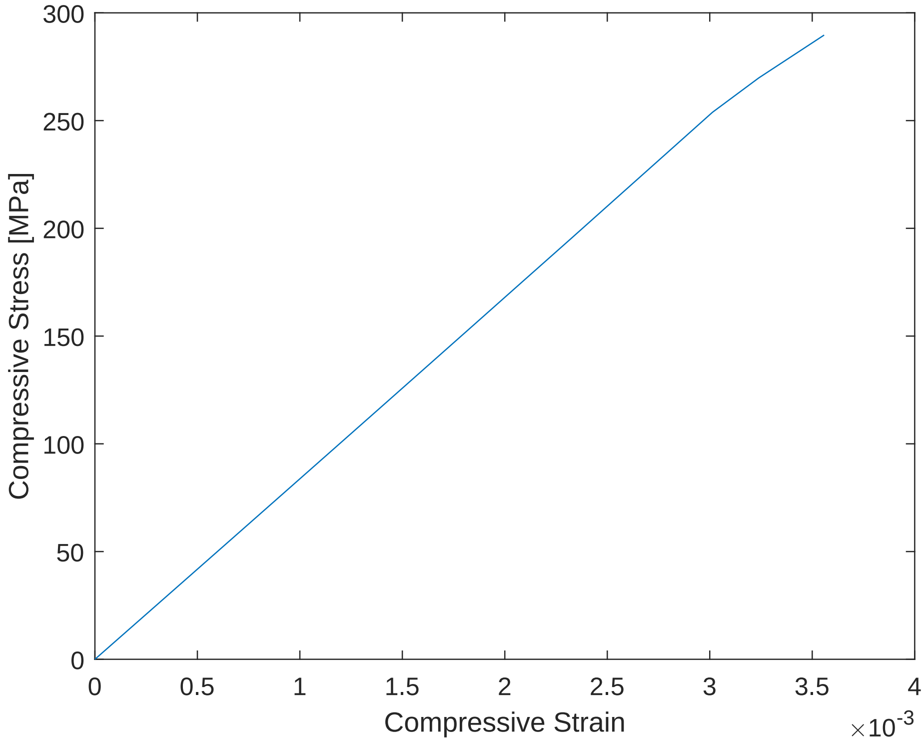

Figure 9.2.: Stress/strain graph 0° offset, loading 9,776.40 N.

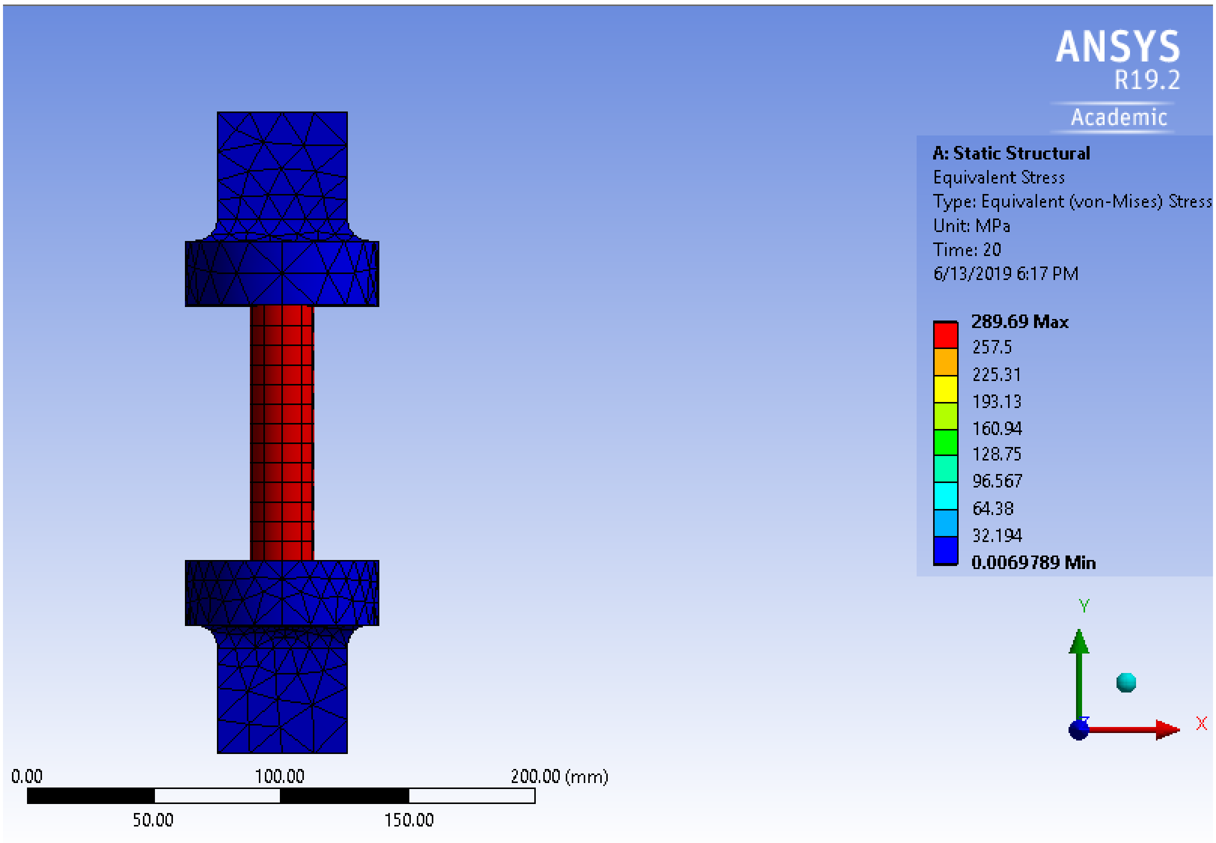

Figure 9.3.: Equivalent stress distribution 0° offset, loading 9,776.40 N.

Table 9.1.: Numerical determined stress and strain of the aluminum cylinder 0° offset, 9,679.94 N.

F [N]	σ_v [MPa]	ϵ_v [$\frac{mm}{mm}$]
657.10	19.47	2.3291×10^{-4}
1314.14	38.94	4.6562×10^{-4}
1971.55	58.42	6.9814×10^{-4}
2629.29	77.91	9.3047×10^{-4}
3287.37	97.41	1.1626×10^{-3}
3945.79	116.92	1.3946×10^{-3}
4604.55	136.44	1.6263×10^{-3}
5434.79	155.97	1.8579×10^{-3}
5923.41	175.52	2.0893×10^{-3}
6581.50	195.02	2.3205×10^{-3}
7243.63	214.64	2.5515×10^{-3}
7904.75	234.23	2.7823×10^{-3}
8566.90	253.85	3.0132×10^{-3}
9105.16	269.80	3.2391×10^{-3}
9776.40	289.69	3.5581×10^{-3}

9.2. Result of Compression Test Using an Offset of 5°

In Figure 9.5, the equivalent stress distribution of the test fixture and the specimen with an offset of 5° is shown. The stress/strain graph is shown in Figure 9.4. The calculated stress and strain values can be found in table 9.2.
A force of 9,436.0 N, which caused a stress of $\sigma_{v,max} = 280.6$ MPa and a strain of $\epsilon_{v,max} = 3.1324 \times 10^{-3} \, \frac{\text{mm}}{\text{mm}}$, has been applied to the specimen.
The line can be divided into two parts. The first part of the line rises with a steep slope until a stress of approx. $\sigma_v = 267.77$ MPa and a strain of $\epsilon_v = 2.87330 \times 10^{-3} \, \frac{\text{mm}}{\text{mm}}$ are reached. The slope of the second part of the line is flatter. Consequently, a plastic deformation did occur. The specimen experienced an irreversible deformation because of $\sigma_{max} \geq \sigma_y$.
Less stress and strain are required to cause yielding and plasticity, compared to the 0° offset.

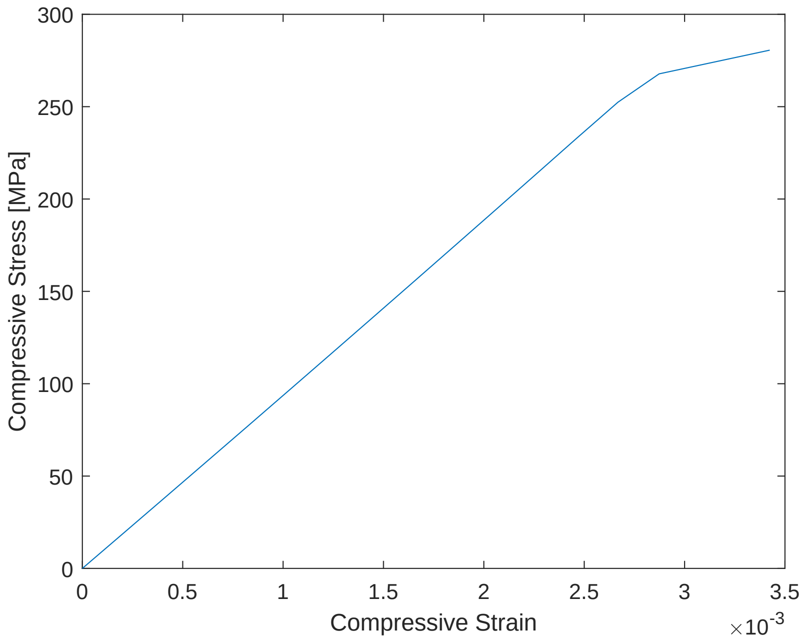

Figure 9.4.: Stress/strain graph 5° offset, loading 9,434.0 N.

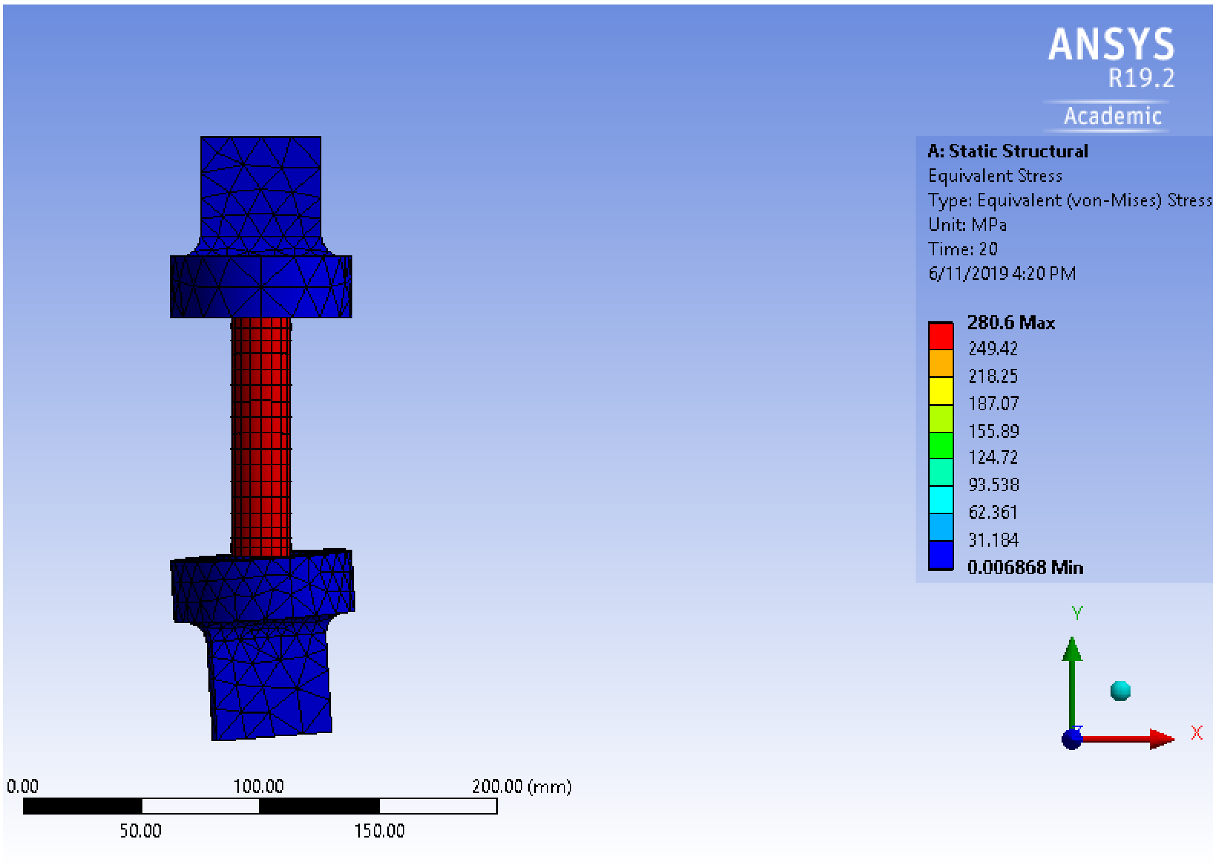

Figure 9.5.: Equivalent stress distribution 5° offset, loading 9,434.0 N.

Table 9.2.: Numerical determined stress and strain of the aluminum cylinder 5° offset, 9,436.0 N.

F [N]	σ_v [MPa]	ϵ_v [$\frac{mm}{mm}$]
646.80	19.197	2.06040×10^{-4}
1294.75	38.428	4.11920×10^{-4}
1943.87	57.694	6.17650×10^{-4}
2594.24	76.997	8.23401×10^{-4}
3245.96	96.34	1.02870×10^{-3}
3898.93	115.72	1.23401×10^{-3}
4553.58	135.15	1.43920×10^{-3}
5209.58	154.62	1.64430×10^{-3}
8567.26	174.14	1.84920×10^{-3}
7188.02	193.71	2.05410×10^{-3}
7433.85	213.34	2.25890×10^{-3}
7851.10	233.02	2.46360×10^{-3}
8504.39	252.41	2.66790×10^{-3}
9021.92	267.77	2.87330×10^{-3}
9436.0	280.06	3.42410×10^{-3}

9.3. Result of Compression Test Using an Offset of 10°

In Figure 9.7, the equivalent stress distribution of the test fixture and the specimen with an offset of 10° is shown. The stress/strain graph is shown in Figure 9.6. The calculated stress and strain values can be found in table 9.3.
A force of 5391.0 N, which caused a stress of $\sigma_{v,max} = 165.75$ MPa and a strain of $\epsilon_{v,max} = 1.7613 \times 10^{-3}\,\frac{\text{mm}}{\text{mm}}$, has been applied to the specimen.
The simulated force for this test was approx. 43% lower than the force used in the previous test (chapter 9.2), which caused a lower stress level and a lower strain. The lower force was chosen to compare the results between the experimental and numerical tests.
The line rises linearly and has a constant slope gradient. A plastic deformation did not occur. Moreover, the specimen experienced a reversible deformation because of $\sigma_{max} \leq \sigma_y$.

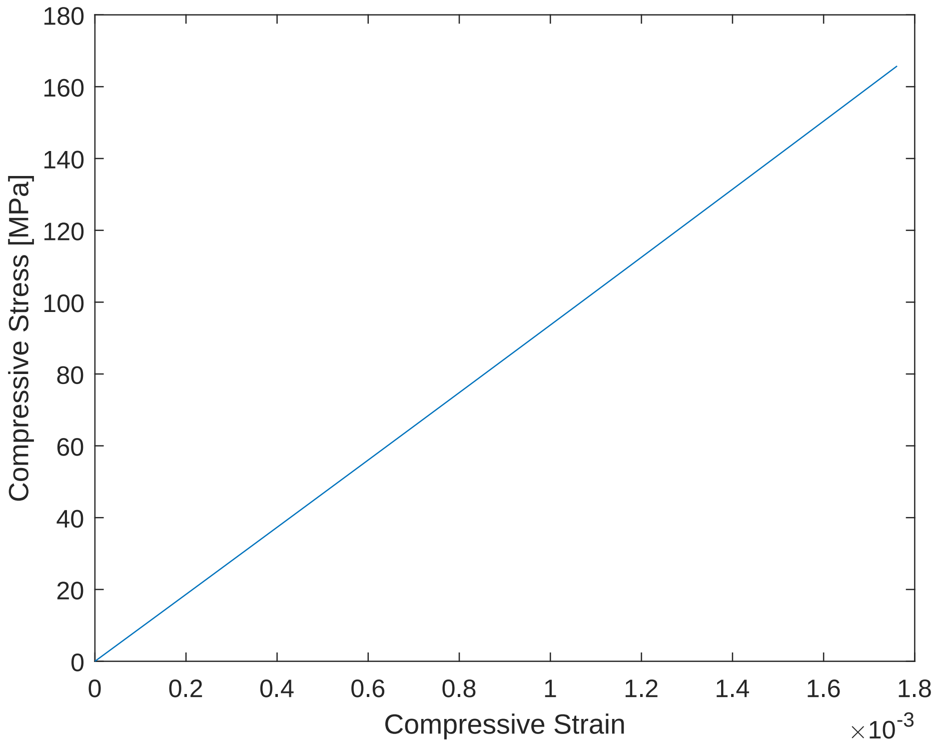

Figure 9.6.: Stress/strain graph 10° offset, loading 5,391.0 N.

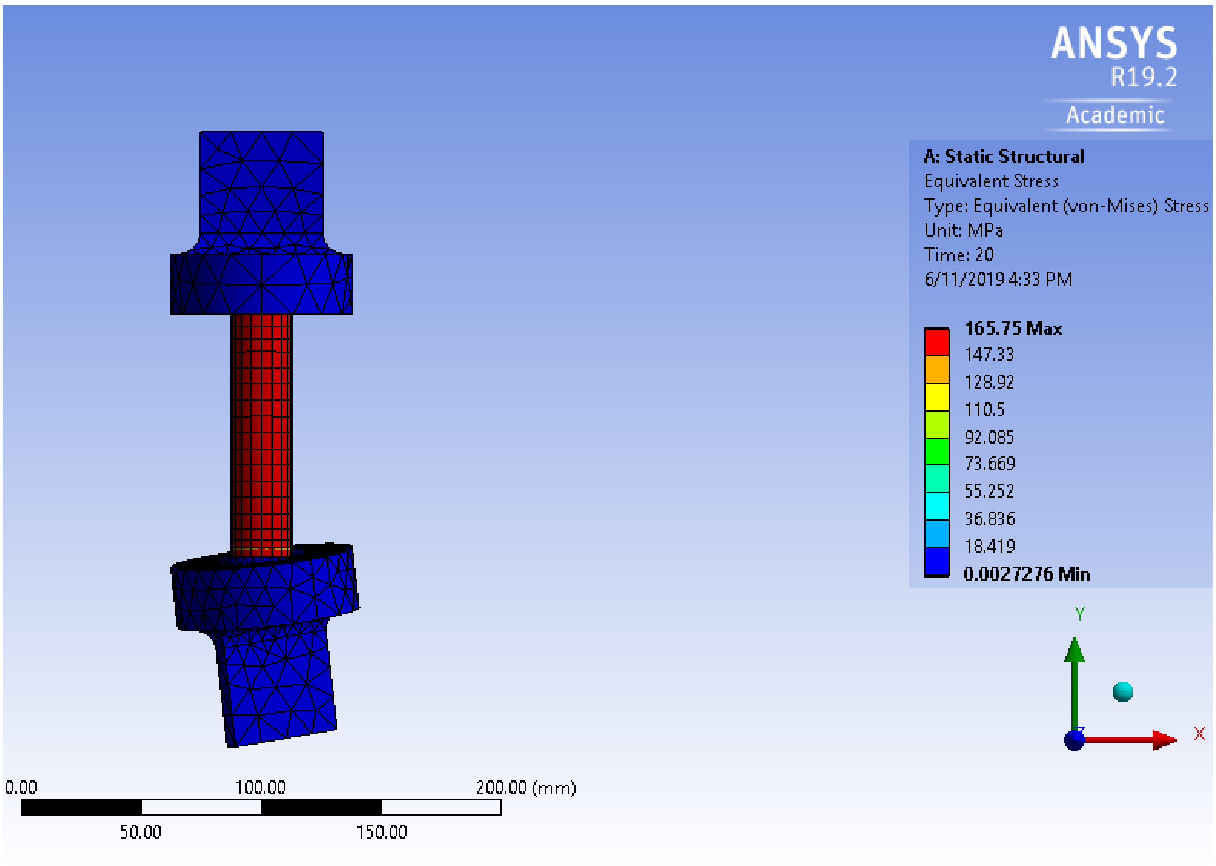

Figure 9.7.: Equivalent stress distribution 10° offset, loading 5,391.0 N.

Table 9.3.: Numerical determined stress and strain of the aluminum cylinder 10° offset, 5,391.0 N.

F [N]	σ_v [MPa]	ϵ_v [$\frac{mm}{mm}$]
356.80	10.97	1.1775×10^{-4}
713.60	21.94	2.3545×10^{-4}
1071.04	32.93	3.5309×10^{-4}
1428.82	43.93	4.7069×10^{-4}
1786.92	54.94	5.8823×10^{-4}
2145.34	65.96	7.0573×10^{-4}
2504.42	77.00	8.2318×10^{-4}
2863.50	88.04	9.4059×10^{-4}
3223.22	99.10	1.0586×10^{-3}
3583.30	110.17	1.1753×10^{-3}
3943.97	121.26	1.2925×10^{-3}
4304.99	132.36	1.4098×10^{-3}
4666.35	143.47	1.5270×10^{-3}
5028.35	154.60	1.6442×10^{-3}
5391.0	165.75	1.7613×10^{-3}

9.4. Result of Compression Test Using an Offset of 15°

In Figure 9.9, the equivalent stress distribution of the test fixture and the specimen with an offset of 15° is shown. The stress/strain graph is shown in Figure 9.8. The calculated stress and strain values can be found in table 9.4.
A force of 2,032.0 N, which caused a stress of $\sigma_{v,max}$ = 62.14 MPa and a strain of $\epsilon_{v,max} = 6.6580 \times 10^{-4} \frac{\text{mm}}{\text{mm}}$, has been applied to the specimen.
The simulated force for this test was approx. 62% lower than the force used in the previous test (chapter 9.3), which caused a lower stress level and a lower strain.
The line rises linearly and has a constant slope gradient. A plastic deformation did not occur.

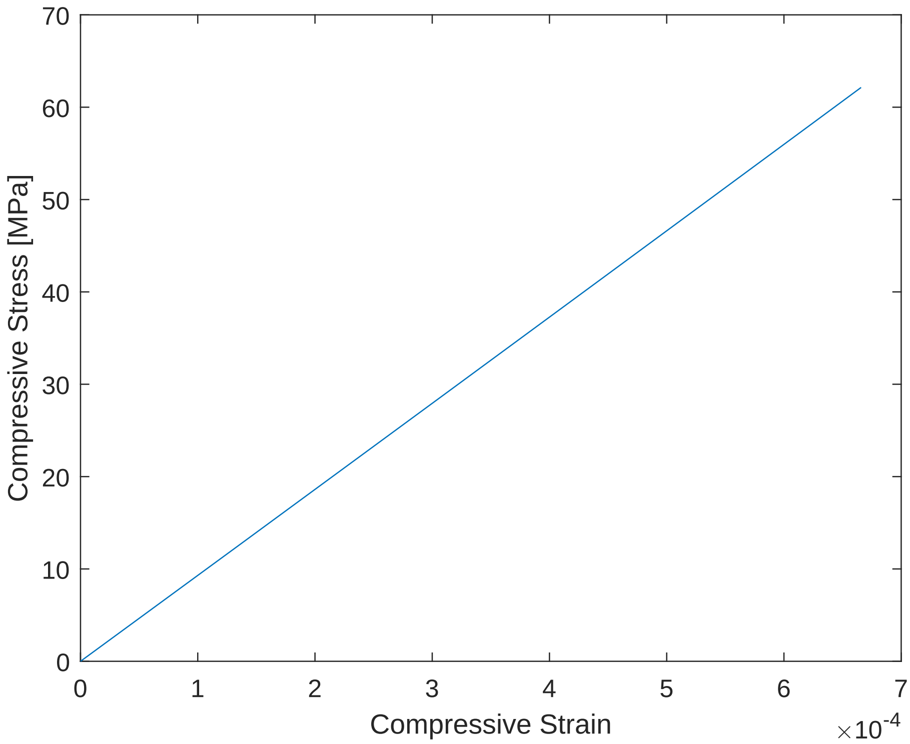

Figure 9.8.: Stress/strain graph 15° offset, loading 2,032.0 N.

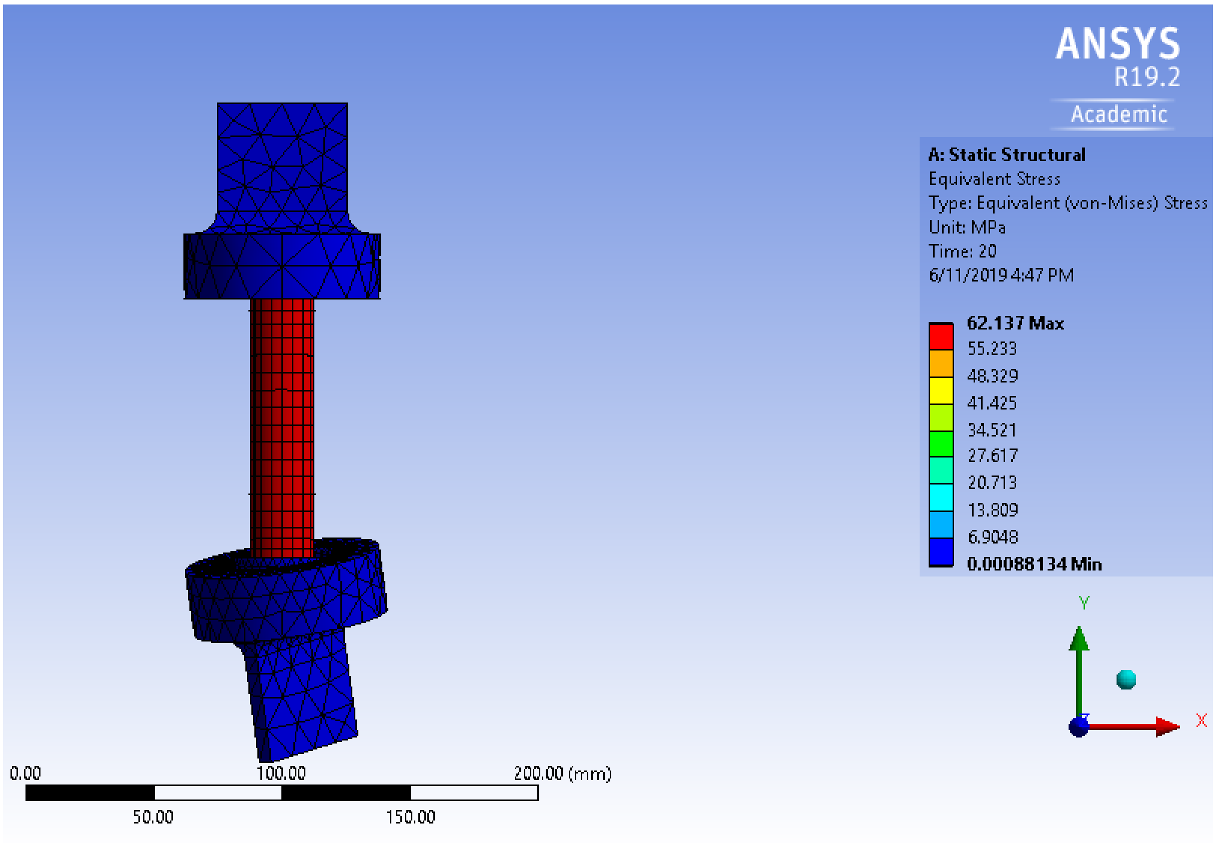

Figure 9.9.: Equivalent stress distribution 15° offset, loading 2,032.0 N.

Table 9.4.: Numerical determined stress and strain of the aluminum cylinder 15° offset, 2,032.0 N.

F [N]	σ_v [MPa]	ϵ_v [$\frac{mm}{mm}$]
135.10	4.13	4.4437×10^{-5}
270.12	8.26	8.8867×10^{-5}
405.50	12.40	1.3329×10^{-4}
540.73	16.54	1.7770×10^{-4}
675.95	20.67	2.2211×10^{-4}
811.33	24.81	2.6651×10^{-4}
946.72	28.95	3.1091×10^{-4}
1082.43	33.10	3.5529×10^{-4}
1217.82	37.24	3.9967×10^{-4}
1353.21	41.38	4.4405×10^{-4}
1488.92	45.53	4.8841×10^{-4}
1624.63	49.68	5.3277×10^{-4}
1760.35	53.83	5.7712×10^{-4}
1896.06	57.98	6.2147×10^{-4}
2032.0	62.14	6.6580×10^{-4}

10. Results of the Numerical Analysis of the Composite Cylinders

In this chapter, the results of the numerical results of the compression tests of the composite cylinders are discussed.
In Figure 10.1, the different stress/strain graphs are combined into one graph to provide a first overview. The load applied in the numerical analysis is adjusted to the applied loads in the experimental tests (see chapter 7). Consequently, a comparison between the different graphs in Figure 9.1 is only possible up to a specific load.
In this section, the similarities of the tests are described. The composite cylinders experienced only reversible deformations. A failure of the composite cylinders did not occur.
All lines rise linearly. The slope of the 0° line is steeper than the slope of the other lines. All other lines have the same slope gradient and only differ in the experienced stress and strain.
The strain, force and stress values deviate from the experimental data. However, a slight deviation is acceptable. Reasons for the slight deviations of the values might be a too coarse mesh. Refining the mesh leads to more precise results. However, refining the mesh leads to an increased solving time. The correct balance between desired precision of the results and solving time has to be found. Moreover, the material properties were only assumed and consequently differ slightly from the exact properties.

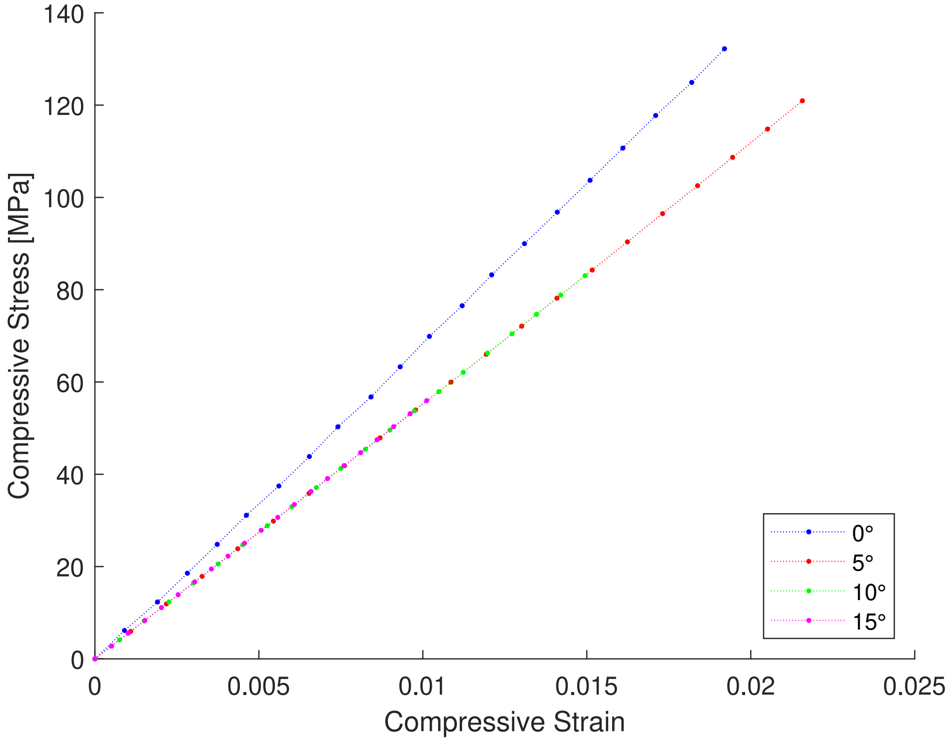

Figure 10.1.: Comparison of the different stress/strain graphs, different loadings.

10.1. Result of the Compression Test Using an Offset of 0°

In Figure 10.2, the minimum stress distribution of the test fixture with the specimen is shown. The stress/strain graph is shown in Figure 10.3. The calculated stress and strain values can be found in table 10.1.
A force of 5,674.86 N, which caused a stress of $\sigma_{III,max} = 132.22$ MPa and a strain of $\epsilon_{III,max} = 1.920 \times 10^{-2}\,\frac{\text{mm}}{\text{mm}}$, has been applied to the specimen.
The line rises linearly and has a constant slope gradient. Consequently, the cylinder was only elastically deformed and the first fibre/resin debonding did not occur. However, in Figure 10.2 the highest stress concentration is in the upper and lower areas of the cylinder. It is expected that the damage process of the cylinder would have taken place in these areas if the load applied was increased.
The reasons for the deviation of the experimental determined stress/strain graph (see chapter 7.1) are because the material properties of the composite material are approximated and not exactly determined. However, the stress and strain shown in Figure 10.3 matches the first part of the stress and strain graph shown in Figure 7.4.

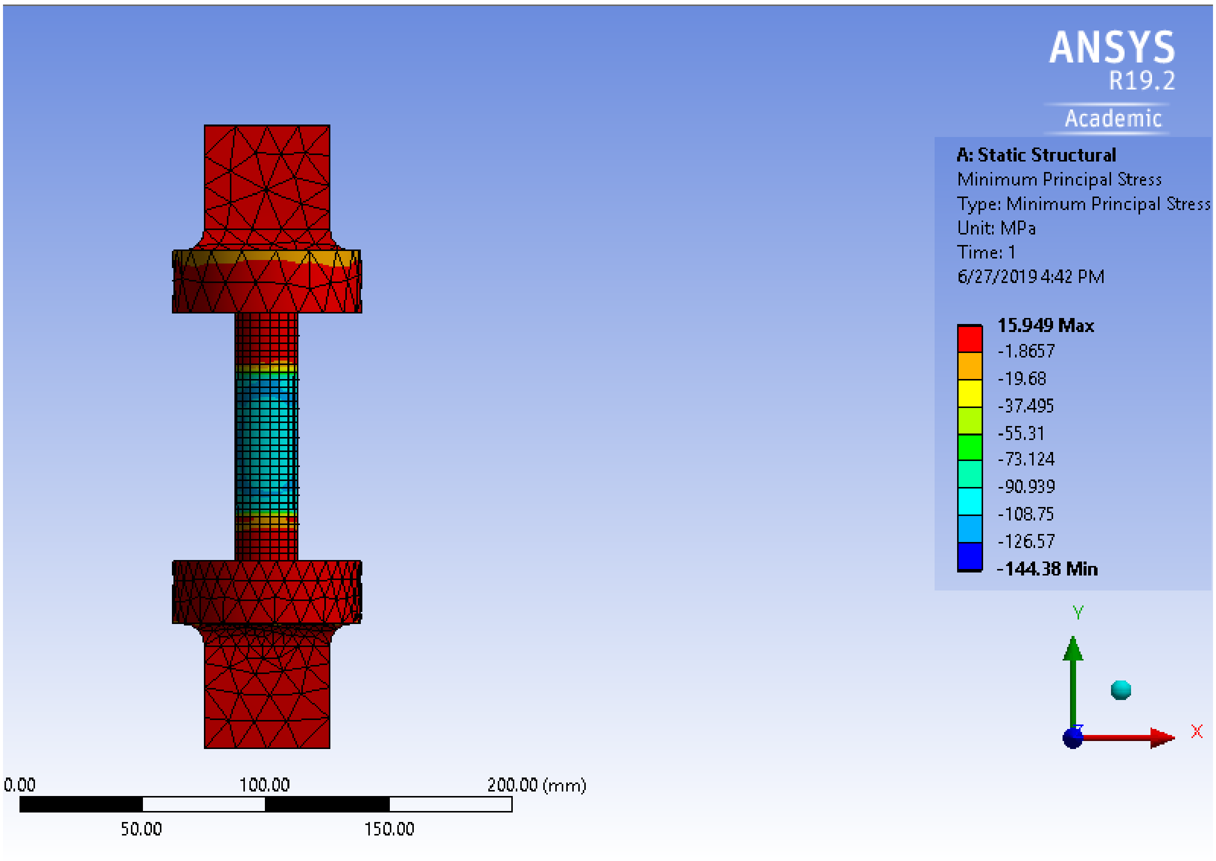

Figure 10.2.: Minimum principal stress distribution 0° offset.

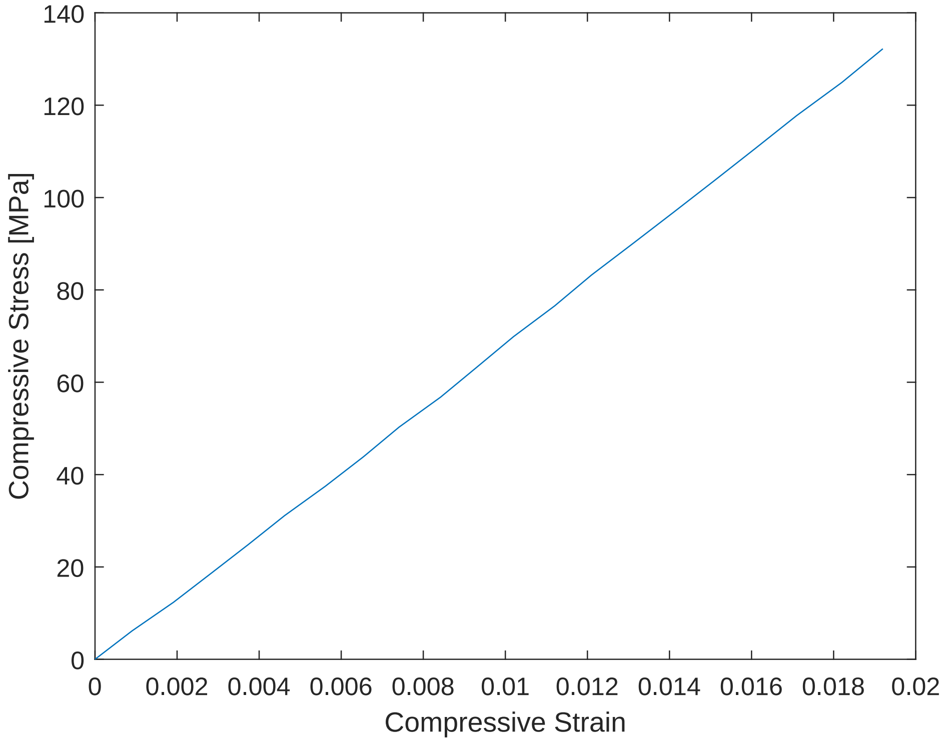

Figure 10.3.: Stress/strain graph 0° offset, loading 5,674.86 N.

Table 10.1.: Numerical determined stress and strain of the composite cylinder 0° offset.

F [N]	σ_{III} [MPa]	ϵ_{III} [$\frac{mm}{mm}$]
263.91	6.1479	9.020×10^{-4}
529.37	12.3320	$1.91\ 0 \times 10^{-3}$
796.46	18.5540	2.820×10^{-3}
1065.17	24.8140	3.730×10^{-3}
1335.70	31.1160	4.620×10^{-3}
1607.98	37.4590	5.610×10^{-3}
1882.20	43.8470	6.540×10^{-3}
2158.40	50.2810	7.410×10^{-3}
2436.63	56.7630	8.420×10^{-3}
2717.11	63.2970	9.310×10^{-3}
2999.77	69.8820	1.020×10^{-2}
3284.90	76.5240	1.120×10^{-2}
3572.46	83.2230	1.210×10^{-2}
3862.64	89.9830	1.310×10^{-2}
4155.90	96.8140	1.410×10^{-2}
4451.89	103.7100	1.510×10^{-2}
4751.51	110.6900	1.610×10^{-2}
5054.60	117.7500	1.710×10^{-2}
5323.60	124.9200	1.820×10^{-2}
5674.86	132.2200	1.920×10^{-2}

10.2. Result of the Compression Test Using an Offset of 5°

In Figure 10.4, the minimum stress distribution of the test fixture with the specimen is shown. The stress/strain graph is shown in Figure 10.5. The calculated stress and strain values can be found in table 10.2.
A force of 4,786.80 N, which caused a stress of $\sigma_{III,max} = 120.95$ MPa and a strain of $\epsilon_{III,max} = 2.157500 \times 10^{-2}\,\frac{\text{mm}}{\text{mm}}$, has been applied to the specimen.
The line rises linearly and has a constant slope gradient. Consequently, the cylinder was only elastically deformed and the first fibre/resin debonding did not occur. However, in Figure 10.4 the highest stress concentration is in the upper and lower areas of the cylinder. It is expected that the damage process of the cylinder would have taken place in these areas if the load applied was increased.
The stress and strain shown in Figure 10.5 matches the first part of the stress and strain graph shown in Figure 7.6.

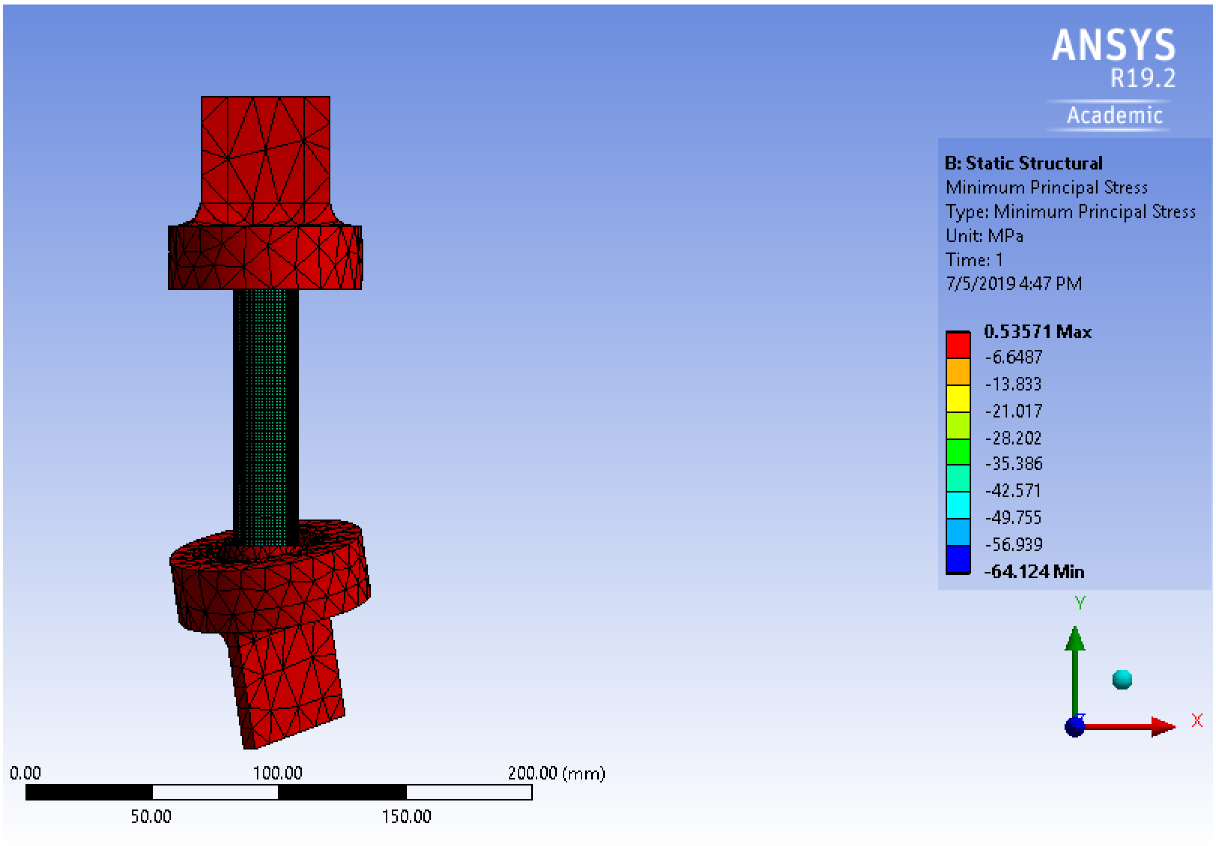

Figure 10.4.: Minimum principal stress distribution 5° offset.

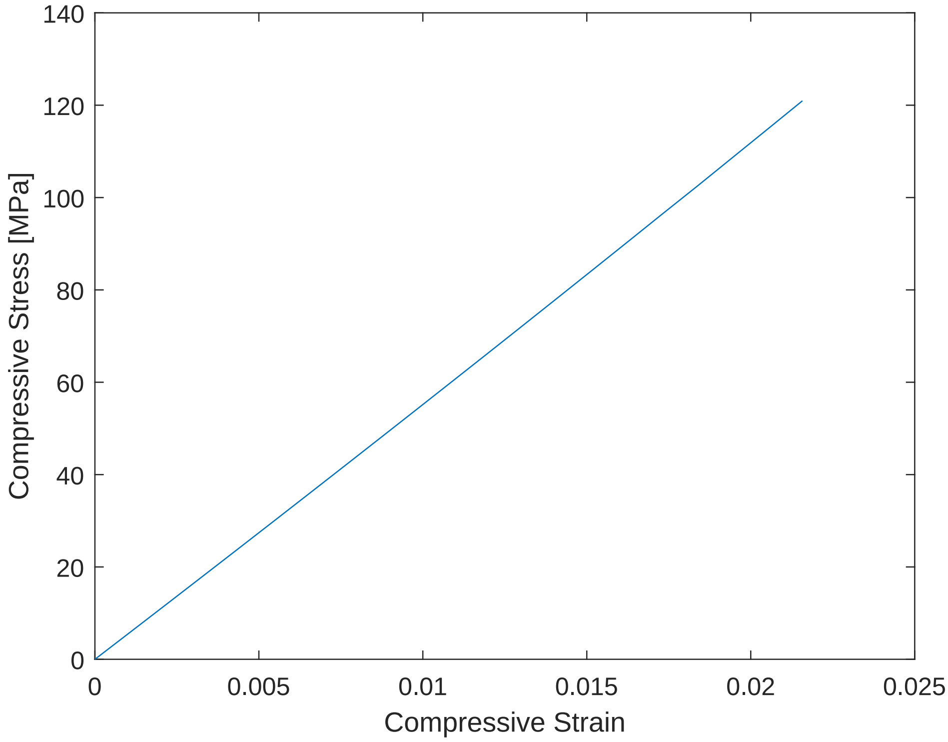

Figure 10.5.: Stress/strain graph 5° offset, loading 4,786.8 N.

Table 10.2.: Numerical determined stress and strain of the composite cylinder 5° offset.

F [N]	σ_{III} [MPa]	ϵ_{III} [$\frac{mm}{mm}$]
235.47	5.9498	1.09060×10^{-3}
471.36	11.91	2.18010×10^{-3}
707.63	17.88	3.26860×10^{-3}
944.30	23.86	4.35610×10^{-3}
1181.40	29.851	5.44250×10^{-3}
1418.94	35.853	6.52780×10^{-3}
1656.88	41.865	7.61190×10^{-3}
1895.30	47.889	8.69490×10^{-3}
2134.10	53.923	9.77670×10^{-3}
2373.33	59.968	1.08570×10^{-2}
2613.05	66.025	1.19370×10^{-2}
2853.20	72.093	1.30150×10^{-2}
3093.87	78.174	1.40910×10^{-2}
334.97	84.266	1.51660×10^{-2}
3576.43	90.367	1.6240×10^{-2}
3818.64	96.487	1.73120×10^{-2}
4057.80	102.53	1.83790×10^{-2}
4301.19	108.68	1.94470×10^{-2}
453.80	114.81	2.05120×10^{-2}
4786.80	120.95	2.15750×10^{-2}

10.3. Result of the Compression Test Using an Offset of 10°

In Figure 10.6, the minimum stress distribution of the test fixture with the specimen is shown. The stress/strain graph is shown in Figure 10.7. The calculated stress and strain values can be found in table 10.3.
A force of 3,302.90 N, which caused a stress of $\sigma_{III,max} = 83.052$ MPa and a strain of $\epsilon_{III,max} = 1.49501 \times 10^{-2} \frac{\text{mm}}{\text{mm}}$, has been applied to the specimen.
The line rises linearly and has a constant slope gradient. Consequently, the cylinder was only elastically deformed and the first fibre/resin debonding did not occur. However, in Figure 10.6 the highest stress concentration is in the upper and lower areas of the cylinder. It is expected that the damage process of the cylinder would have taken place in these areas if the load applied was increased.
The stress and strain shown in Figure 10.7 matches the first part of the stress and strain graph shown in Figure 7.9.

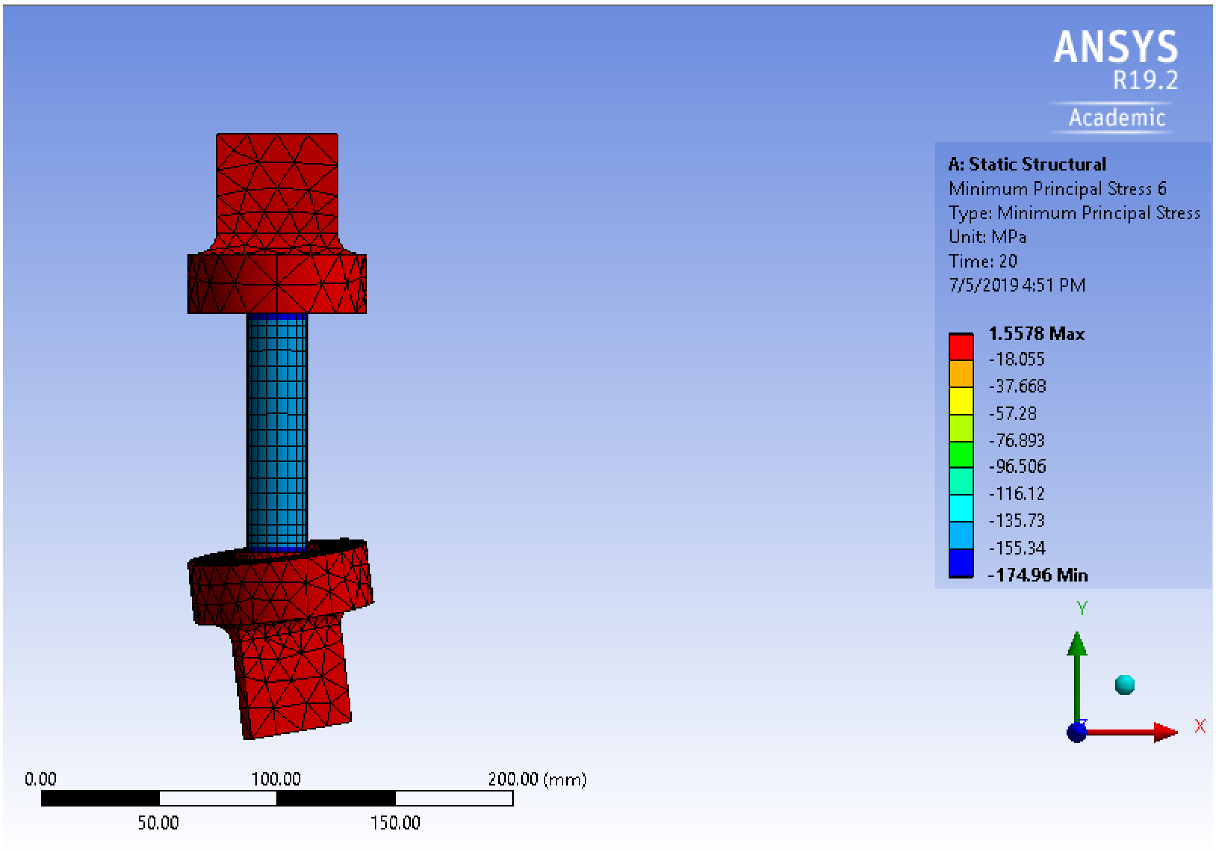

Figure 10.6.: Minimum principal stress distribution 10° offset.

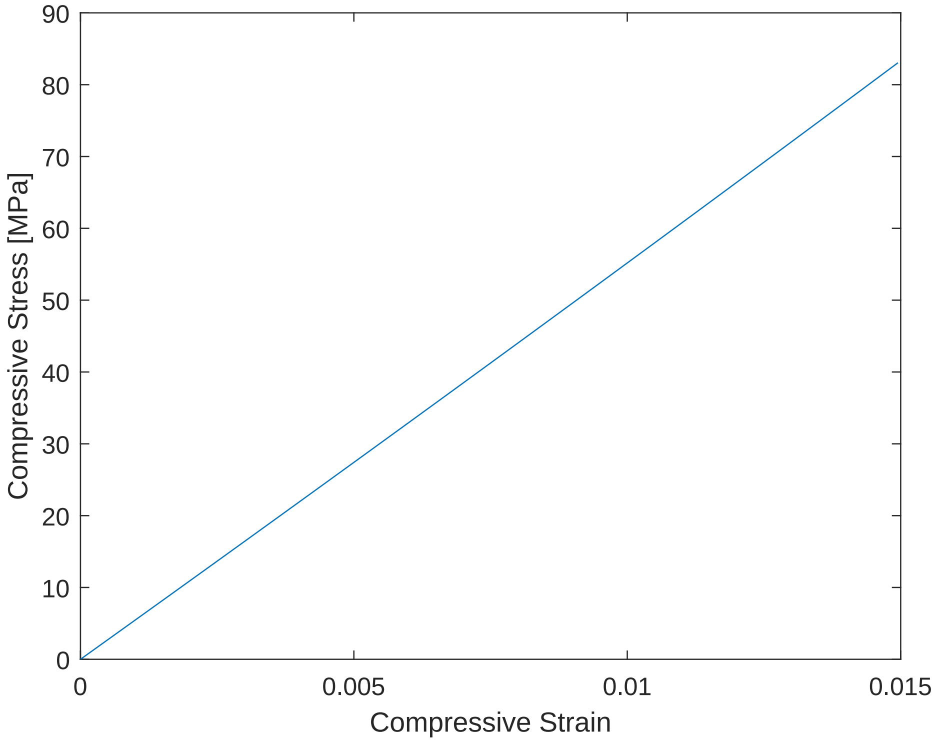

Figure 10.7.: Stress/strain graph 10° offset, loading 3,302.90 N.

Table 10.3.: Numerical determined stress and strain of the composite cylinder 10° offset.

F [N]	σ_{III} [MPa]	ϵ_{III} [$\frac{mm}{mm}$]
163.23	4.1045	7.52490×10^{-4}
326.66	8.2138	1.50450×10^{-3}
490.27	12.328	2.25610×10^{-3}
654.10	16.447	3.00710×10^{-3}
818.10	20.571	3.75760×10^{-3}
982.30	24.70	4.50770×10^{-3}
1146.70	28.834	5.25720×10^{-3}
1311.27	32.972	6.00620×10^{-3}
1476.07	37.116	6.75470×10^{-3}
1641.11	41.266	7.50260×10^{-3}
1806.31	45.42	8.25011×10^{-3}
1971.71	49.579	8.99680×10^{-3}
2137.35	53.744	9.74310×10^{-3}
2303.19	57.914	1.04890×10^{-2}
2469.26	62.09	1.12340×10^{-2}
2635.54	66.271	1.19780×10^{-2}
2802.05	70.458	1.27220×10^{-2}
2968.76	74.65	1.34650×10^{-2}
3135.71	78.848	1.42080×10^{-2}
3302.90	83.052	1.49501×10^{-2}

10.4. Result of the Compression Test Using an Offset of 15 °

In Figure 10.8, the minimum stress distribution of the test fixture with the specimen is shown. The stress/strain graph is shown in Figure 10.9. The calculated stress and strain values can be found in table 10.4.
A force of 2,231.7 N, which caused a stress of $\sigma_{III,max} = 55.95$ MPa and a strain of $\epsilon_{III,max} = 1.01170 \times 10^{-2}\,\frac{\mathrm{mm}}{\mathrm{mm}}$, has been applied to the specimen.
The line rises linearly and has a constant slope gradient. Consequently, the cylinder was only elastically deformed and the first fibre/resin debonding did not occur. However, in Figure 10.8 the highest stress concentration is in the upper and lower areas of the cylinder. It is expected that the damage process of the cylinder would have taken place in these areas if the load applied was increased.
The stress and strain shown in Figure 10.9 matches with the first part of the stress and strain graph shown in Figure 7.12.

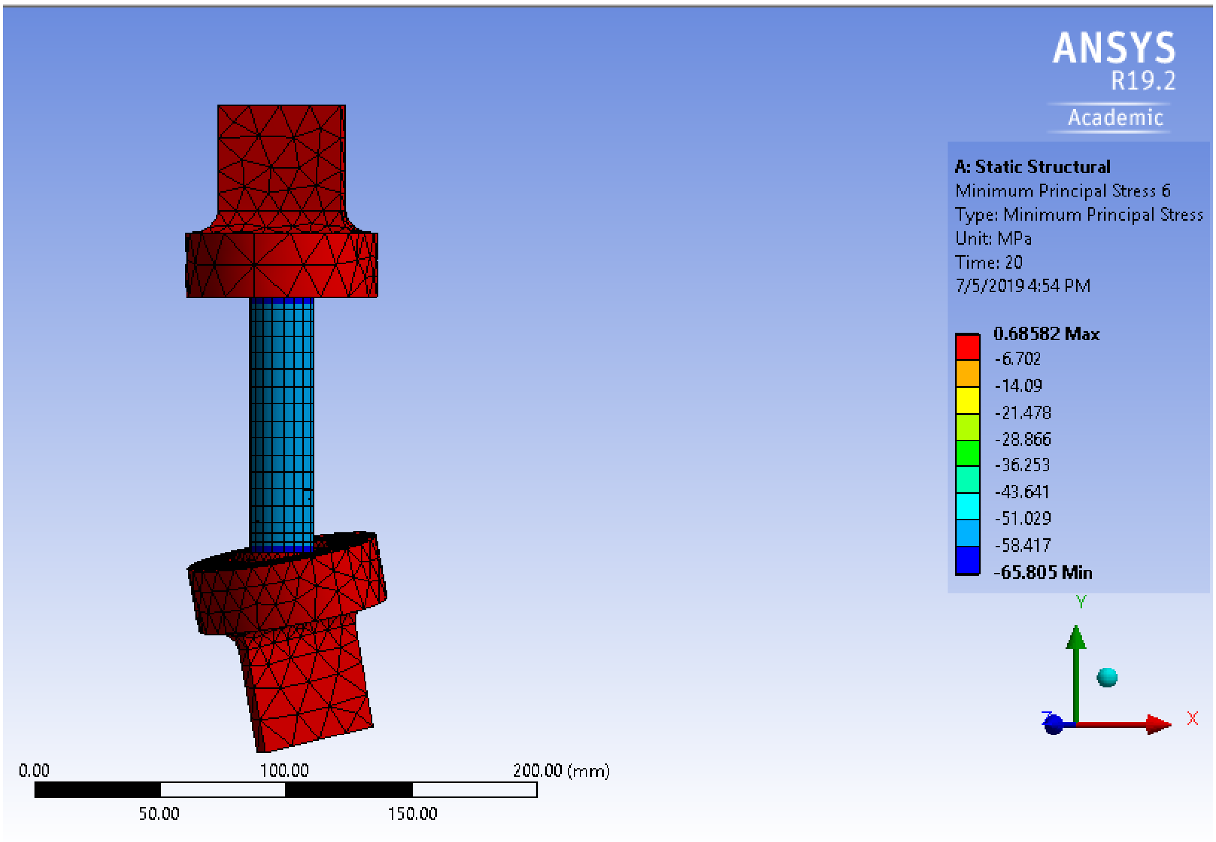

Figure 10.8.: Minimum principal stress distribution 15° offset.

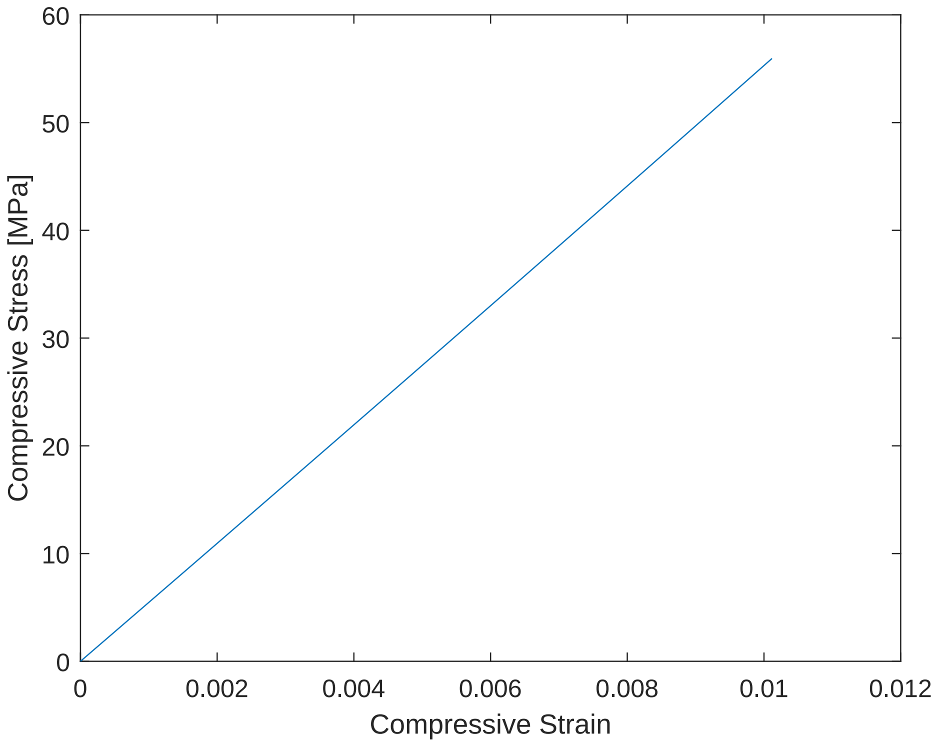

Figure 10.9.: Stress/strain graph 15° offset, loading 2,231.7 N.

Table 10.4.: Numerical determined stress and strain of the composite cylinder 15° offset.

F [N]	σ_{III} [MPa]	ϵ_{III} $[\frac{mm}{mm}]$
110.70	2.7753	5.08020×10^{-4}
221.49	5.5529	1.01580×10^{-3}
332.37	8.3327	1.52340×10^{-3}
443.35	11.115	2.03080×10^{-3}
554.39	13.899	2.53790×10^{-3}
665.56	16.686	3.04480×10^{-3}
776.81	19.475	3.55160×10^{-3}
888.13	22.266	4.05810×10^{-3}
999.58	25.06	4.56430×10^{-3}
1111.10	27.856	5.07030×10^{-3}
1222.75	30.655	5.57610×10^{-3}
1334.43	33.455	6.08160×10^{-3}
1446.28	36.259	6.58690×10^{-3}
1558.16	39.064	7.09210×10^{-3}
1670.17	41.872	7.59680×10^{-3}
1782.29	44.683	8.10140×10^{-3}
2006.81	47.496	8.60570×10^{-3}
2119.2	50.312	9.10970×10^{-3}
2119.22	53.13	9.61350×10^{-3}
2231.7	55.95	1.01170×10^{-2}

11. Conclusion

In this thesis, composite cylinders were subjected to a compression loading with loading angles of 0°, 5°, 10° and, 15°. The cylinders were manufactured using the filament winding technique, and a winding angle of 45° was used.
The bottom part of the first test fixture used for the tests had to be clamped with an offset into the hydraulic grip of the compression testing machine to cause the offset loading. However, because of this design, the bottom part of the test fixture was prone to slipping. This slipping was more severe with increasing offset and increasing load. Thus, the data obtained with this test fixture can be compared up to the point when the slipping started. Moreover, the cylinders tested with an offset of more than 5° did not experience any visible damage, because the bottom part started to slip.

According to the test results of the composite cylinders tested with the first fixture, the compression strength decreases with increasing offset. Consequently, the compression strength of the composite cylinder tested with an offset of 0° was the highest and the strength of the cylinder tested with an offset of 15° was the weakest. Stresses of $\sigma = 162.14$ MPa and $\sigma = 63.66$ MPa were required to cause the failures of the composite cylinders tested with an offset of 0° and 15°. The aluminum cylinders experienced also a decrease of the compression strength with increasing offset.
Because of the previously described issue of the bottom part of the first test fixture, a second test fixture was designed such, that the bottom part did not have to be clamped with an offset into the grip. Consequently, three different bottom parts were designed and printed. One different part was used for each loading angle greater than 0°. For the 0° offset, the first test fixture was used. However, the new design of the second test fixture had an influence of the failure type of the composite cylinders. Due to these bottom parts, the cylinders started to buckle.
According to the test results of the composite cylinders tested with the second test fixture, the compression strength decreases with increasing offset. However, some material imperfections caused locally a too-high stress concentration in the cylinder, which caused an early failure. Consequently, the cylinder tested with an offset of 5° had a higher strength than the cylinder tested with an offset of 0°. The compression strength of the composite cylinder tested with an offset of 5° is the highest and the strength of the cylinder tested with an offset of 10° is the weakest. Stresses of $\sigma = 103.18$ MPa and $\sigma = 82.58$ MPa were required to cause the failures of the cylinder tested with an offset of 5° and 10°.
The three-layered cylinder, except for the 0° and 15°, also had a higher compression strength than the two-layered cylinder, because of the larger cross section.

Numerical analyses of the compression tests of the aluminum alloy cylinders and the two-layered composite cylinders were also conducted. For these analyses, the first test fixture was used. However, the computed results differ from the results obtained by the experimental tests. One of the reasons for the deviation was that the material properties were only assumed and not exactly determined. Consequently, the assumed Young's modulus is too low in comparison to the actual Young's modulus.

11.1. Outlook

The use of composite materials for the design of structures in high-performance applications (e.g., aerospace, automotive, and motorsport), which require a high level of compressive performance, will become more important in the future. Especially, the compressive modulus and strength of a composite material are critical parameters for many structural uses. Therefore, it is important to confidently predict their compressive response. According to the results of this thesis, the compression strength of the composite material decreases with increasing loading angles. Since composite materials are used in structures (e.g., aircraft) that do not experience only non-offset loadings, and because of the increasing application of these materials, predicting the compression strength under different loading angles becomes more important in the future.

More tests must be conducted with the cylinders to obtain comparable results and the slipping of the test fixture in the grip must be solved.

Bibliography

[1] Gurit, "Guide to composites." https://www.google.de/url?sa=t&rct=j&q=&esrc=s&source=web&cd=1&ved=2ahUKEwj21c-Us9HiAhUYsZ4KHQq6C-IQFjAAegQIAxAC&url=https%3A%2F%2Fwww.gurit.com%2F-%2Fmedia%2FGurit%2FDatasheets%2Fguide-to-composites.pdf&usg=AOvVaw0I4iUcAlXzhgQzgI24vcVw. Accessed on 04-06-2019.

[2] E. Gaertner and M. DeBortoli, "Wireless technology applied in 3-axis filament winding machine control system using mit app inventor," *International Ansys conference*, 2006.

[3] University of Cambridge, "Yield criteria for metals." www.doitpoms.ac.uk/tlplib/metal-forming-1/yield_criteria.php. Accessed on 03-04-2019.

[4] Netzsch, "Spannungs-/dehnungsverhalten." https://www.netzsch-thermal-analysis.com/de/industrien-branchen/glossary/spannungs-dehnungsverhalten/. Accessed on 30-05-2019.

[5] Sharcnet.ca, "Deformation." https://www.sharcnet.ca/Software/Ansys/17.0/en-us/help/wb_sim/ds_Deformation.html. Accessed on 03-04-2019.

[6] Sharcnet.ca, "Max., mid., and min. principal." www.sharcnet.ca/Software/Ansys/17.0/en-us/help/wb_sim/ds_Princip_Stress.html. Accessed on 03-04-2019.

[7] Q. Ma, R. Rejab, J. Kaige, I. M. Sahat, and N. Harith, "Filament winding technique, experiment and simulation analysis on tubular structure," *IOP Conference Series Materials Science and Engineering*, 2018.

[8] P. D. Soden, R. Kitching, P. C. Tse, Y. Tsavalas, and M. J. Hinton, "Influence of winding angle on the strength and deformation of filament-wound composite tubes subjected to uniaxial and biaxial loads," *Composites Science and Technology*, vol. 46, pp. 363–378, 1993.

[9] E. Sancaktar and D. A. Schauber, "Failure behavior of filament-wound carbon fiber/epoxy composite tubes under axial compression," vol. 116, 01 2003.

[10] I. M. Daniel, "Yield and failure criteria for composite materials under static and dynamic loading," *Strain - An international Journal for Experimental Mechanics*, vol. 43, pp. 4–12, 2007.

[11] M. Jawaid, M. Thariq, and N. Saba, "Durability and life prediction in biocomposites, fibre-reinforced composites and hybrid composites," *Composites Science and Engineering*, 2019.

[12] P. Camanho, "Failure criteria for fibre-reinforced polymer composites," 2002.

[13] S. Bhavya, P. R. Kumar, and S. A. Kalam, "Failure analysis of a composite cylinder," *Journal of Mechanical and Civil Engineering*, vol. 3, pp. 01–07, 2012.

[14] J. Sengupta, "Recent advances in the failure theories," *Researchgate*, 2016.

[15] E. L. Gaertner and M. Giovanni, "Some aspects for the simulation of a non-linear problem with plasticity and contact," *IOP Conference Series Materials Science and Engineering*, 2019.

[16] Sharcnet.ca, "Plasticity models." https://www.sharcnet.ca/Software/Fluent14/help/ans_mat/amp8sq21dldm.html#miso. Accessed on 05-30-2019.

[17] Sharcnet.ca, "Stress and strain." https://www.sharcnet.ca/Software/Ansys/17.0/en-us/help/wb_sim/ds_Stress_Strain.html. Accessed on 03-04-2019.

[18] Sharcnet.ca, "Equivalent (von mises)." https://www.sharcnet.ca/Software/Ansys/17.0/en-us/help/wb_sim/ds_Equiv_Stress.html. Accessed on 03-04-2019.

[19] L. M. Surhone, M. T. Timpledon, and S. F. Marseken, *Mechanics of Composite Materials*. VDM Publishing, 2010.

A. Appendix

Table A.1.: Material properties of the aluminum alloy AMS-WW-T-700/6C used for the cylinders.

Young's Modulus [MPa]	Poisson's ratio	Bulk Modulus [MPa]	Shear Modulus [MPa]
7100	0.33	69608	26692

Ultimate strength [MPa]	Yield strength [MPa]
310	276

Table A.2.: Multilinear isotropic hardening values of the aluminum alloy.

Stress [MPa]	Plastic Strain $\left[\frac{mm}{mm}\right]$	Temperature [C]
1.0×10^{-10}	0	20
270	5.0×10^{-3}	20
300	2.0×10^{-2}	20
305	3.0×10^{-2}	20
322	6.50×10^{-2}	20

Table A.3.: Material properties of the stainless steel used for the test fixture.

Young's Modulus [MPa]	Poisson's ratio	Bulk Modulus [MPa]	Shear Modulus [MPa]
1.930×10^{5}	0.31	201.6930×10^{5}	73664

Tensile Yield / Ultimate Strength [MPa]	Compressive Yield Strength [MPa]
207 / 586	207

Table A.4.: Material properties of the composite material used for the cylinder: T700SC-12K-50C.

Compressive strength [MPa]	Tensile strength / Tensile modulus [MPa]	Tensile strain [%]
1,470.00	2,550.0 / 135,000.0	1.7

B. Appendix

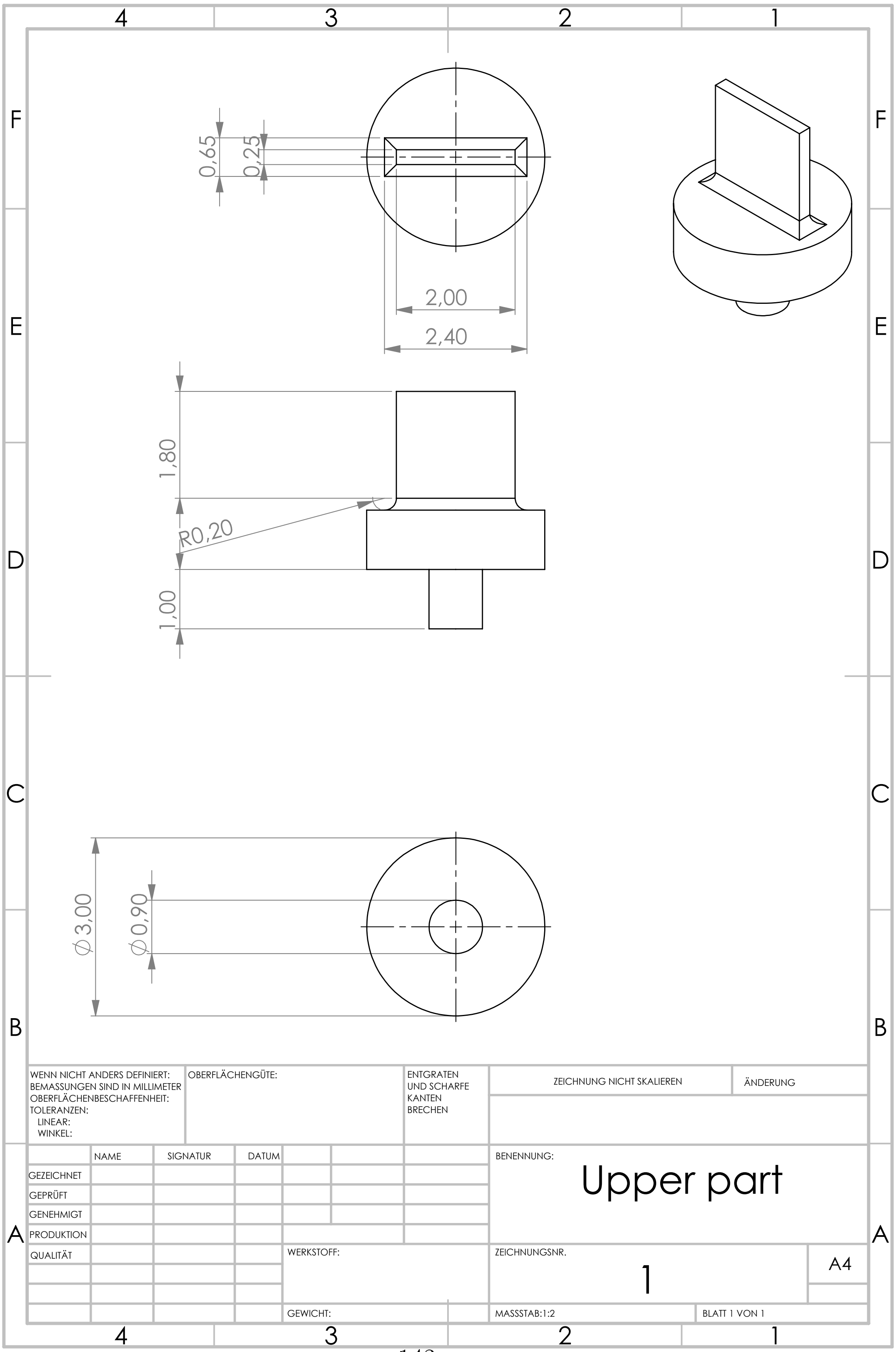

Figure B.1.: Composite compression test fixture—Upper part.

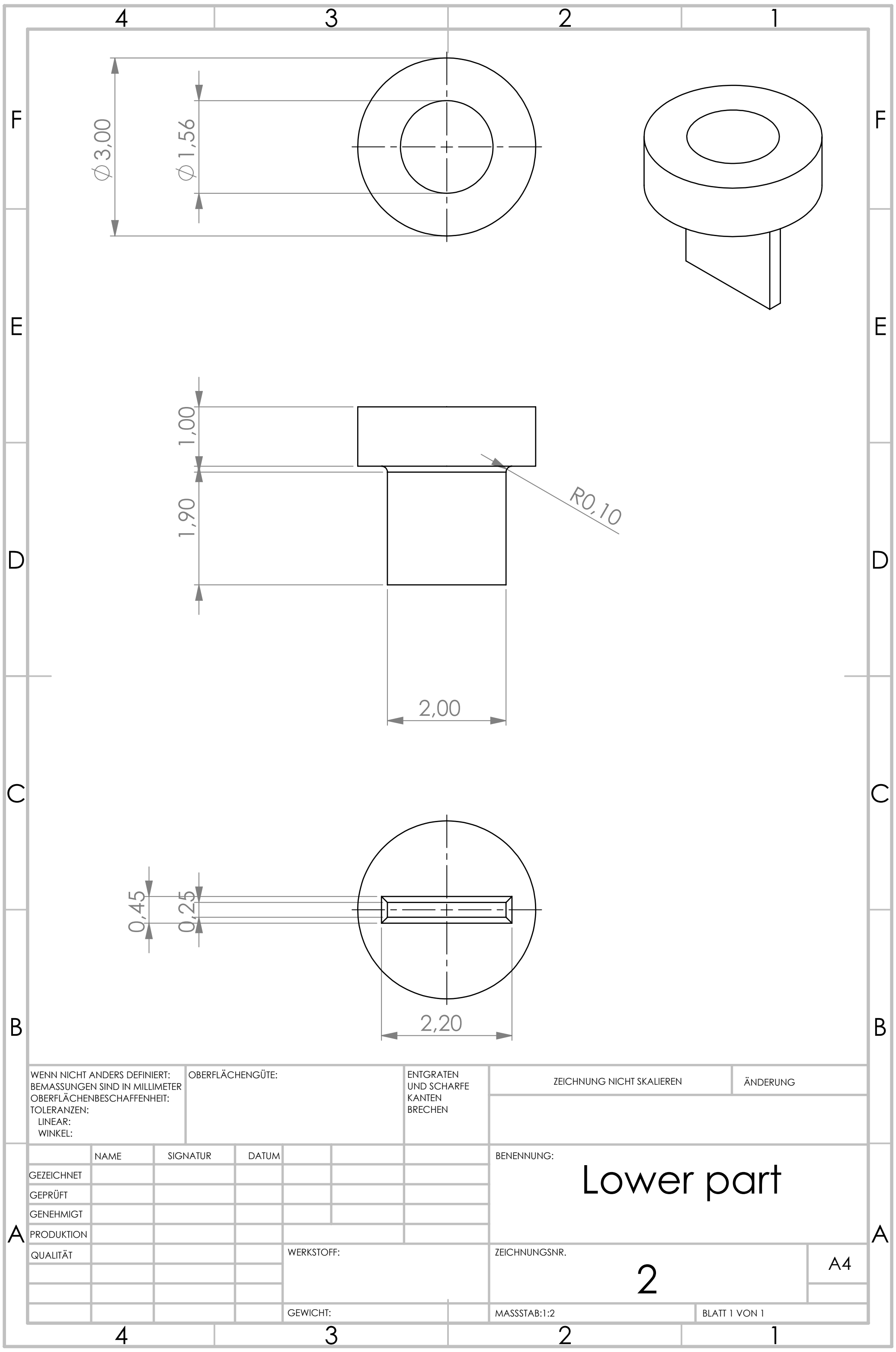

Figure B.2.: Composite compression test fixture—Lower part.

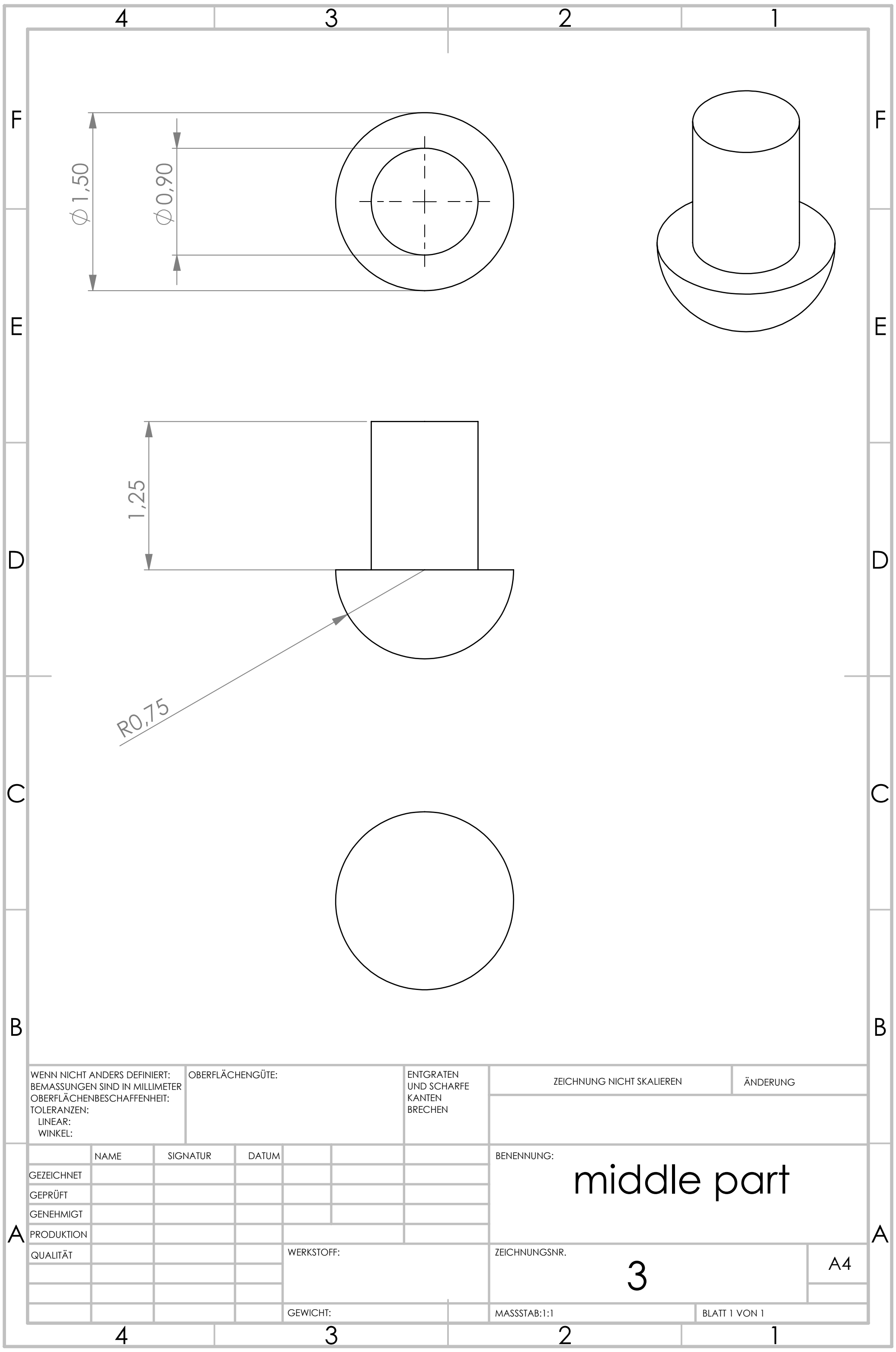

Figure B.3.: Composite compression test fixture—Middle part.

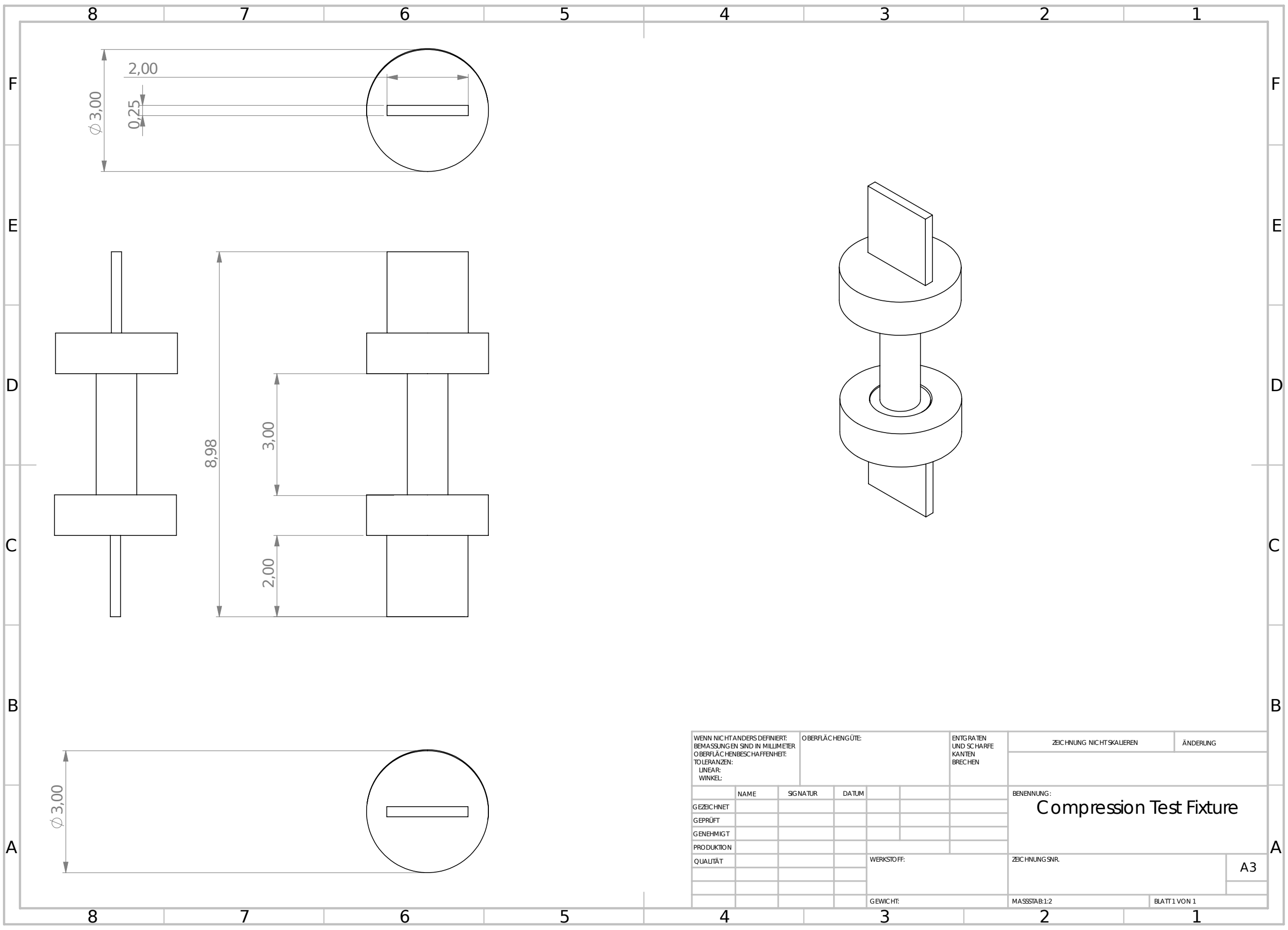

Figure B.4.: Composite compression test fixture—Complete.

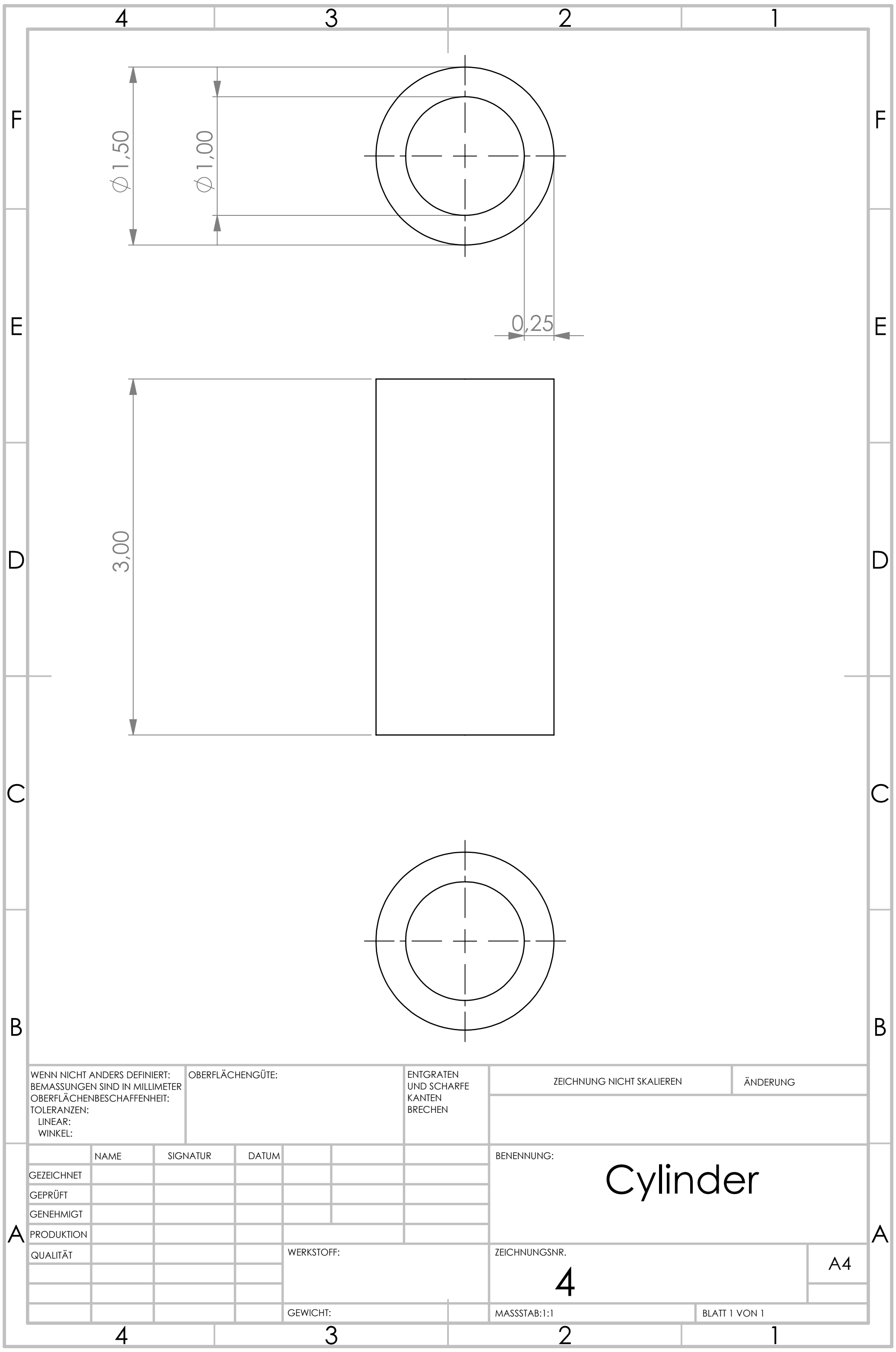

Figure B.5.: Composite compression test fixture—Cylinder.